Experimental Study and Computational Modelling of the Biomechanical Properties of Arteries

Chen Yen Ooi
chenyen.ooi@cantab.net

Department of Engineering
St Catharine's College
University of Cambridge

A dissertation submitted for the degree of

Doctor of Philosophy

August 2014

Preface

This thesis is submitted for the degree of Doctor of Philosophy at the University of Cambridge. The research was conducted from October 2010 to April 2014 in the Department of Engineering, under the supervision of Dr. Michael Sutcliffe. This dissertation is the result of my own work and includes nothing which is the outcome of work done in collaboration except where specifically indicated in the text. This document is original and has not been submitted for any other degree, diploma, or qualifications. This thesis contains approximately 30,400 words with 64 figures and 8 tables, in accordance to the specifications of the Board of Graduate Studies and the Department of Engineering.

Chen Yen Ooi
Cambridge, UK

Acknowledgement

I would like to express my gratitude and appreciation to my supervisor Dr. Michael Sutcliffe for his invaluable support and guidance to perform successful research studies leading to this thesis. In addition to his supervision, Dr. Sutcliffe has run the mechanical tests described in Chapters 4 and 5, and has provided essential support for the development of the MATLAB functions used in these studies. Besides, I would also like to thank my advisor Professor Vikram Deshpande for providing insightful advices and suggestions on the research studies during my PhD annual meetings.

In addition, I would like to acknowledge the collaborators Dr. Janet Maguire, Dr. Anthony Davenport, Dr. Kaisa Mäki-Petäjä, and Professor Ian Wilkinson in the Clinical Pharmacology Unit in the School of Clinical Medicine, University of Cambridge. Dr. Maguire has assisted the mechanical tests in Chapters 4 and 5 as well as run the arterial active function tests described in Chapter 5, in collaboration with Dr. Davenport. Dr. Mäki-Petäjä proposed the study in Chapter 6 and has helped preparing the tissue samples and run the biochemistry assays, with guidance from Professor Wilkinson. The collaboration studies in this thesis would not have succeeded without their help.

Furthermore, I gratefully acknowledge the project grant of the Tunku Abdul Rahman Centenary Fund from St Catharine’s College, and the Engineering for Clinical Practice Grant from the Department of Engineering, which provided essential funds for the equipment, material, and travel costs of my research studies. Lastly, I would also like to thank my family members for their mental and financial support of my PhD study throughout these years.

Contents

Abstract

Biomechanics of artery has been shown to play an important role in the progression of cardiovascular diseases. Thus studies of arterial biomechanics are essential to find the causes and preventions of these diseases. The thesis first introduces work demonstrating the use of the optical flow estimation technique to track the deformation of biological tissue in biomechanical experiments. The study shows that the optical flow technique provides a good estimation of the strains for the constructed deformation images by comparing the results with those of the finite element (FE) models.

The optical flow technique was then used on the analysis of the images obtained from the experiments of human coronary arteries with atherosclerosis. Atherosclerosis is a cardiovascular disease in which the rupture of atherosclerotic plaque leads to stroke or myocardial infarction, where the risk of the rupture has been associated with mechanical factors. An approach was developed combining the tensile ring tests, optical flow analysis, and FE modelling to obtain the heterogeneous mechanical properties of atherosclerotic arteries. This approach provides a sensible estimation of the hyperelastic properties of atherosclerotic plaques by matching the forces and strains of the experiments and FE models using an error minimisation approach.

The study on the biomechanics of atherosclerotic arteries was then extended to the muscle active properties of the diseased vessels. Previous drug response experiments have shown that human atherosclerotic arteries maintained active forces of more than 70% of those in healthy arteries in response to endothelin-1 (ET-1) despite an extensive thinning of the media smooth muscle layer. FE analyses have been performed to model the passive tensile ring tests and active ET-1 response tests, which demonstrate the potential elevated contractile strains of diseased smooth muscle cells in response to ET-1. The results suggest that adaptation mechanisms occur with atherosclerosis to maintain the distensibility of the diseased artery in physiological condition with the presence of cell activation agents.

In addition, a project investigating the role of hyaluronan in systemic inflammation-induced aortic stiffening has been carried out. Systemic inflammation occurs in several diseases such as rheumatoid arthritis which increases aortic stiffness and causes altered distribution and function of arterial hyaluronan. Tensile ring tests were performed on rat aortas that have hyaluronan digested by hyaluronidase and control samples. The results show no significant difference between the elastic modulus of the two groups despite successful digestion of the hyaluronan content in the treated samples in biochemistry assays. A potential mechanism of this contradiction is that the hyaluronan accumulation-induced aortic stiffening is a long term effect in patients and cannot be shown with the methodology of this study.

In order to solve the non-physiological loading limitation of the tensile ring tests in the studies above, an inflation test system has been designed for future experiments. This system inflates an artery ring with a balloon tube with the cross-sectional deformation captured using a camera in an inverted position. The system has been tested with a pig aortic ring with the deformation analysed using the optical flow technique. The estimated elastic modulus of the artery was compared to that obtained from a tensile ring test, which shows a good matching between the two values.

Overall, the thesis demonstrates experimental and computational approaches to study the biomechanical properties of arteries. The results also provide information on the hyperelastic and active properties of atherosclerotic arteries as well as the effects of hyaluronan digestion on the stiffness of rat aortas.

1. Introduction

1.1 Background and Motivation

Biomechanics of artery has been widely studied and shown to be correlated with the causes and prevention of cardiovascular diseases. One of the diseases that causes a significant number of mortality is atherosclerosis (Figure 1.1), where the rupture of atherosclerotic plaque leads to stroke or myocardial infarction. Studies have suggested that the risk of plaque rupture is associated with the composition of the plaque and external mechanical factors. Therefore, knowledge of the local mechanical properties of plaque composition and how atherosclerotic arteries respond to mechanical loads is important to predict the risk of rupture.

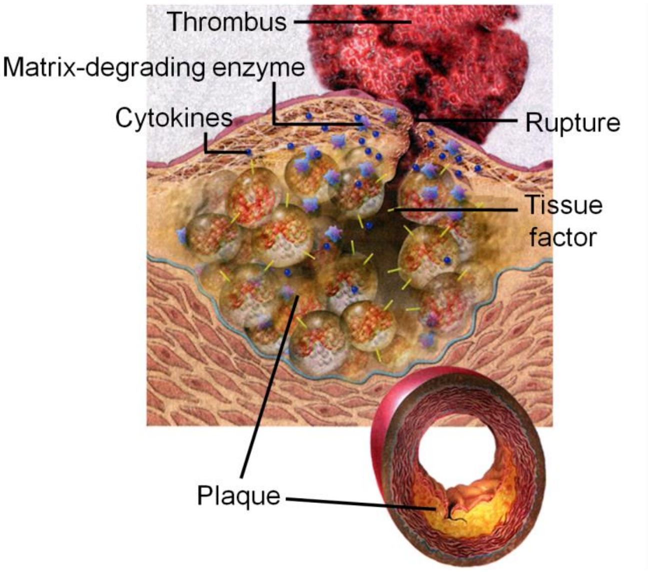

Figure 1.1 A schematic diagram showing the rupture of atherosclerotic plaque. (Libby 2002)

The studies of arterial biomechanics investigated the changes of arterial mechanical properties with cardiovascular diseases for the conditions both without smooth muscle activation (passive) and with smooth muscle activated by drugs. In general, the artery shows a hyperelastic passive behaviour which differs with the types of artery due to differences in arterial composition. The atherosclerotic artery tends to be stiffer than the healthy artery and has more heterogeneous mechanical properties due to different components across the plaque (Figure 1.2). Various experimental techniques have been used in the studies, which include *in vitro* inflation and tensile ring tests as well as *in vivo* tests. Images recorded in these experiments are often analysed with computational methods such as digital image correlation and optical flow estimation. Constitutive frameworks and computational modelling have also been used to predict the arterial mechanical behaviour and correlate them with the results of the experiments.

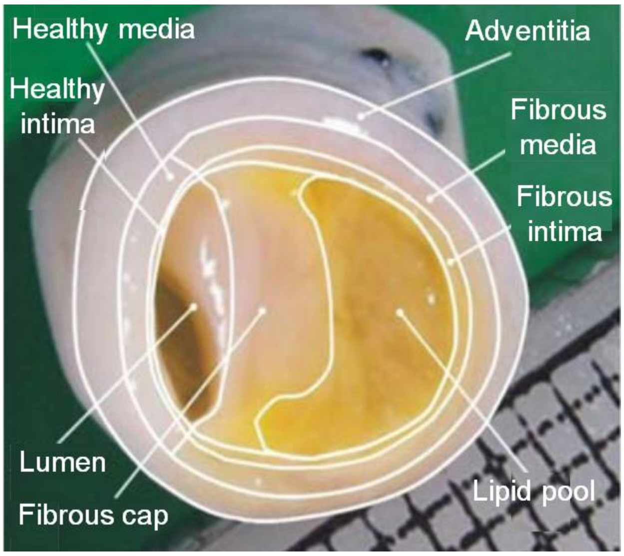

Figure 1.2 Cross-section of an atherosclerotic human iliac artery. (Gasser and Holzapfel 2007)

Despite the widespread studies of arterial biomechanics, more in-depth knowledge of the mechanical properties of the arteries with cardiovascular diseases is needed to develop efficient treatment strategies. Therefore, the thesis aims to develop improved techniques for investigating the passive and active mechanical properties of the atherosclerotic artery. The majority of the thesis focuses on the development of experimental and computational techniques to study the heterogeneous mechanical properties of atherosclerotic arteries and their active function in response to vasoactive agents. The approaches used involved mechanical tests, optical flow image analysis, and finite element modelling, where the mechanical properties of the arteries were determined by matching the results of the experiments with those of the models.

In addition, aortic stiffening induced by systemic inflammation has been studied. This cardiovascular event occurs in several systemic diseases including rheumatoid arthritis, and involves altered function of arterial hyaluronan, a type of glycosaminoglycan on proteoglycan proteins. Therefore, the role of hyaluronan on arterial stiffness was investigated with mechanical tests on hyaluronan-digested rat aortas, and the results were associated with the data of biochemistry assays.

The results of these studies provide information for further understanding the diseased-induced changes of arterial biomechanics, which is useful for future development of treatment strategies. The demonstrated experimental and computational approaches can also be used in future research studies on the biomechanical properties of both healthy and diseased arteries.

1.2 References

Gasser TC and Holzapfel GA. Modeling plaque fissuring and dissection during balloon angioplasty intervention. *Ann Biomed Eng*. 35(5):711-723, 2007.

Libby P. Atherosclerosis: the new view. *Sci Am*. 286(5):46-55, 2002.

2. Literature Review

2.1 Atherosclerosis

2.1.1 Background

Atherosclerosis (arteriosclerotic vascular disease) is a cardiovascular disease in which lipids accumulate in the inner layer of the arterial wall to form an atherosclerotic plaque (Figure 2.1), which often associates with a chronic inflammatory response in the arterial wall (Falk 1991). The atherosclerotic plaque can be classified into stable and vulnerable plaque. The stable plaque is rich in extracellular matrix (ECM) and smooth muscle cells, whereas the vulnerable plaque is composed mainly of lipids and macrophages, with a thin fibrous cap (Falk et al. 1995). Therefore, the vulnerable plaque has higher inflammatory response and is more prone to rupture. The rupture of the atherosclerotic plaque exposes its components to the bloodstream and induces thrombus formation, which can lead to the occlusion of downstream arteries. This thrombosis event in the coronary artery causes myocardial infarction (heart attack), and the same event in the carotid artery causes stroke (Falk et al. 1995, Falk 1999, Davies 2000).

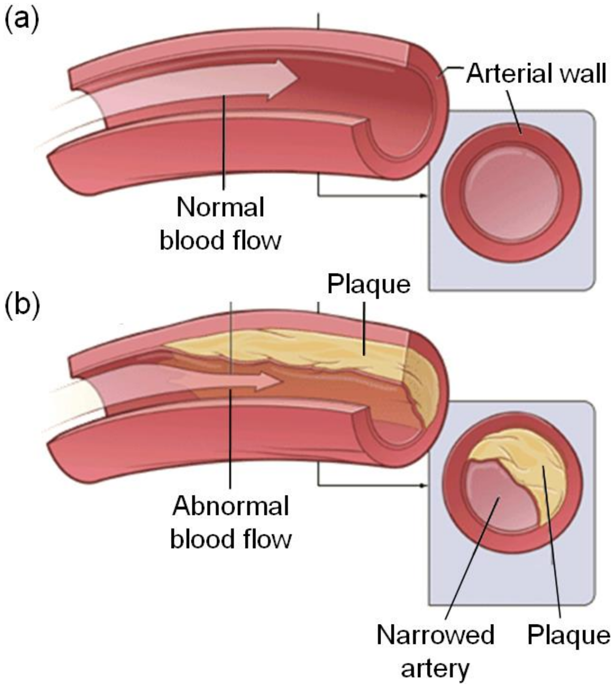

Figure 2.1 (a) A healthy artery and (b) the formation of atherosclerotic plaque in the arterial lumen. (Figure taken from NIH website, see the reference in Section 2.7)

2.1.2 Factors that stimulate atherosclerotic plaque rupture

Studies have suggested that the risk of atherosclerotic plaque rupture is determined by the composition of the plaque and external mechanical factors (Falk et al. 1995, Pasterkamp and Falk 2000). The risk of rupture is higher for a plaque with a higher lipids proportion in the core (Gertz and Roberts 1990, Davies et al. 1993), thinner fibrous cap (Loree et al. 1992), or higher degree of inflammation (Lendon et al. 1991, Moreno et al. 1994). External mechanical loads such as arterial stretching during systole or contraction during diastole and the blood pressure can contribute to a stress concentration on the plaque and increase the risk of plaque rupture (Muller et al. 1989). On the other hand, research has shown that the risk of plaque rupture does not directly correlate with the size of the plaque (Mann and Davies 1996).

2.1.3 Prevention of atherosclerotic plaque rupture

The atherosclerotic plaque could be stabilised by increasing the strength of the plaque or reducing the mechanical loads to prevent the plaque rupture (Kovanen and Pentikäinen 2007). Studies have shown that statins could stabilise the plaque by decreasing inflammation and lipids accumulation in the plaque (Crisby et al. 2001, Martín-Ventura et al. 2005), thereby strengthening it by increasing the ratio of ECM protein to lipids. The efficiency of statins on plaque stabilisation has also been shown clinically (Nissen et al. 2005 and 2006, Ray 2005). Other studies have demonstrated the use of β-blockers (Kaplan et al. 1987, Ostlund-Lindqvist et al. 1988, Hedblad et al. 2001, Wiklund et al. 2002) and calcium antagonists (Pitt et al. 2000, Zanchetti et al. 2002, Nissen et al. 2004) to stabilise the plaque and reduce the progress of atherosclerosis, which potentially achieve these by changing the mechanical behaviour of vascular smooth muscle cells.

2.2 Arterial Biomechanics

2.2.1 Arterial geometry

The arterial geometry varies with the type and location of the artery. In general, arteries can be classified into elastic and muscular arteries. Elastic arteries have relatively large diameters and are closer to the heart, whereas muscular arteries have smaller diameters and are closer to arterioles (Holzapfel et al. 2000). All arteries consist of three layers: intima, media, and adventitia (Figure 2.2). The innermost intima layer consists of a single-layer of endothelial cells; the middle media layer consists of vascular smooth muscle cells, collagen, and elastin, with ground substance matrix containing proteoglycans; and the outermost adventitia layer consists primarily of collagen, with some elastin and fibroblasts (Holzapfel et al. 2000). Most of these collagen fibres have helical orientation which prevents over-distension of the arteries (Figure 2.2). These three layers are separated by thin layers of internal elastic lamina.

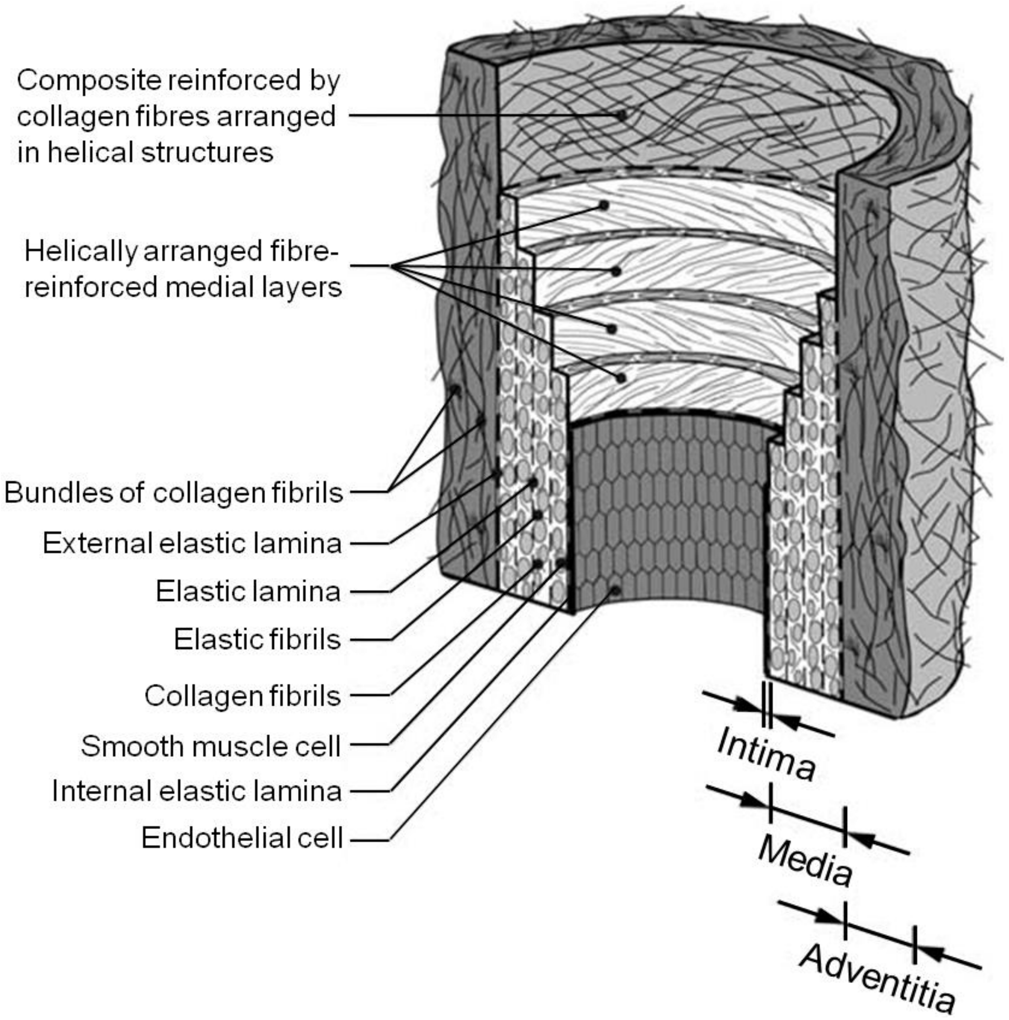

Figure 2.2 The cross-sectional geometry of an artery, showing the components in intima, media, and adventitia layers. (Holzapfel et al. 2000)

While the different orientations of cells and fibres in the media and adventitia layers show an anisotropic structure, Patel and Fry (1969) suggested that the biomechanical response of the artery is cylindrically orthotropic with symmetric planes perpendicular to the radial, circumferential, and axial directions of the artery, thus having the same mechanical properties along the circular layers and the axial direction. This is consistent with later work by Demiray and Vito (1991), which shows that the media layer is cylindrical orthotropic. In atherosclerotic disease condition, the plaque starts developing with the thickening of the intima layer, and may disrupt the media and adventitia layers in a later stage (Akyildiz et al. 2014).

2.2.2 Passive mechanical properties

The passive mechanical properties of the artery, in the absence of smooth muscle tone, are determined by the arterial ECM protein which is mainly composed of collagen and elastin (Holzapfel et al. 2000). The recruitment of the wavy collagen fibrils leads to the nonlinear passive properties of the artery, which differ between axial and circumferential directions (Roach and Burton 1957). Similar to most soft tissues, an increase in extension stiffens the artery in the passive condition, which results in a hyperelastic behaviour (Figure 2.3, open circles). Roach and Burton (1957) suggested that elastin is responsible for the low pressure passive response, whereas collagen is responsible for the high pressure response. Another study from Burton (1954) suggested that media and adventitia, but not intima, contribute to the load-carrying capability of the artery. In addition, von Maltzahn *et al.* (1981) reported that the media layer is stiffer and more nonlinear than the adventitia. Therefore, the passive mechanical properties of artery vary with type and location (Figure 2.3) due to differences in the media and adventitia thicknesses which lead to the variations in the overall orientation and composition of ECM protein.

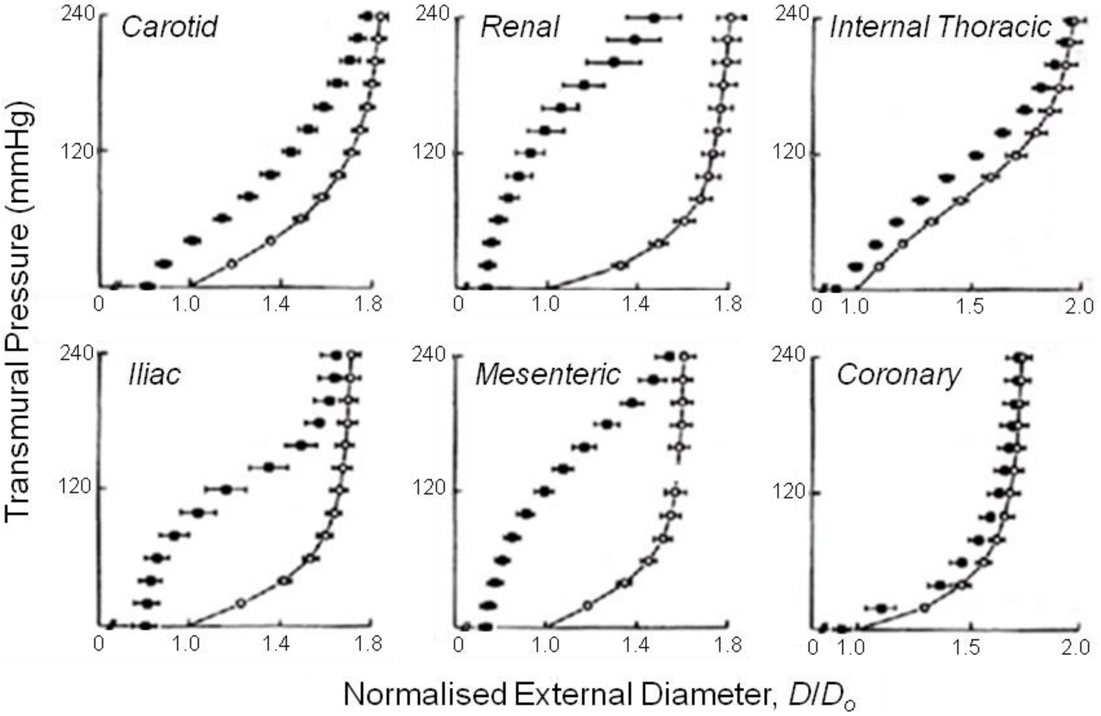

Figure 2.3 Active (closed circles) and passive (open circles) pressure-diameter behaviour of various arteries. (Humphrey 2002 taken from Cox 1978)

Artery is often assumed to be incompressible in experimental and theoretical studies. Carew *et al.* (1968) found that the ratio of the arterial bulk to shear modulus is on the order of 10^3, justifying this assumption in the context of the linearised theory. Lawton (1954) and Dobrin and Rovick (1969) also suggested the validity of this incompressibility assumption by showing that arteries deformed isochorically under various applied loads. In addition, Chuong and Fung (1984) justified this assumption by showing little fluid exudation of arteries while being loaded with a compressive radial stress.

Arteries have residual stress, the stress that exists in the wall in the absence of external loads. The effects of the residual stress on arterial mechanical properties have been discussed by Chuong and Fung (1986) and Takamizawa and Hayashi (1987). In addition, arteries have significant viscoelastic properties, thus exhibiting hysteresis under cyclic loading, stress relaxation under constant deformation, creep under constant load, and strain rate-dependent behaviour (Fung et al. 1979). Despite this, the strain rate-dependent property of an artery is relatively insignificant, where a 1000-fold increase in the loading frequency usually changes the stress-strain relationship by a factor less than two (Collins and Hu 1972, Fung et al. 1979). This characteristic is similar to other soft tissues as discussed by Fung (1984). An artery subjected to a cyclic loading shows stress softening in the first few cycles, which diminishes with the number of load cycles until exhibiting a nearly repeatable cyclic response where the artery is considered preconditioned and can be regarded as pseudoelastic (Fung et al. 1979).

2.2.3 Active mechanical properties

The active mechanical properties of artery are mainly contributed by vascular smooth muscle cells, which comprise about 25% to 60% of the arterial wall by dry weight (Milnor 1990). KCl and norepinephrine are the most commonly used vasoconstrictors in *in vitro* studies to stimulate arterial active response. Vascular smooth muscle contracts when exposed to KCl ≥ 10 to 30 mM, and achieve a maximum response at ≥ 50 to 80 mM (Humphrey 2002). In the same way as the skeletal muscle, vascular smooth muscle generates its maximum force ($F_{\max}$) at a specific stretch or length ($L_{\max}$)

(Figures 2.4 and 2.5) (Price et al. 1981). At a length less than or greater than $L_{\max}$, the force generated by the muscle cells is less than $F_{\max}$.

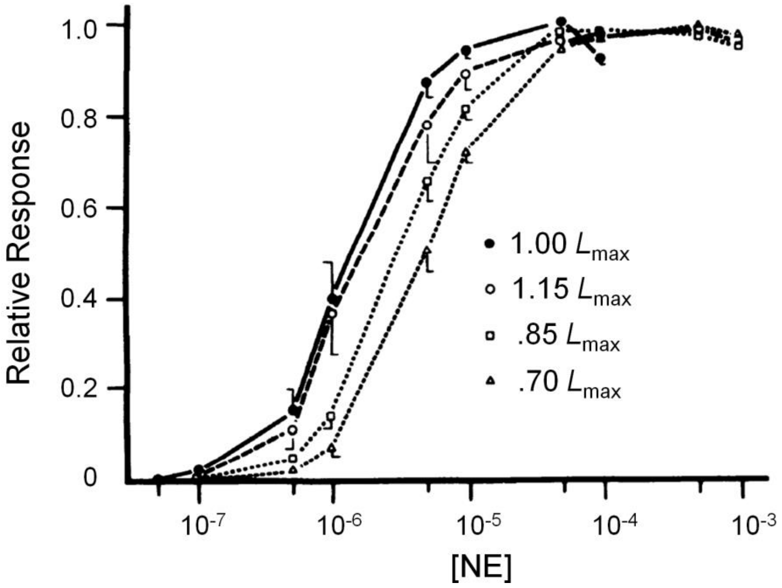

Figure 2.4 An example dose-response curves of vascular smooth muscle. [NE]: norepinephrine concentration. (Humphrey 2002 taken from Price et al. 1981)

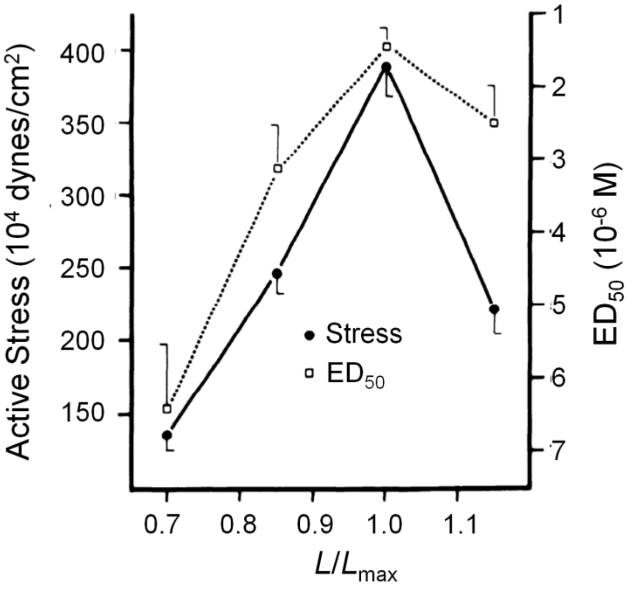

Figure 2.5 Active stress of vascular smooth muscle in response to mechanical stretch and norepinephrine activation. ED_{50}: median effective dose. (Humphrey 2002 taken from Price et al. 1981)

Cox (1978) has shown that the mechanical behaviour of arteries activated by vasoconstrictors is significantly different from their passive behaviour (Figure 2.3). Cox's results show that the muscle response curves obtained by subtracting the passive response from the active response show a maximum stress at a specific diameter (Figure 2.6), which is consistent with the finding of Price *et al.* (1981) in Figure 2.5.

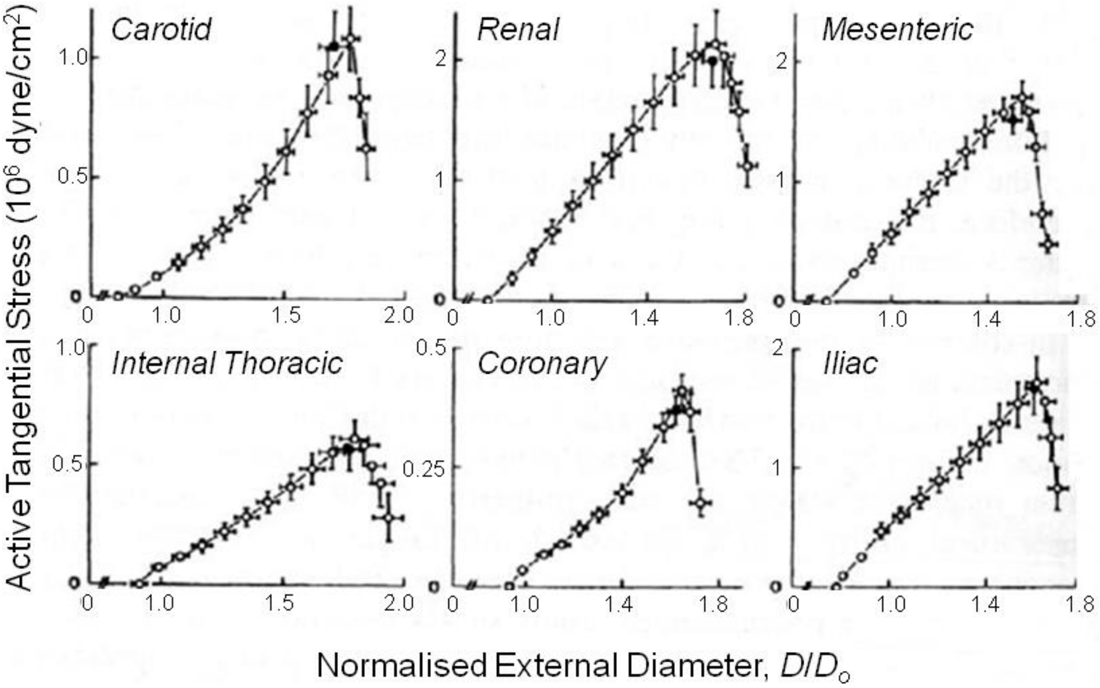

Figure 2.6 Active response of various arteries determined by subtracting the passive from the active responses shown in Figure 2.3. (Humphrey 2002 taken from Cox 1978)

2.2.4 Biomechanics of atherosclerotic artery

Studies have shown that the atherosclerotic artery is significantly stiffer than the healthy artery in *in vitro* uniaxial tension (Band et al. 1973, Pynadath and Mukherjee 1977. Hasegawa and Watanabe 1988) and inflation tests (Cox and Detweiler 1979) and *in vivo* clinical studies (van Popele et al. 2001, Wykretowicz et al. 2009). Sherebrin *et al.* (1987) showed a decreased tensile failure stretch, and Hasegawa and Watanabe (1988) showed increased stress relaxation behaviour in atherosclerotic aortas. Cox and Detweiler (1979) showed that the muscle active force of the diseased iliac artery was lower than that of the healthy artery. In addition, the atherosclerotic plaque has been shown to have heterogeneous mechanical properties which vary between the lipid core, fibrous tissue, and calcified regions of the plaque (Beattie et al. 1998).

2.3 Experimental Techniques

2.3.1 Inflation test

The pressure-diameter inflation test is commonly performed for *in vitro* study of arterial biomechanical properties due to its loading mode and arterial deformation that mimic the physiological pressurisation conditions. The test is typically carried out by mounting an artery onto two cannulas, with one end fixed and the other end adjusted to the desired axial extension; see the example setup from Takamizawa and Hayashi (1987) in Figure 2.7. A load cell is usually connected to the cannula to measure the axial force. During the test, the lumen of the artery is loaded with incremental step or cyclic pressures using a pump. The applied pressure is measured by a pressure transducer located near the cannula. The changes in arterial diameter are recorded with images or video using a camera, which can be connected to a computer for direct recording. The inflation test can be controlled by programming software on a computer to handle more complex loading modes (Vito and Hickey 1980, Humphrey et al. 1993). For cyclic inflation, the pressurisation can be programmed to have the frequency that mimics the pulsatility of physiological condition, but slow and steady inflation is typically used due to the challenges of setting a high frequency test especially for the cases of small animals that have high heart rates.

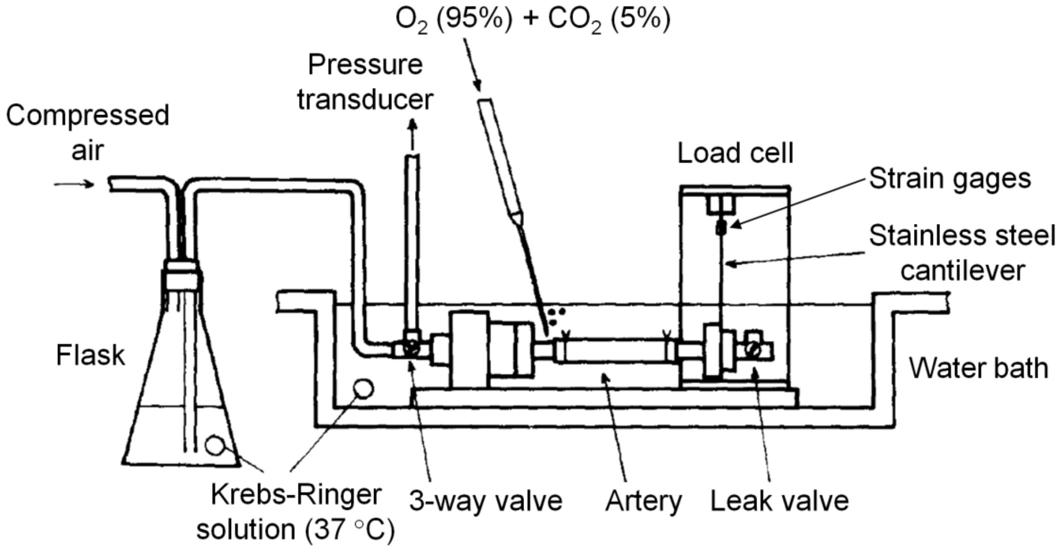

Figure 2.7 An example setup of an inflation test. (Takamizawa and Hayashi 1987)

2.3.2 Tensile ring test

The tensile ring test is conducted by applying uniaxial or biaxial loading on an artery ring that is mounted onto loading arms, and recording the reaction forces with a force transducer. In a uniaxial test, the artery ring is stretched with one-directional loading as seen in the studies of Cox (1982, 1983) and Consigny *et al.* (1986) (Figure 2.8). While having the advantages of simpler setup and enabling the examination of arterial cross-sectional deformation, the ring test has the limitation of not mimicking the physiological pressure loading. In some studies (Lawton 1954, Sherebrin et al. 1987, Teng et al. 2009), tensile tests of cut arterial strips were performed instead of using artery rings. This methodology usually aims to determine the micromechanics of the sample, but is more difficult to relate to physiological loading due to its non-physiological sample geometry.

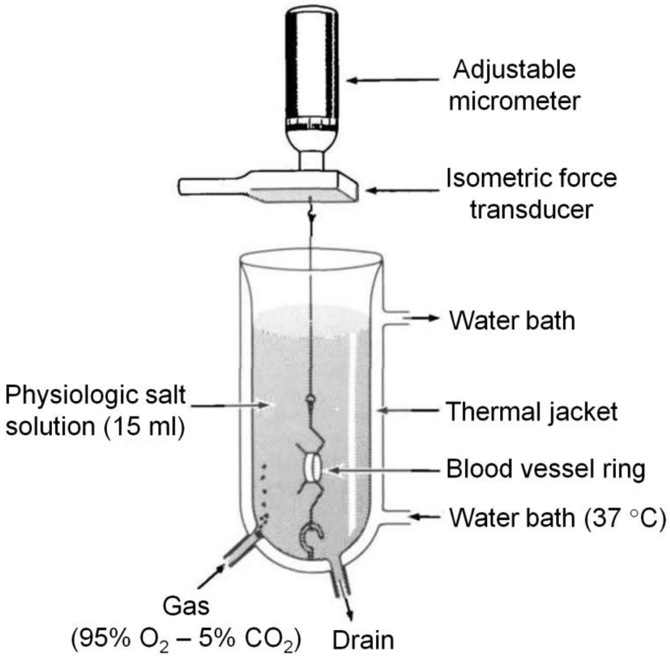

Figure 2.8 An example setup of a tensile ring test. (Consigny et al. 1986)

2.3.3 *In vivo* test

Data from *in vivo* studies are obtained clinically or from experiments on live animals. In an *in vivo* test, the primary measureable properties are blood pressure and arterial geometry. The blood pressure is typically measured invasively using an intramural catheter and pressure transducer, or noninvasively using tonometric methods for the vessels that are close to the skin surface (Hayashi 1993). The measurements of arterial geometry are often performed invasively using angiography or intravascular ultrasound (IVUS) (Hodgson et al. 1993), or noninvasively using computed tomography (CT) (Budoff et al. 1996) or magnetic resonance imaging (MRI) (Mohiaddin et al. 1989). These blood pressure and arterial geometry can be used to compute the *in vivo* cross-sectional compliance of an artery as the change of lumen area divided by the pulse pressure. The measured pressure waves can also be used to determine the pulse wave velocity for representing the arterial stiffness (O’Rourke et al. 2001). While providing direct physiological information that relates to specific diseases, the data collected from the *in vivo* studies are often limited by the accessible technology. The studies also involved more sophisticated equipment and strict regulations.

2.4 Analysis of Experimental Images

2.4.1 Digital image correlation

Various image analysis techniques have been used to correlate the motion of biological components between two images. Among these techniques, digital image correlation has been widely used to measure the local deformation of biological tissue. This technique allows full-field analysis of tissue deformation by employing tracking and image registration methods (Sutton et al. 2009). It tracks the pixel intensity patterns of the images in specified neighbourhoods, and finds an appropriate mapping which maximises the correlation coefficient between corresponding images. Many experimental studies of the mechanical properties of biological tissue have involved the use of digital image correlation, which includes studies on skeletal (McKinley and Bay 2003, Verhulp et al. 2004, Mann et al. 2009) and cardiovascular systems (Zhang et al. 2002, Zhang and Arola 2004, Sutton et al. 2008). However, significant discrepancies may exist between the deformations calculated using this technique and the actual deformations. As discussed by Schierer's (2000, 2002) and Haddadi's (2008) research groups, the accuracy of the correlation closely related to the quality of the measurement devices and environment such as the lighting and the presence of out-of-plane displacement, as well as the correlation principle such as the correlation functions, the speckle pattern, and the sizes of subset and strain grid, where an inappropriate choice of these factors would result in a high correlation error.

2.4.2 Optical flow estimation

Another image analysis technique that has become commonly used in biomechanics experiments is optical flow estimation. The details of this methodology have been described by Fleet and Weiss in (Paragios et al. 2006). In short, optical flow is the pattern of intensity movements in an image, which arises from the relative motion between an object and the observer. The sequence of ordered images allows the estimation of the motion as either instantaneous velocities or discrete displacements of the object. The optical flow estimation assumes constant intensity I for a changing time δt and changing locations δx and δy:

$$I(x, y, t) = I(x + \delta x, y + \delta y, t + \delta t) \tag{2.1}$$

Using the Taylor series approximation, Equation (2.1) results in

$$I_x u + I_y v + I_t = 0 \tag{2.2}$$

where u and v are the x and y components of the optical flow velocity; I_x, I_y, and I_t are the derivatives of the intensity with respect to the changes of x and y positions and time, respectively. Hence optical flow estimation is a differential method using the partial derivatives of pixel intensity with respect to spatial and temporal coordinates to track the motion.

2.4.2.1 Horn-Schunck method

Since the displacement or velocity field of each pixel has two spatial components in the horizontal and vertical directions, an additional constraint is required in addition to the constant intensity to compute the optical flow. Therefore, various methods have been suggested to introduce different constraints for capturing the pixel motion. Among these studies, the method developed by Horn and Schunck (1981) has been well known and widely used as the basis for more advanced approaches (Black and Anandan 1996, Bruhn et al. 2005, Sun et al. 2010).

As a summary of the Horn-Schunck method described in (Horn and Schunck 1981), this method minimises distortions in the flow by assuming the velocities of pixels vary smoothly over the entire image; this smoothness constraint is expressed by minimising the square of the velocity gradient. This method yields a high density of flow vectors and fills in flow information that is missing in the inner parts of homogeneous objects from the motion of the surrounding area. In order to achieve this, it minimises the sum of the error of the constant intensity constraint

$$E_I = I_x u + I_y v + I_t \tag{2.3}$$

and the error of the smoothness constraint

$$E_s{}^2 = \left(\frac{\partial u}{\partial x}\right)^2 + \left(\frac{\partial u}{\partial y}\right)^2 + \left(\frac{\partial v}{\partial x}\right)^2 + \left(\frac{\partial v}{\partial y}\right)^2 \tag{2.4}$$

Therefore, the total error to be minimised is

$$E^2 = \iint (\alpha^2 E_s{}^2 + E_I{}^2)\, dxdy \tag{2.5}$$

where α is a regularisation constant with larger α leading to a smoother flow. Using the calculus of variation and the approximation to the Laplacian to solve for *u* and *v*, the following equations are obtained:

$$\begin{gathered}(\alpha^2 + I_x{}^2 + I_y{}^2)u = \left(\alpha^2 + I_y{}^2\right)\bar{u} - I_x I_y \bar{v} - I_x I_t \\ (\alpha^2 + I_x{}^2 + I_y{}^2)v = \left(\alpha^2 + I_x{}^2\right)\bar{v} - I_x I_y \bar{u} - I_y I_t\end{gathered} \tag{2.6}$$

where $\bar{u}$ and $\bar{v}$ are the weighted average of *u* and *v* for neighbourhood pixels. Since the solution depends on the neighbouring values of the flow field, the calculations of the velocities are repeated with iterative equations below, where *n* and *n* + 1 are the iteration steps:

$$\begin{gathered}u^{n+1} = \bar{u}^n - \frac{I_x(I_x\bar{u}^n + I_y\bar{v}^n + I_t)}{\alpha^2 + I_x{}^2 + I_y{}^2} \\ v^{n+1} = \bar{v}^n - \frac{I_y(I_x\bar{u}^n + I_y\bar{v}^n + I_t)}{\alpha^2 + I_x{}^2 + I_y{}^2}\end{gathered} \tag{2.7}$$

The Horn-Schunck method works for images that are quantised coarsely in space and time. However, its quadratic formulation is not robust to outliers, thus it is more sensitive to noise than some other optical flow methods. In order to solve this issue, Sun *et al.* (2010) have developed an improved optical flow estimation method based on the Horn-Schunck algorithm.

2.4.2.2 *Sun's method*

In the study of Sun *et al.* (2010), they investigated the reasons for improved accuracy for the optical flow estimation with various techniques derived from the Horn-Schunck method. As described in (Sun et al. 2010), they developed a baseline function called "classical", and compared the influences of various factors on improving the accuracy of this function. The classical objective function is shown in Equation (2.8):

$$\begin{aligned} E(\mathbf{u},\mathbf{v}) = \sum_{i,j} \Big\{ \rho_D \left(I_1(i,j) - I_2(i + u_{i,j}, j + v_{i,j}) \right) \\ + \lambda \big[\rho_S(u_{i,j} - u_{i+1,j}) + \rho_S(u_{i,j} - u_{i,j+1}) \\ + \rho_S(v_{i,j} - v_{i+1,j}) + \rho_S(v_{i,j} - v_{i,j+1}) \big] \Big\} \end{aligned} \tag{2.8}$$

where I_1 and I_2 represent the two corresponding images, λ is a regularisation parameter, and ρ_D and ρ_S are the data and spatial penalty functions. Among the factors investigated, they determined that applying a median filter to the intermediate flow values during incremental estimation and warping provides the most significant improvement by removing outliers.

Median filtering is a commonly used technique in digital image processing for reducing noise and outliers in a smooth distribution of pixels while retaining edge sharpness (Russ 2011). For a selected neighbourhood of a square kernel with $m \times m$ pixels, the median filter replaces the pixel at the centre of the kernel with the median of all pixel values in this neighbourhood, thus removing an outlier. An example is shown in Figure 2.9, where the median value of the nine pixels in the 3 × 3 kernel is 3. Using a median filter, the outlier at the centre of the kernel is replaced by this median value and the distribution of pixels becomes smooth.

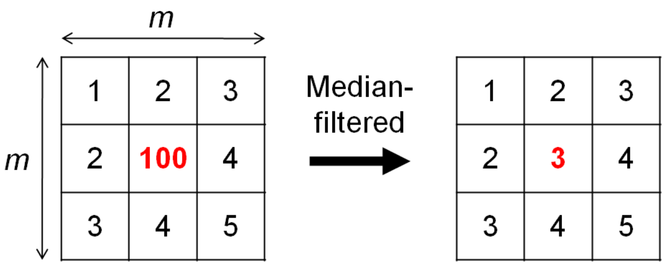

Figure 2.9 A median filter replaces the pixel at the centre of a 3 × 3 kernel ($m = 3$) with the median value of the nine pixels in the kernel.

While this median filtering improves the accuracy of the flow fields in Sun's study, it increases the energy of the objective function. This suggests that optimisation of the classical objective with median filtering approximately minimises the function in Equation (2.9):

$$\begin{aligned} E_A(\mathbf{u}, \mathbf{v}, \hat{\mathbf{u}}, \hat{\mathbf{v}}) = \sum_{i,j} \Big\{ \rho_D \left(I_1(i,j) - I_2\left(i + u_{i,j}, j + v_{i,j}\right)\right) \\ + \lambda\left[\rho_S\left(u_{i,j} - u_{i+1,j}\right) + \rho_S\left(u_{i,j} - u_{i,j+1}\right) \right. \\ \left. + \rho_S\left(v_{i,j} - v_{i+1,j}\right) + \rho_S\left(v_{i,j} - v_{i,j+1}\right)\right]\Big\} \\ + \lambda_2(\|\mathbf{u} - \hat{\mathbf{u}}\|^2 + \|\mathbf{v} - \hat{\mathbf{v}}\|^2) \\ + \sum_{i,j} \sum_{(i',j') \in N_{i,j}} \lambda_3\left(\left|\hat{u}_{i,j} - \hat{u}_{i',j'}\right| + \left|\hat{v}_{i,j} - \hat{v}_{i',j'}\right|\right) \end{aligned} \tag{2.9}$$

where $\hat{\mathbf{u}}$ and $\hat{\mathbf{v}}$ denote an auxiliary flow field, $N_{i,j}$ is the set of neighbours of pixel (i, j) in a possibly large area, and λ_2 and λ_3 are scalar weights. The term in braces (the first three lines) is the same as Equation (2.8), and the last term (the fifth line) is a new non-local term added to the original function with a coupling term (the fourth line) encouraging $\hat{\mathbf{u}}$, $\hat{\mathbf{v}}$ and $\mathbf{u}$, $\mathbf{v}$ to be the same. This non-local term represents the median filtering heuristic, which imposes a particular smoothness assumption within a specified flow region.

Sun *et al.* introduced the non-local and coupling terms to the original objective, and optimised the new objective by alternately minimising the following two functions:

$$\begin{aligned}E_O(\mathbf{u},\mathbf{v}) = \sum_{i,j} \Big\{ \rho_D\Big(I_1(i,j) - I_2(i+u_{i,j}, j+v_{i,j})\Big) \\ + \lambda\big[\rho_S(u_{i,j}-u_{i+1,j}) + \rho_S(u_{i,j}-u_{i,j+1}) + \rho_S(v_{i,j}-v_{i+1,j}) \\ + \rho_S(v_{i,j}-v_{i,j+1})\big]\Big\} + \lambda_2(\|\mathbf{u}-\hat{\mathbf{u}}\|^2 + \|\mathbf{v}-\hat{\mathbf{v}}\|^2)\end{aligned} \tag{2.10}$$

$$\begin{aligned}E_M(\hat{\mathbf{u}},\hat{\mathbf{v}}) = \lambda_2(\|\mathbf{u}-\hat{\mathbf{u}}\|^2 + \|\mathbf{v}-\hat{\mathbf{v}}\|^2) \\ + \sum_{i,j} \sum_{(i',j')\in N_{i,j}} \lambda_3\big(|\hat{u}_{i,j}-\hat{u}_{i',j'}| + |\hat{v}_{i,j}-\hat{v}_{i',j'}|\big)\end{aligned} \tag{2.11}$$

With these terms, minimisation of the new objective function approximates the original optimisation with the median filtering step. This new objective function robustly integrates flow estimates over large spatial neighbourhoods.

In addition, Sun *et al.* incorporated the image structure and flow boundaries into a weighted version of the non-local term to prevent over-smoothing across boundaries, thus reducing the errors produced by median filtering.

$$\sum_{i,j} \sum_{(i',j')\in N_{i,j}} w_{i,j,i',j'}\big(|\hat{u}_{i,j}-\hat{u}_{i',j'}| + |\hat{v}_{i,j}-\hat{v}_{i',j'}|\big) \tag{2.12}$$

The $w_{i,j,i',j'}$ is the weight that represents the likelihood of the pixel (i', j') belonging to the same surface as pixel (i, j). Overall, Sun's method provides significant improvement for the optical flow estimation, and has ranked at the top of the Middlebury benchmark during the publication of the work in 2010. The MATLAB functions of this method are available on the web (Sun 2010).

2.5 Theoretical Models

Theoretical models have been used for sophisticated analysis of the mechanical properties of arteries. The modelling can be performed mathematically as constitutive frameworks or with computational finite element (FE) models, where the results can be correlated to experimental data.

2.5.1 Constitutive frameworks

Fung *et al.* (1979) have developed a classical strain-energy function that has been used extensively in modelling the passive mechanical behaviour of arteries. They used the pseudoelastic strain energy function in Equation (2.13) to approximate the stress-strain relationship of the artery subjected to the internal pressure and longitudinal stretch within the physiological range.

$$\psi = \frac{c}{2}\exp\left[a_1\left({E_{\theta\theta}}^2 - {E^*_{\theta\theta}}^2\right) + a_2\left({E_{zz}}^2 - {E^*_{zz}}^2\right) + 2a_4\left(E_{\theta\theta}E_{zz} - E^*_{\theta\theta}E^*_{zz}\right)\right] \quad (2.13)$$

c, a_1, a_2, and a_4 are material constants; $E_{\theta\theta}$ and E_{zz} are the circumferential and axial strains where $E^*_{\theta\theta}$ and E^*_{zz} are the strains that correspond to the reference stresses $S^*_{\theta\theta}$ and S^*_{zz} selected arbitrarily often from the physiologic range. The two-dimensional stresses $S_{\theta\theta}$ and S_{zz} can be obtained by differentiating the energy function with respect to $E_{\theta\theta}$ and E_{zz}, respectively.

In a later work of Fung's group, they generalised this function to the three-dimensional (3D) regime (Chuong and Fung 1983), assuming that the principal stresses are in the radial, circumferential, and axial directions of the artery. Deng *et al.* (1994) proposed an extension model of Fung’s classical function to incorporate the shear deformation of the artery. In addition, Humphrey (1995) has also generalised Fung’s function to be 3D and incorporated shear deformations as shown in Equations (2.14) and (2.15), where the number of non-dimensional material parameters, a_i for $i = 1, 2, \ldots,$ and 9, has been increased for the additional radial direction and shear strains of the artery.

$$\psi = \frac{1}{2}c[\exp(Q) - 1] \tag{2.14}$$

$$\begin{aligned} Q = a_1 {E_{\theta\theta}}^2 + a_2 {E_{ZZ}}^2 + a_3 {E_{RR}}^2 + 2a_4 E_{\theta\theta} E_{ZZ} + 2a_5 E_{ZZ} E_{RR} \\ + 2a_6 E_{RR} E_{\theta\theta} + a_7 {E_{\theta Z}}^2 + a_8 {E_{RZ}}^2 + a_9 {E_{R\theta}}^2 \end{aligned} \tag{2.15}$$

In more recent years, Holzapfel *et al.* (2000) developed an improved constitutive framework to study the passive mechanical behaviour of the arterial wall, aiming to solve the mechanical, mathematical, and computational deficiencies of the previous models such as parameter identification problems and oversimplification of the arterial geometry or mechanical properties. They modelled the artery as an incompressible, cylindrical thick-walled tube with two layers representing the media and adventitia. The relatively thin intima layer was assumed to have negligible effects on the mechanical properties of healthy arteries. The two layers were treated as fibre-reinforced materials that correspond to collagen fibres, which are symmetrically oriented with respect to the cylindrical axis. Two different 3D strain-energy functions with isotropic and anisotropic components were used for the two layers, resulting in different orthotropic behaviours in each layer. The expressions of the function are shown in Equations (2.16), (2.17), and (2.18), where $\mathbf{C}$ is the right Cauchy-Green deformation tensor; I_1, I_4, and I_6 are the invariants determined as in Equation (2.19); $\mathbf{A}_i$ are the tensor products of $\mathbf{a}_i \otimes \mathbf{a}_i$ for $i = 1, 2$ and $\mathbf{a}_i$ are the two direction vectors that characterise the orientation of collagen fibres. The c and k_1 are stress parameters and k_2 is a dimensionless parameter. The two layers are assigned with different parameters, resulting in a total of six parameters of c, k_1, and k_2 for both media and adventitia.

$$\psi(\mathbf{C}, \mathbf{A}_1, \mathbf{A}_2) = \psi_{\text{iso}}(I_1) + \psi_{\text{aniso}}(I_4, I_6) \tag{2.16}$$

$$\psi_{\text{iso}}(I_1) = \frac{c}{2}(I_1 - 3) \tag{2.17}$$

$$\psi_{\text{aniso}}(I_4, I_6) = \frac{k_1}{2k_2} \sum_{i=4,6} \left\{ \exp[k_2(I_i - 1)^2] - 1 \right\} \tag{2.18}$$

$$I_1(\mathbf{C}) = \text{tr}(\mathbf{C}) \qquad I_4(\mathbf{C}, \mathbf{a}_1) = \mathbf{C} : \mathbf{A}_1 \qquad I_6(\mathbf{C}, \mathbf{a}_2) = \mathbf{C} : \mathbf{A}_2 \tag{2.19}$$

In order to validate the model, Holzapfel *et al.* (2000) fitted the model with experimental test data for arteries under combined axial extension, inflation, and torsion. The effect of residual stress on the stress distribution in arterial wall was also examined.

In later works, this constitutive framework was extended to include the viscoelastic regime (Holzapfel et al. 2002) and the effects of non-atherosclerotic intima thickening (Holzapfel et al. 2005). This model was also generalised to include the information of the dispersed collagen orientation in each layer by incorporating an additional scalar structure parameter (Gasser et al. 2006), which allows better representation of the anisotropic properties of arteries.

2.5.2 Computational finite element models

Computational FE modelling has been used to apply the constitutive frameworks to study the structure-function relationships of arteries, especially for the cases of disease-induced changes of biomechanical properties. Some studies involving computational modelling are reviewed here to introduce the techniques relevant to this thesis.

Cheng *et al.* (1993) performed FE modelling to calculate the stress distribution in the atherosclerotic artery, and have shown that the ruptured atherosclerotic plaques have a higher number of stress concentration regions than the stable plaques, which coincided well with the rupture sites and have significantly higher circumferential stresses (Figure 2.10).

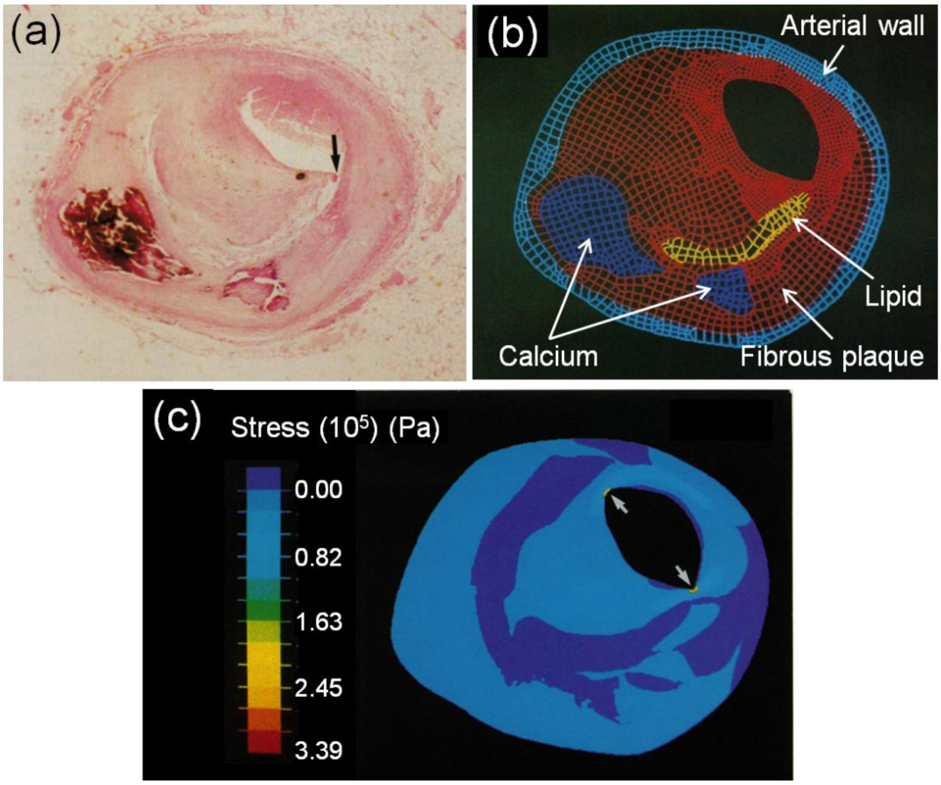

Figure 2.10 (a) Histology of an atherosclerotic artery; arrow indicates the location of plaque rupture. (b) Finite element mesh of the atherosclerotic artery showing the regions of different components. (c) Colour contour of the circumferential stress in the model; arrows indicate high stress regions. (Cheng et al. 1993)

Baldewsing *et al*. (2005, 2008) developed a technique that was used to determine the elastic modulus of the atherosclerotic artery and plaque, which reconstructed images of elastogram using a parametric FE model and iteratively changed the plaque geometry and material parameters (Figure 2.11).

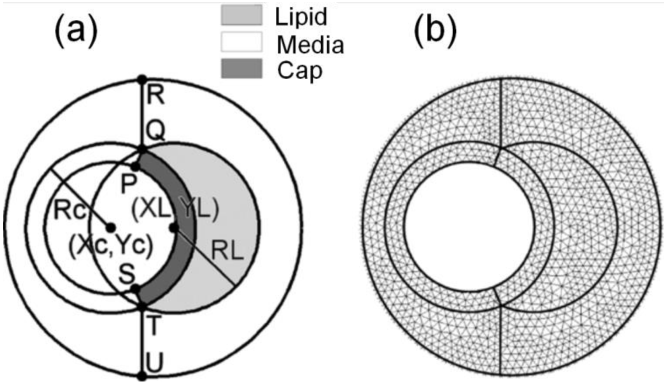

Figure 2.11 Parametric finite element model of an atherosclerotic plaque in the study of Baldewsing *et al*. (2005). (a) Circles used to define different components of the plaque, with centre (X, Y), radius R, and dynamic control points P, Q, R, S, T, and U; letters L and c denote lipid and cap. (b) Finite element mesh of the artery.

Gasser and Holzapfel (2007) used an FE model to trace the fissuring and dissection of the atherosclerotic plaque during balloon angioplasty interventions, assuming the arterial wall to be anisotropic, heterogeneous, highly deformable, and nearly incompressible (Figure 2.12).

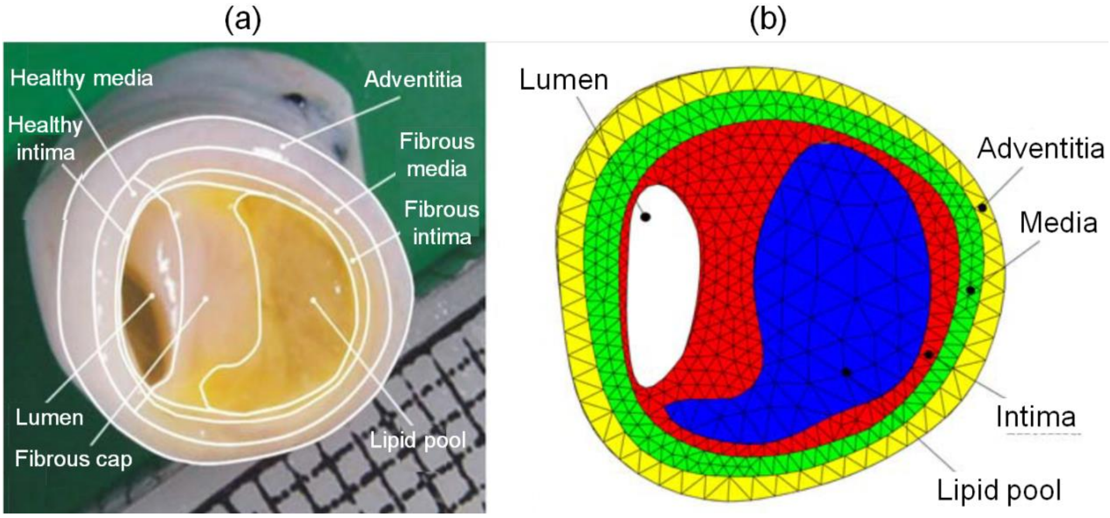

Figure 2.12 (a) Cross-section and (b) finite element model of an atherosclerotic human iliac artery in the study of Gasser and Holzapfel (2007).

In order to noninvasively estimate the mechanical properties of abdominal aortic aneurysm, Raghavan *et al.* (2000) developed an FE technique which reconstructed the 3D geometry of the aneurysm and aorta using *in vivo* data obtained from computed tomography scans (Figure 2.13). From this, they determined the stress distribution on the wall of the aneurysm and aorta under systolic blood pressure.

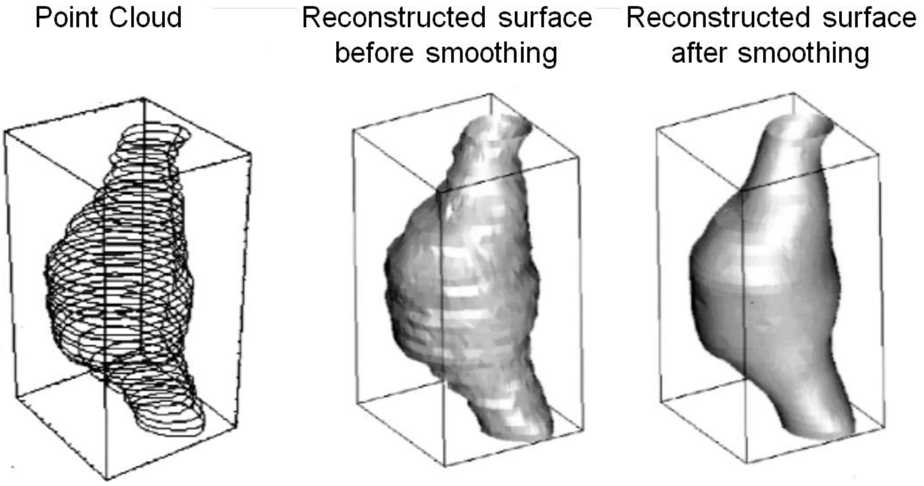

Figure 2.13 Computational reconstruction of an abdominal aortic aneurysm in the study of Raghavan *et al.* (2000).

In addition, Delfino *et al.* (1997) developed a 3D FE model of human carotid artery bifurcation (Figure 2.14). This model was used to study the stress distribution in the bifurcation and the effects of residual strain on it, where the stress field was shown to be more uniform with the existence of the residual strain. The material of the artery was assumed hyperelastic, homogenous, isotropic, and incompressible.

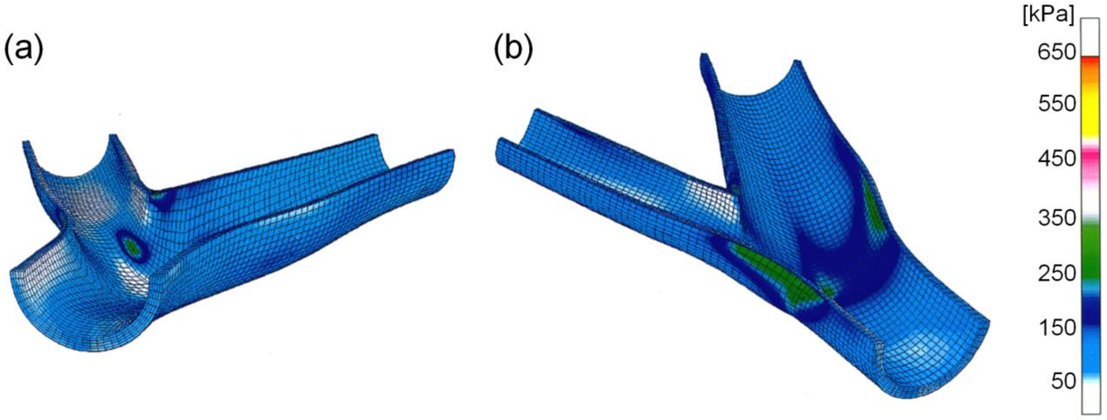

Figure 2.14 Three-dimensional finite element model of human carotid bifurcation in the study of Delfino *et al*. (1997), showing the stress distribution in the arterial wall.

2.5.3 Modelling of arterial active mechanical properties

Most of the theoretical studies of arterial active mechanical properties focus on the constitutive modelling of smooth muscle activation force. Gestrelius and Borgström (1986) developed a one-dimensional dynamic model of smooth muscle contraction based on the sliding of myosin and actin filaments. Having a similar aim, Hai and Murphy (1988) developed a minimum kinetic model for cross-bridge interactions of the thin filaments in smooth muscle cells. Furthermore, Yang *et al.* (2003) proposed a smooth muscle model that consists of electro-chemical and chemo-mechanical components to address the interaction between the electrical, chemical, and mechanical functions of the smooth muscle. More recently, Stålhand *et al.* (2008) formulated a one-dimensional model to study the interaction between the mechanical and biochemical components of the cell activation function. A strain-energy function was used to include the chemical kinetics and nonlinear kinematics of smooth muscle contraction, which incorporated the chemical law of Hai and Murphy (1988) and reduced the function to the model of Yang *et al.* (2003) in the linear limit of small deformations.

While these models enable estimation of the activation force of vascular smooth muscle cells, more work is required to apply them to the modelling of arterial active mechanical behaviour. A phenomenological model is essential to incorporate the effects of the arterial geometry and the coupling of the smooth muscle cells with ECM proteins. In contrast to the smooth muscle cell models, Zulliger *et al.* (2004) proposed a pseudo-strain energy function describing the biomechanical properties of large conduit arteries with active smooth muscle tone. This model incorporates the interactions between mechanical stretch and myogenic contraction, which enables the estimation of the stress distribution in physiological conditions at different levels of smooth muscle tone. However, this model is limited to the assumptions of isotropic muscle sensitivity, linear muscle stress-stretch behaviour, and homogeneous structure across the wall thickness.

2.6 Conclusion

This literature review provides the fundamental knowledge of the physiological and biomechanical properties of artery. While many studies on arterial biomechanics have been performed, the knowledge of the mechanical properties of arteries with cardiovascular diseases is still insufficient to develop efficient treatments for these diseases. This includes the limited accuracy of the determined passive mechanical properties of the atherosclerotic artery and the lack of thorough investigations of the active function of this diseased artery. In addition, the knowledge of the role of ECM proteins other than collagen and elastin, such as proteoglycan and glycosaminoglycan, on diseased-induced changes of arterial stiffness is limited.

Therefore, this thesis aims to develop an improved technique for determining the heterogeneous mechanical properties of the atherosclerotic artery and to better understand the active function of the artery in this diseased condition. Another study has also been performed to investigate the role of hyaluronan, a type of glycosaminoglycan, on systemic inflammation-induced arterial stiffening.

2.7 References

Akyildiz AC, Speelman L, Gijsen FJ. Mechanical properties of human atherosclerotic intima tissue. *J Biomech*. 47(4):773-783, 2014.

Baldewsing RA, Danilouchkine MG, Mastik F, Schaar JA, Serruys PW, van der Steen AF. An inverse method for imaging the local elasticity of atherosclerotic coronary plaques. *IEEE Trans Inf Technol Biomed*. 12(3):277-289, 2008.

Baldewsing RA, Schaar JA, Mastik F, Oomens CW, van der Steen AF. Assessment of vulnerable plaque composition by matching the deformation of a parametric plaque model to measured plaque deformation. *IEEE Trans Med Imaging*. 24(4):514-528, 2005.

Band W, Goedhard WJ, Knoop AA. Comparison of effects of high cholesterol intake on viscoelastic properties of the thoracic aorta in rats and rabbits. *Atherosclerosis*. 18(1):163-171, 1973.

Beattie D, Xu G, Vito R, Glagov S, Whang WG. Mechanical analysis of heterogeneous, atherosclerotic human aorta. *J Biomech Eng*. 120(5):602-607, 1998.

Black MJ and Anandan P. The robust estimation of multiple motions: parametric and piecewise-smooth flow fields. *Comput Vision Image Understanding*. 63(1):75-104, 1996.

Bruhn A, Weickert J, Schnorr C. Lucas/Kanade meets Horn/Schunck: combining local and global optic flow methods. *Int J Comput Vision*. 61(3):211-231, 2005.

Budoff MJ, Georgiou D, Brody A, Agatston AS, Kennedy J, Wolfkiel C, Stanford W, Shields P, Lewis RJ, Janowitz WR, Rich S, Brundage BH. Ultrafast computed tomography as a diagnostic modality in the detection of coronary artery disease: a multicenter study. *Circulation*. 93(5):898-904, 1996.

Burton AC. Relation of structure to function of the tissues of the wall of blood vessels. *Physiol Rev*. 34(4):619-642, 1954.

Carew TE, Vaishnav RN, Patel DJ. Compressibility of the arterial wall. *Circ Res*. 23(1):61-68, 1968.

Cheng GC, Loree HM, Kamm RD, Fishbein MC, Lee RT. Distribution of circumferential stress in ruptured and stable atherosclerotic lesions. A structural analysis with histopathological correlation. *Circulation*. 87(4):1179-1187, 1993.

Chuong CJ and Fung YC. Three-dimensional stress distribution in arteries. *J Biomech Eng*. 105(3):268-274, 1983.

Chuong CJ and Fung YC. Compressibility and constitutive equation of arterial wall in radial compression experiments. *J Biomech*. 17(1):35-40, 1984.

Chuong CJ and Fung YC. On residual stresses in arteries. *J Biomech Eng*. 108(2):189-192, 1986.

Collins R and Hu WC. Dynamic deformation experiments on aortic tissue. *J Biomech*. 5(4):333-337, 1972.

Consigny PM, Tulenko TN, Nicosia RF. Immediate and long-term effects of angioplasty-balloon dilation on normal rabbit iliac artery. *Arteriosclerosis*. 6(3):265-276, 1986.

Cox RH. Passive mechanics and connective tissue composition of canine arteries. *Am J Physiol*. 234(5):H533-H541, 1978.

Cox RH. Comparison of mechanical and chemical properties of extra- and intralobar canine pulmonary arteries. *Am J Physiol*. 242(2):H245-H253, 1982.

Cox RH. Comparison of arterial wall mechanics using ring and cylindrical segments. *Am J Physiol*. 244(2):H298-H303, 1983.

Cox RH and Detweiler DK. Arterial wall properties and dietary atherosclerosis in the racing greyhound. *Am J Physiol*. 236(6):H790-H797, 1979.

Crisby M, Nordin-Fredriksson G, Shah PK, Yano J, Zhu J, Nilsson J. Pravastatin treatment increases collagen content and decreases lipid content, inflammation, metalloproteinases, and cell death in human carotid plaques: implications for plaque stabilization. *Circulation*. 103(7):926-933, 2001.

Davies MJ. The pathophysiology of acute coronary syndromes. *Heart*. 83(3):361-366, 2000.

Davies MJ, Richardson PD, Woolf N, Katz DR, Mann J. Risk of thrombosis in human atherosclerotic plaques: role of extracellular lipid, macrophage, and smooth muscle cell content. *Br Heart J*. 69(5):377-381, 1993.

Delfino A, Stergiopulos N, Moore JE, Jr., Meister JJ. Residual strain effects on the stress field in a thick wall finite element model of the human carotid bifurcation. *J Biomech*. 30(8):777-786, 1997.

Demiray H and Vito RP. A layered cylindrical-shell model for an aorta. *Int J Eng Sci*. 29(1):47-54, 1991.

Deng SX, Tomioka J, Debes JC, Fung YC. New experiments on shear modulus of elasticity of arteries. *Am J Physiol*. 266(1 Pt 2):H1-H10, 1994.

Dobrin PB and Rovick AA. Influence of vascular smooth muscle on contractile mechanics and elasticity of arteries. *Am J Physiol*. 217(6):1644-1651, 1969.

Falk E. Coronary thrombosis: pathogenesis and clinical manifestations. *Am J Cardiol*. 68(7):28B-35B, 1991.

Falk E. Stable versus unstable atherosclerosis: clinical aspects. *Am Heart J*. 138(5 Pt 2):S421-S425, 1999.

Falk E, Shah PK, Fuster V. Coronary plaque disruption. *Circulation*. 92(3):657-671, 1995.

Fung YC. Structure and stress-strain relationship of soft tissues. *Am Zool*. 24(1):13-22, 1984.

Fung YC, Fronek K, Patitucci P. Pseudoelasticity of arteries and the choice of its mathematical expression. *Am J Physiol*. 237(5):H620-H631, 1979.

Gasser TC and Holzapfel GA. Modeling plaque fissuring and dissection during balloon angioplasty intervention. *Ann Biomed Eng*. 35(5):711-723, 2007.

Gasser TC, Ogden RW, Holzapfel GA. Hyperelastic modelling of arterial layers with distributed collagen fibre orientations. *J R Soc Interface*. 3(6):15-35, 2006.

Gertz SD and Roberts WC. Hemodynamic shear force in rupture of coronary arterial atherosclerotic plaques. *Am J Cardiol*. 66(19):1368-1372, 1990.

Gestrelius S and Borgström P. A dynamic model of smooth muscle contraction. *Biophys J*. 50(1):157-169, 1986.

Haddadi H and Belhabib S. Use of rigid-body motion for the investigation and estimation of the measurement errors related to digital image correlation technique. *Opt Lasers Eng*. 46(2):185-196, 2008.

Hai CM and Murphy RA. Cross-bridge phosphorylation and regulation of latch state in smooth muscle. *Am J Physiol*. 254(1 Pt 1):C99-C106, 1988.

Hasegawa M and Watanabe Y. Rheological properties of the thoracic aorta in normal and WHHL rabbits. *Biorheology*. 25(1-2):147-156, 1988.

Hayashi K. Experimental approaches on measuring the mechanical properties and constitutive laws of arterial walls. *J Biomech Eng*. 115(4B):481-488, 1993.

Hedblad B, Wikstrand J, Janzon L, Wedel H, Berglund G. Low-dose metoprolol CR/XL and fluvastatin slow progression of carotid intima-media thickness: main results from the Beta-Blocker Cholesterol-Lowering Asymptomatic Plaque Study (BCAPS). *Circulation*. 103(13):1721-1726, 2001.

Hodgson JM, Reddy KG, Suneja R, Nair RN, Lesnefsky EJ, Sheehan HM. Intracoronary ultrasound imaging: correlation of plaque morphology with angiography, clinical syndrome and procedural results in patients undergoing coronary angioplasty. *J Am Coll Cardiol*. 21(1):35-44, 1993.

Holzapfel GA, Gasser TC, Ogden RW. A new constitutive framework for arterial wall mechanics and a comparative study of material models. *J Elast*. 61(1-3):1-48, 2000.

Holzapfel GA, Gasser TC, Stadler M. A structural model for the viscoelastic behavior of arterial walls: continuum formulation and finite element analysis. *Eur J Mech A/Solids*. 21(3):441-463, 2002.

Holzapfel GA, Sommer G, Gasser CT, Regitnig P. Determination of layer-specific mechanical properties of human coronary arteries with nonatherosclerotic intimal thickening and related constitutive modeling. *Am J Physiol Heart Circ Physiol*. 289(5):H2048-H2058, 2005.

Horn BKP and Schunck BG. Determining optical-flow. *Artif Intell*. 17(1-3):185-203, 1981.

Humphrey JD. Mechanics of the arterial wall: review and directions. *Crit Rev Biomed Eng*. 23(1-2):1-162, 1995.

Humphrey JD. Cardiovascular solid mechanics: cells, tissues, and organs. *Springer*. 2002.

Humphrey JD, Kang T, Sakarda P, Anjanappa M. Computer-aided vascular experimentation: a new electromechanical test system. *Ann Biomed Eng*. 21(1):33-43, 1993.

Kaplan JR, Manuck SB, Adams MR, Weingand KW, Clarkson TB. Inhibition of coronary atherosclerosis by propranolol in behaviorally predisposed monkeys fed an atherogenic diet. *Circulation*. 76(6):1364-1372, 1987.

Kovanen PT and Pentikäinen MO. Pharmacologic prevention of coronary plaque rupture - the major cause of acute coronary syndromes. *Heart Metab*. 36:9-14, 2007.

Lawton RW. The thermoelastic behavior of isolated aortic strips of the dog. *Circ Res*. 2(4):344-353, 1954.

Lendon CL, Davies MJ, Born GV, Richardson PD. Atherosclerotic plaque caps are locally weakened when macrophages density is increased. *Atherosclerosis*. 87(1):87-90, 1991.

Loree HM, Kamm RD, Stringfellow RG, Lee RT. Effects of fibrous cap thickness on peak circumferential stress in model atherosclerotic vessels. *Circ Res*. 71(4):850-858, 1992.

Mann JM and Davies MJ. Vulnerable plaque. Relation of characteristics to degree of stenosis in human coronary arteries. *Circulation*. 94(5):928-931, 1996.

Mann KA, Miller MA, Race A, Verdonschot N. Shear fatigue micromechanics of the cement-bone interface: an in vitro study using digital image correlation techniques. *J Orthop Res*. 27(3):340-346, 2009.

Martín-Ventura JL, Blanco-Colio LM, Gómez-Hernández A, Muñoz-García B, Vega M, Serrano J, Ortega L, Hernández G, Tuñón J, Egido J. Intensive treatment with atorvastatin reduces inflammation in mononuclear cells and human atherosclerotic lesions in one month. *Stroke*. 36(8):1796-1800, 2005.

McKinley TO and Bay BK. Trabecular bone strain changes associated with subchondral stiffening of the proximal tibia. *J Biomech*. 36(2):155-163, 2003.

Milnor WR. Cardiovascular physiology. *Oxford University Press*. 1990.

Mohiaddin RH, Underwood SR, Bogren HG, Firmin DN, Klipstein RH, Rees RS, Longmore DB. Regional aortic compliance studied by magnetic resonance imaging: the effects of age, training, and coronary artery disease. *Br Heart J*. 62(2):90-96, 1989.

Moreno PR, Falk E, Palacios IF, Newell JB, Fuster V, Fallon JT. Macrophage infiltration in acute coronary syndromes. Implications for plaque rupture. *Circulation*. 90(2):775-778, 1994.

Muller JE, Tofler GH, Stone PH. Circadian variation and triggers of onset of acute cardiovascular disease. *Circulation*. 79(4):733-743, 1989.

NIH website. What is atherosclerosis? www.nhlbi.nih.gov/health/dci/Diseases/Atherosclerosis/Atherosclerosis_WhatIs.html, accessed 4 February 2014.

Nissen SE, Nicholls SJ, Sipahi I, Libby P, Raichlen JS, Ballantyne CM, Davignon J, Erbel R, Fruchart JC, Tardif JC, Schoenhagen P, Crowe T, Cain V, Wolski K, Goormastic M, Tuzcu EM. Effect of very high-intensity statin therapy on regression of coronary atherosclerosis: the ASTEROID trial. *JAMA*. 295(13):1556-1565, 2006.

Nissen SE, Tuzcu EM, Libby P, Thompson PD, Ghali M, Garza D, Berman L, Shi H, Buebendorf E, Topol EJ. Effect of antihypertensive agents on cardiovascular events in patients with coronary disease and normal blood pressure: the CAMELOT study: a randomized controlled trial. *JAMA*. 292(18):2217-2225, 2004.

Nissen SE, Tuzcu EM, Schoenhagen P, Crowe T, Sasiela WJ, Tsai J, Orazem J, Magorien RD, O'Shaughnessy C, Ganz P. Statin therapy, LDL cholesterol, C-reactive protein, and coronary artery disease. *N Engl J Med*. 352(1):29-38, 2005.

O'Rourke MF, Pauca A, Jiang XJ. Pulse wave analysis. *Br J Clin Pharmacol*. 51(6):507-522, 2001.

Ostlund-Lindqvist AM, Lindqvist P, Bräutigam J, Olsson G, Bondjers G, Nordborg C. Effect of metoprolol on diet-induced atherosclerosis in rabbits. *Arteriosclerosis*. 8(1):40-45, 1988.

Paragios N, Chen Y, Faugeras OD. Handbook of mathematical models in computer vision. *Springer*. 2006.

Pasterkamp C and Falk E. Atherosclerotic plaque rupture: an overview. *J Clin Basic Cardiol*. 3(2):81-86, 2000.

Patel DJ and Fry DL. The elastic symmetry of arterial segments in dogs. *Circ Res*. 24(1):1-8, 1969.

Pitt B, Byington RP, Furberg CD, Hunninghake DB, Mancini GB, Miller ME, Riley W. Effect of amlodipine on the progression of atherosclerosis and the occurrence of clinical events. PREVENT Investigators. *Circulation*. 102(13):1503-1510, 2000.

Price JM, Davis DL, Knauss EB. Length-dependent sensitivity in vascular smooth muscle. *Am J Physiol*. 241(4):H557-H563, 1981.

Pynadath TI and Mukherjee DP. Dynamic mechanical properties of atherosclerotic aorta. A correlation between the cholesterol ester content and the viscoelastic properties of atherosclerotic aorta. *Atherosclerosis*. 26(3):311-318, 1977.

Raghavan ML, Vorp DA, Federle MP, Makaroun MS, Webster MW. Wall stress distribution on three-dimensionally reconstructed models of human abdominal aortic aneurysm. *J Vasc Surg*. 31(4):760-769, 2000.

Ray KK, Cannon CP, McCabe CH, Cairns R, Tonkin AM, Sacks FM, Jackson G, Braunwald E. Early and late benefits of high-dose atorvastatin in patients with acute coronary syndromes: results from the PROVE IT-TIMI 22 trial. *J Am Coll Cardiol*. 46(8):1405-1410, 2005.

Roach MR and Burton AC. The reason for the shape of the distensibility curves of arteries. *Can J Biochem Physiol*. 35(8):681-690, 1957.

Russ JC. The image processing handbook. 6th edition. *CRC Press*. 2011.

Schreier HW, Braasch JR, Sutton MA. Systematic errors in digital image correlation caused by intensity interpolation. *Opt Eng*. 39(11):2915-2921, 2000.

Schreier HW and Sutton MA. Systematic errors in digital image correlation due to undermatched subset shape functions. *Exp Mech*. 42(3):303-310, 2002.

Sherebrin MH, Bernans HA, Roach MR. Extensibility changes of calcified soft tissue strips from human aorta. *Can J Physiol Pharmacol*. 65(9):1878-1883, 1987.

Stålhand J, Klarbring A, Holzapfel GA. Smooth muscle contraction: mechanochemical formulation for homogeneous finite strains. *Prog Biophys Mol Biol*. 96(1-3):465-481, 2008.

Sun D. 2010. Optical flow MATLAB functions.
http://cs.brown.edu/people/dqsun/research/software.html, accessed 19 April 2011.

Sun D, Roth S, Black MJ. Secrets of optical flow estimation and their principles. *IEEE Conf Comput Vis Pattern Recognit*. 2432-2439, 2010.

Sutton MA, Ke X, Lessner SM, Goldbach M, Yost M, Zhao F, Schreier HW. Strain field measurements on mouse carotid arteries using microscopic three-dimensional digital image correlation. *J Biomed Mater Res A*. 84(1):178-190, 2008.

Sutton MA, Orteu JJ, Schreier HW. Image correlation for shape, motion and deformation measurements. *Springer*. 2009.

Takamizawa K and Hayashi K. Strain energy density function and uniform strain hypothesis for arterial mechanics. *J Biomech*. 20(1):7-17, 1987.

Teng Z, Tang D, Zheng J, Woodard PK, Hoffman AH. An experimental study on the ultimate strength of the adventitia and media of human atherosclerotic carotid arteries in circumferential and axial directions. *J Biomech*. 42(15):2535-2539, 2009.

van Popele NM, Grobbee DE, Bots ML, Asmar R, Topouchian J, Reneman RS, Hoeks APG, van der Kuip DAM, Hofman A, Witteman JCM. Association between arterial stiffness and atherosclerosis: the Rotterdam Study. *Stroke*. 32(2):454-460, 2001.

Verhulp E, van Rietbergen B, Huiskes R. A three-dimensional digital image correlation technique for strain measurements in microstructures. *J Biomech*. 37(9):1313-1320, 2004.

Vito RP and Hickey J. The mechanical properties of soft tissues–II: the elastic response of arterial segments. *J Biomech*. 13(11):951-957, 1980.

von Maltzahn WW, Besdo D, Wiemer W. Elastic properties of arteries: a nonlinear two-layer cylindrical model. *J Biomech*. 14(6):389-397, 1981.

Wiklund O, Hulthe J, Wikstrand J, Schmidt C, Olofsson SO, Bondjers G. Effect of controlled release/extended release metoprolol on carotid intima-media thickness in patients with hypercholesterolemia: a 3-year randomized study. *Stroke*. 33(2):572-577, 2002.

Wykretowicz A, Gerstenberger P, Guzik P, Milewska A, Krauze T, Adamska K, Rutkowska A, Wysocki H. Arterial stiffness in relation to subclinical atherosclerosis. *Eur J Clin Invest*. 39(1):11-16, 2009.

Yang J, Clark JW Jr, Bryan RM, Robertson C. The myogenic response in isolated rat cerebrovascular arteries: smooth muscle cell model. *Med Eng Phys*. 25(8):691-709, 2003.

Zanchetti A, Bond MG, Hennig M, Neiss A, Mancia G, Dal Palù C, Hansson L, Magnani B, Rahn KH, Reid JL, Rodicio J, Safar M, Eckes L, Rizzini P. Calcium antagonist lacidipine slows down progression of asymptomatic carotid atherosclerosis: principal results of the European Lacidipine Study on Atherosclerosis (ELSA), a randomized, double-blind, long-term trial. *Circulation*. 106(19):2422-2427, 2002.

Zhang D and Arola DD. Applications of digital image correlation to biological tissues. *J Biomed Opt*. 9(4):691-699, 2004.

Zhang D, Eggleton CD, Arola DD. Evaluating the mechanical behavior of arterial tissue using digital image correlation. *Exp Mech*. 42(4):409-416, 2002.

Zulliger MA, Rachev A, Stergiopulos N. A constitutive formulation of arterial mechanics including vascular smooth muscle tone. *Am J Physiol Heart Circ Physiol*. 287(3):H1335-H1343, 2004.

3. Application of Optical Flow Estimation to Arterial Image Analysis

3.1 Introduction

Various optical flow techniques have been suggested (Horn and Schunck 1981, Barron et al. 1994, Black and Anandan 1996, Sun et al. 2010); and the application of these techniques to estimate tissue movements has been well developed, including studies on arterial (Wan et al. 2001, Maurice et al. 2005, Danilouchkine et al. 2008), cardiac (Xu et al. 2010, Po et al. 2011, Yang et al. 2011), skeletal (du Bois d'Aische et al. 2005, Østergaard Noe et al. 2008), and muscle (Zoccolan et al. 2001) biomechanics. While some of these studies involved determination of deformation strains using the optical flow displacements (Wan et al. 2001, Maurice et al. 2005, Danilouchkine et al. 2008, Xu et al. 2010, Yang et al. 2011), detailed validation of the accuracy of the measurements is limited.

Therefore, before using the optical flow technique to analyse the experimental images in the following studies, the accuracy of the technique was accessed by comparing the optical flow and actual strains of finite element (FE) models. The technique was first used in a comparison of the strains of a square model representing a uniaxial tensile test on a square of biological tissue. This approach was then applied to other two models which mimic the tensile ring test of an atherosclerotic artery and inflation test of a normal artery. The studies confirm the capability of the optical flow estimation to obtain biological tissue deformation from experimental studies, as an alternative approach to digital image correlation or other image analysis methods, and provide a detailed methodology for these applications.

3.2 Methods

An overview of the method used to assess the accuracy of the optical flow methodology is given in Figure 3.1. An FE model was first created and loads applied. The nodal coordinates of the deformed structure were used to create a series of images that capture the deformation steps. These images were then analysed using the optical flow technique to obtain spatial displacement fields. The displacement of each pixel was used to determine the deformed coordinate of the pixel and the corresponded strains which were compared to those of the FE model. This analysis was first applied to a square structure and then to structures mimicking an atherosclerotic artery ring undergoing a tensile deformation and a normal artery undergoing an internal pressurisation.

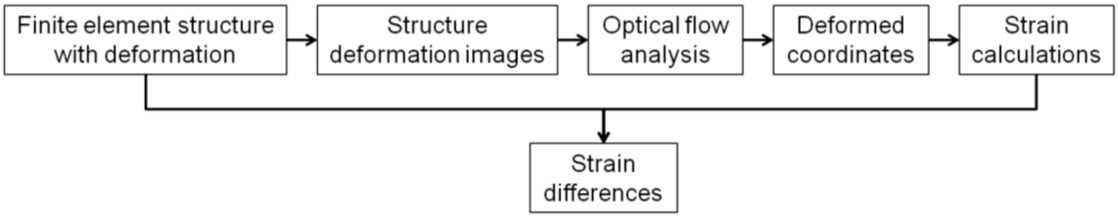

Figure 3.1 Diagram showing the steps of optical flow estimation and strain calculations.

3.2.1 Creation of a finite element structure with deformation

Abaqus FEA software (version 6.9, Dassault Systèmes Simulia, Providence, USA) was used to create a square structure of side-length 1 unit with 500 × 500 elements. A tensile displacement of 0.2 units was applied at both ends of the structure as shown in Figure 3.2. This deformation mimics the condition of a square biological tissue undergoing uniaxial tensile loading. Since only the displacement was required for the analysis, the structure was taken as linear elastic with unit modulus and Poisson’s ratio of 0.5. The loading was split into four steps of 0.05 units each, which enables comparisons of the optical flow analyses between different incremental displacement steps.

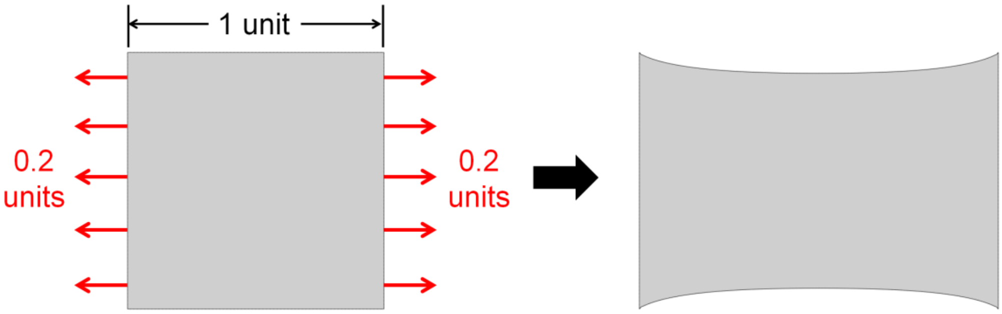

Figure 3.2 Finite element model of a square structure undergoing a tensile deformation.

3.2.2 Creation of images demonstrating the structure deformation

The nodal coordinates of the 500 × 500 square structure elements taken from the initial and deformed geometries after each loading step were used to create a series of corresponded deformed images with MATLAB (version 7.13/R2011b, MathWorks, Natick, USA). A random intensity pattern was assigned to the undeformed structure in the initial image. Assigning the same intensity value to the same element node throughout the deformation steps generates a structure containing the deformed random pattern in each deformation image. In order to create this random pattern, random values with a normal distribution of zero mean and standard deviation equal to 30 were assigned to a matrix of dimensions 1300 × 1300 using the MATLAB *randn* command. The *gridfit* command (D'Errico 2010) was then used to smooth this random pattern and interpolate onto a 520 × 520 grid, using a smoothness parameter equal to 30. Next, the *patch* command was used to create a greyscale image by assigning the intensity of each of the 501 × 501 element nodes with the smoothed matrix value that located at a position corresponded to the coordinates of the particular element node, interpolating as necessary to fill the potential gaps between the nodal coordinates. The value of the smoothness parameter chosen for the *gridfit* function generates approximately 15 to 20 'blob' features across the width of the structure. Using the *patch* command, the intensity associated with each node from the initial configuration were then assigned to the same node in the deformed structure to generate a series of five images corresponding to the initial configuration and the four loading steps, see Figure 3.3. The width of the initial square is approximately 700 pixels.

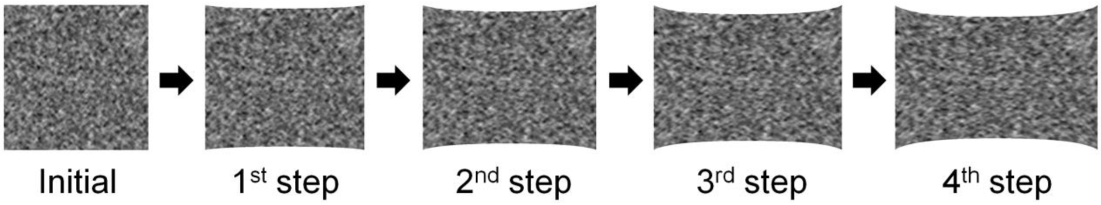

Figure 3.3 Structures created by MATLAB using the initial and deformed coordinates of the finite element nodes.

3.2.3 Analysis of the images using optical flow technique

The deformation of the structure in the images was analysed using the optical flow technique suggested by Sun *et al*. (2010), which has been described in Section 2.4.2.2. The displacement field associated with each loading increment was obtained with the deformed position at each increment used as the initial position for the analysis of the next increment. The deformed coordinates of each node were obtained by adding the incremental displacements to the initial coordinates. In addition to an analysis using all four loading steps, the optical flow analysis was repeated in two steps (i.e. using only the images from the initial, second, and fourth steps) and in only one step (using images from only the initial and final steps), in order to check the capability of the optical flow estimation for detecting larger deformations.

3.2.4 Calculating strains from optical flow results

The strains associated with the deformation were calculated based on standard concepts, see for example in (Abaqus Theory Manual, Section 1.4.1) and the MATLAB function used for stretch calculation in Appendix I. In brief, the images were divided into square elements with width w. For an element undergoing deformation, let the initial position of each corner be $\mathbf{X}$ in $X_1 - X_2$ coordinates, and the final position be $\mathbf{x}$ in $x_1 - x_2$ coordinates (Figure 3.4).

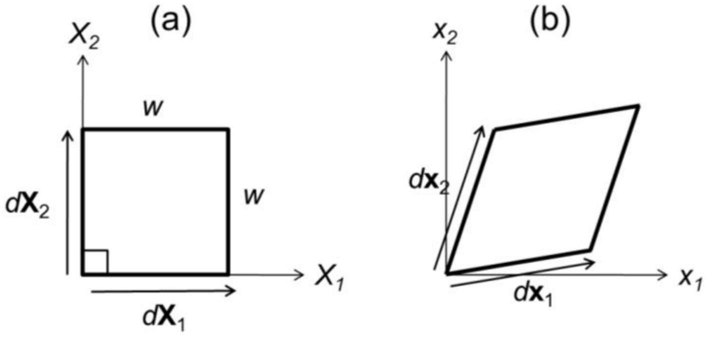

Figure 3.4 (a) Initial and (b) final configurations of a square element undergoing a deformation.

Since there is a one-to-one correspondence between **x** and **X** where **x** = **x**(**X**, *t*), it can be written as:

$$d\mathbf{x} = \frac{\partial \mathbf{x}}{\partial \mathbf{X}} \cdot d\mathbf{X} = \mathbf{F} \cdot d\mathbf{X} \tag{3.1}$$

where **F** is the deformation gradient tensor. Two-dimensional deformation analyses were performed in this study, thus the deformation gradient is:

$$\mathbf{F} = \frac{\partial \mathbf{x}}{\partial \mathbf{X}} = \begin{bmatrix} \frac{\partial x_1}{\partial X_1} & \frac{\partial x_1}{\partial X_2} \\ \frac{\partial x_2}{\partial X_1} & \frac{\partial x_2}{\partial X_2} \end{bmatrix} \tag{3.2}$$

Since the structure underwent uniaxial deformation in the horizontal direction, only the results in the X_1 direction were compared. The horizontal stretch λ_{X1} was obtained from **F** as:

$$\lambda_{X1} = F_{11} = \frac{\partial x_1}{\partial X_1} \tag{3.3}$$

The logarithmic horizontal strain ε_{X1} was then calculated as the natural logarithm of the stretch.

$$\varepsilon_{X1} = \ln \lambda_{X1} \tag{3.4}$$

A two-dimensional mean filter was applied to the strain results using MATLAB *smooth2a* command (Reeves 2009) to reduce noise in the strain data. The strains in the background region of the image were assigned a ‘Not-a-Number’ (*NaN*) representation to avoid using regions outside the structure boundaries in the smoothing procedure. The normalised differences between the smoothed strains and the strains of the FE model were then calculated as:

$$e = \frac{|\varepsilon_{\mathrm{FE}} - \varepsilon_{\mathrm{OF}}|}{\varepsilon_{\mathrm{FE}}} \times 100\% \tag{3.5}$$

where e is the error representing the difference, and $\varepsilon_{\mathrm{FE}}$ and $\varepsilon_{\mathrm{OF}}$ are the strains of the FE model and optical flow analysis, respectively. The mean value of the errors e_m averaged across the elements in the structure was used to determine the overall accuracy of the optical flow strain field.

3.2.5 Determining optimum smoothness parameters

There are four parameters that influence the smoothness of the optical flow strain results, which are the median filter size m_1 and regularisation parameter λ of the optical flow functions (Sun et al. 2010), the grid size w for the strain calculations, and the mean filter size m_2 used for smoothing the strains. Larger values of these parameters produce smoother strain results, reducing any noise in the data but also limiting the spatial resolution of the analysis. In order to determine the optimum set of these parameters that provides the lowest e_m by reducing the outliers but not over-smoothing the results, multi-dimensional analyses were carried out varying these parameters from 3 to 55 pixels.

3.2.6 Analysis with an atherosclerotic artery structure undergoing tensile test

After examining the accuracy of the square structure deformation, the capability of the optical flow analysis was further tested on more sophisticated biomechanical test geometries. The FE model of a circular disc structure with diameter = 1 unit was created (Figure 3.5), mimicking a diseased artery ring with occluded lumen as in the case of atherosclerosis. This structure has two rigid pins embedded in the body which underwent tensile displacement of 0.1 units, representing two hooks used to stretch the artery ring. The size of an element in this structure is approximately 0.002 units. The material properties are the same as those of the square structure, and the displacement was separated into four steps of 0.025 units each.

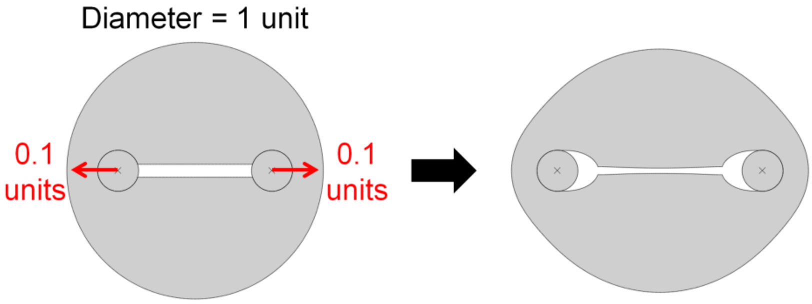

Figure 3.5 Finite element model of an atherosclerotic artery structure undergoing a tensile deformation from two pins.

As with the square structure, images capturing the deformation of the artery structure were constructed with MATLAB (Figure 3.6) and analysed with the optical flow technique. The diameter of the initial structure is approximately 700 pixels. Again, analyses using all four loading steps, two steps, and a single step were performed. The strains in the horizontal direction were then calculated, and the differences between the analysed and FE model strains were determined. In order to prevent over-emphasis on regions with very small strains which occur at the edges of this structure, where the estimate of the error (Equation 3.5) would involve division by a small number, the error calculation included only elements with strains $|\varepsilon| > 0.02$ which accounted for 61% of the total elements. In addition, the smoothness parameters of the optical flow analysis and strain calculation were varied over the same range as for the square structure to find the optimum set of parameters that provided the lowest e_m.

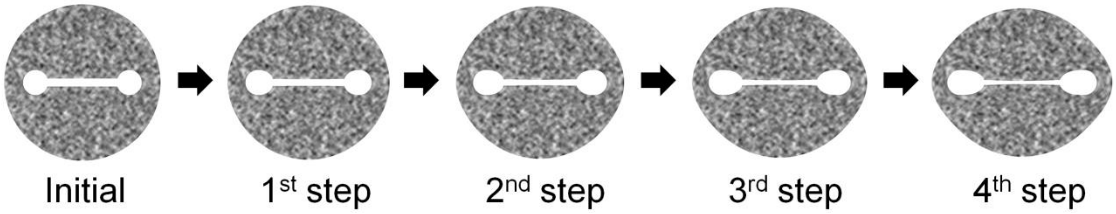

Figure 3.6 Atherosclerotic artery structures created by MATLAB using the initial and deformed coordinates of the finite element nodes.

3.2.7 Analysis with a normal artery structure undergoing inflation test

Following the optical flow analysis of the atherosclerotic artery structure, the application of the technique to a different case of deformation was examined. A circular ring FE model with diameter = 1 unit and wall thickness = 0.1 unit was created (Figure 3.7), mimicking a normal artery ring undergoing an internal pressurisation with inner circumferential strains of 0.09. The inflation was separated into five steps, and images capturing the deformation were constructed with MATLAB (Figure 3.8). The diameter of the initial structure is approximately 860 pixels. Again, optical flow analyses using all five loading steps, three steps, and a single step were performed.

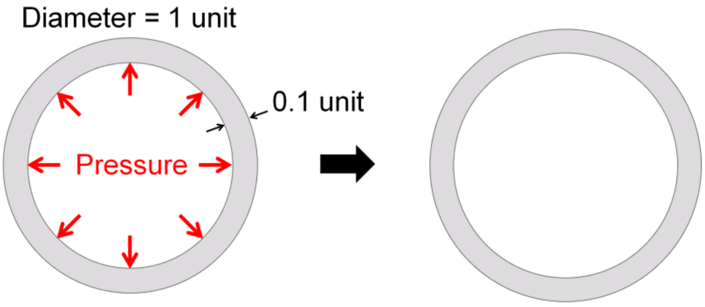

Figure 3.7 Finite element model of a normal artery structure undergoing an internal pressurisation.

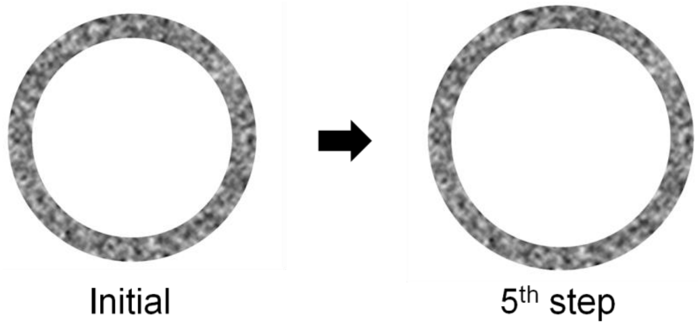

Figure 3.8 Normal artery structures created by MATLAB using the initial and deformed coordinates of the finite element nodes.

The circumferential strains of the structure were then calculated using the theory described in Section 3.2.4, see the MATLAB function used to calculate the strain tensor in Appendix II. From Equation (3.2), the right Cauchy-Green deformation tensor **C** is

$$\mathbf{C} = \mathbf{F}^{\mathrm{T}}\mathbf{F} \tag{3.6}$$

and the Green-Lagrange strain tensor **E** is

$$\mathbf{E} = \frac{1}{2}(\mathbf{C} - \mathbf{I}) \tag{3.7}$$

where **I** is the identity matrix. The horizontal, vertical, and shear strains are the E_{11}, E_{22}, and E_{12} components in the strain tensor, respectively. The circumferential strain ε_c is then calculated using Equation (3.8):

$$\varepsilon_c = E_{11}\sin^2\theta + E_{22}\cos^2\theta - 2E_{12}\sin\theta\cos\theta \tag{3.8}$$

where θ is the counterclosewise angle from the positive horizontal axis. In order to compare to the logarithmic strains of the FE model, ε_c is converted to the stretch λ_c and logarithmic strain ε using Equations (3.9) and (3.10).

$$\lambda_c = \sqrt{2\varepsilon_c + 1} \tag{3.9}$$

$$\varepsilon = \ln\lambda_c \tag{3.10}$$

The differences between the analysed and FE strains were determined using Equation (3.5). The smoothness parameters of the analysis were again varied over the same range as for the previous structures to find the optimum set of parameters that provided the lowest e_m.

3.3 Results

3.3.1 Square structure

The final horizontal logarithmic strains of the square FE model are shown in Figure 3.9, plotted with Abaqus as colour contours on the initial and deformed geometries of the structure. The majority of the strains are in the range of 0.22 to 0.38. Varying the median filter size m_1 and regularisation parameter λ from 3 to 55 pixels, and the strain grid size w and mean filter size m_2 for 3, 5, 15, 25, 35, 45, and 55 pixels, the mean error e_m of each analysis was found (Table 3.1). Based on the trend of the changes of e_m, analyses where a higher value of e_m would be expected were not carried out. Among these analyses, m_1 = 3, λ = 3, w = 35, and m_2 = 35 pixels provides the lowest e_m.

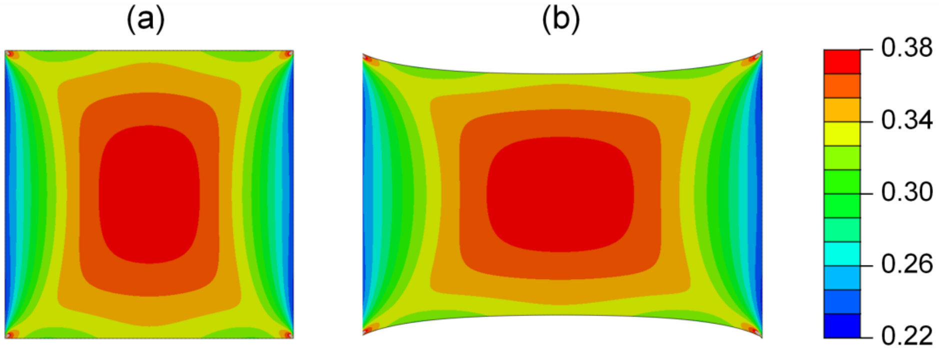

Figure 3.9 The final horizontal logarithmic strains of the square finite element model plotted on the (a) initial and (b) deformed geometries of the structure.

Table 3.1 Effect of changes in smoothing parameters m_1, λ, w, and m_2 on the value of the normalised average strain error e_m (%) for the square structure. The value of e_m given at each point in the table is the lowest value taken from a set of calculations with w and m_2 both spanning the range of {3, 5, 15, 25, 35, 45, 55} pixels. The case of m_1 = 3, λ = 3, w = 35, and m_2 = 35 pixels, given in bold, has the smallest e_m.

λ m_1	3	5	7	15	35	55
3	**0.842**	0.849	0.851	0.857	0.863	0.894
5	0.843	0.849	0.851	-	-	-
7	0.845	0.849	0.851	-	-	-
15	-	0.850	-	0.853	0.862	0.906
35	-	0.854	-	-	-	-
55	-	0.865	-	0.878	0.889	0.985

Further comparison was then made for the ranges of w and m_2 narrowed to 35 ± 8 pixels, with m_1 and λ fixed at 3 pixels. Figure 3.10 shows the e_m of the analyses with w and m_2 over the range of 15 to 55 pixels and m_1 and λ equal to 3 pixels. From this comparison, m_1 = 3, λ = 3, w = 35, and m_2 = 35 pixels is the set of optimum smoothness parameters that provides the lowest e_m.

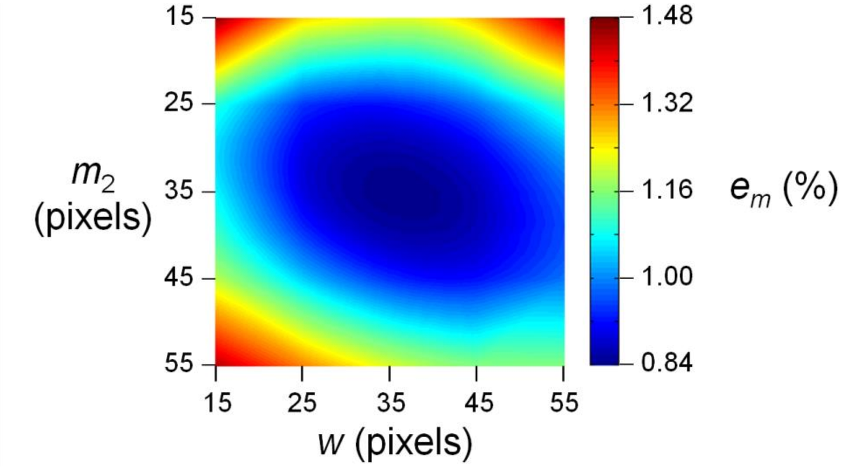

Figure 3.10 The value of e_m for the square structure analyses using w and m_2 ranging from 15 to 55 pixels while fixing m_1 and λ at 3 pixels. The case of both w and m_2 = 35 pixels provides the lowest value of e_m.

The horizontal logarithmic strains of the analysis using the optimum smoothness parameters are presented in Figure 3.11a, along with the FE strains (Figure 3.11b) and the normalised error differences between the strains (Figure 3.11c). In order to observe the strain differences without normalisation, the non-normalised errors $e = |\varepsilon_{\mathrm{FE}} - \varepsilon_{\mathrm{OF}}|$ were further calculated as shown in Figure 3.11d. The value of e_m for this four-step analysis, as well as those for the one and two steps analyses using optimum smoothness parameters are given in Table 3.2.

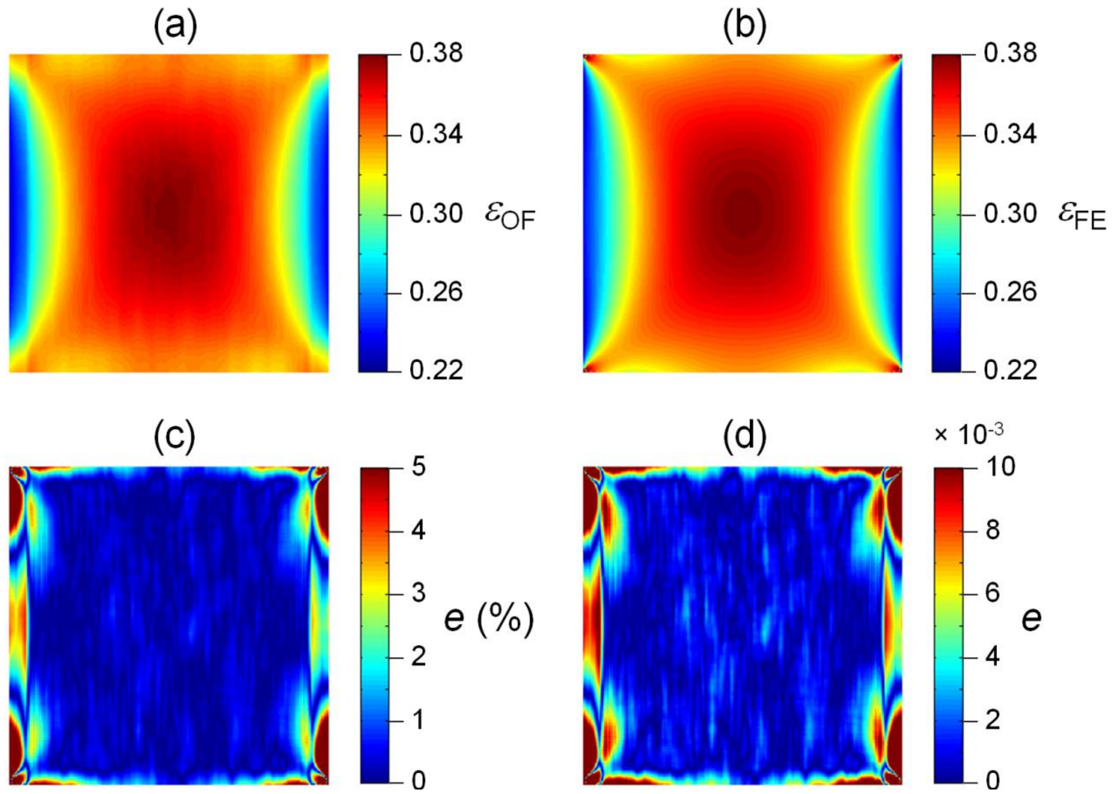

Figure 3.11 The horizontal logarithmic strains of the (a) optical flow and (b) finite element analyses, $\varepsilon_{\mathrm{OF}}$ and $\varepsilon_{\mathrm{FE}}$, of the square structure. (c) Normalised and (d) non-normalised errors *e* between the optical flow and finite element strains.

Table 3.2 The effect of the number of analysis steps on the value of the normalised average strain error e_m for the square structure, using the optimum smoothness parameters.

	Optical flow increment		
	One step	**Two steps**	**Four steps**
e_m (%)	65.2	0.83	0.84

3.3.2 Atherosclerotic artery tensile test structure

The final horizontal logarithmic strains of the atherosclerotic artery FE model are shown in Figure 3.12. The deformation pattern is more complex than for the square model, with the majority of the strains in the range of -0.15 to 0.30.

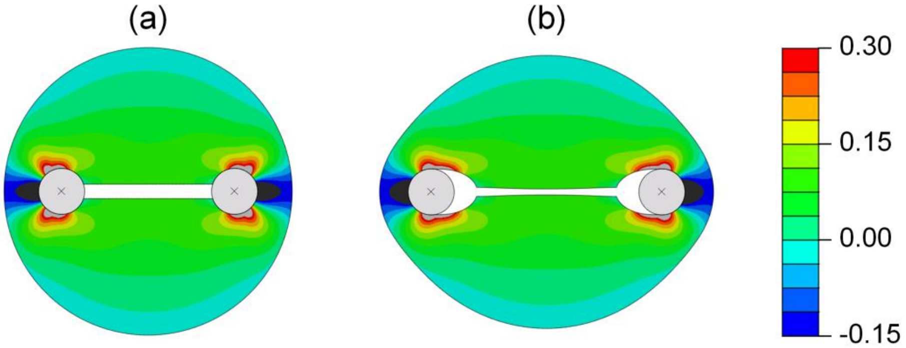

Figure 3.12 The final horizontal logarithmic strains of the atherosclerotic artery model plotted on the (a) initial and (b) deformed geometries of the structure.

Comparing only the strains of $|\varepsilon| > 0.02$ and varying the smoothness parameters in the same way as for the square structure analysis, the set of parameters that minimises the average strain error e_m for this artery analysis is $m_1 = 15$, $\lambda = 5$, $w = 3$, and $m_2 = 29$ pixels. The horizontal logarithmic strains for this analysis are presented in Figure 3.13a. The normalised and non-normalised error differences between the strains inferred from optical flow and those of the FE model (Figure 3.13b) are shown in Figures 3.13c and 3.13d, respectively. The value of e_m for this analysis, which uses four deformation steps, is 13.0%, which is lower than corresponding estimates using one or two steps (Table 3.3).

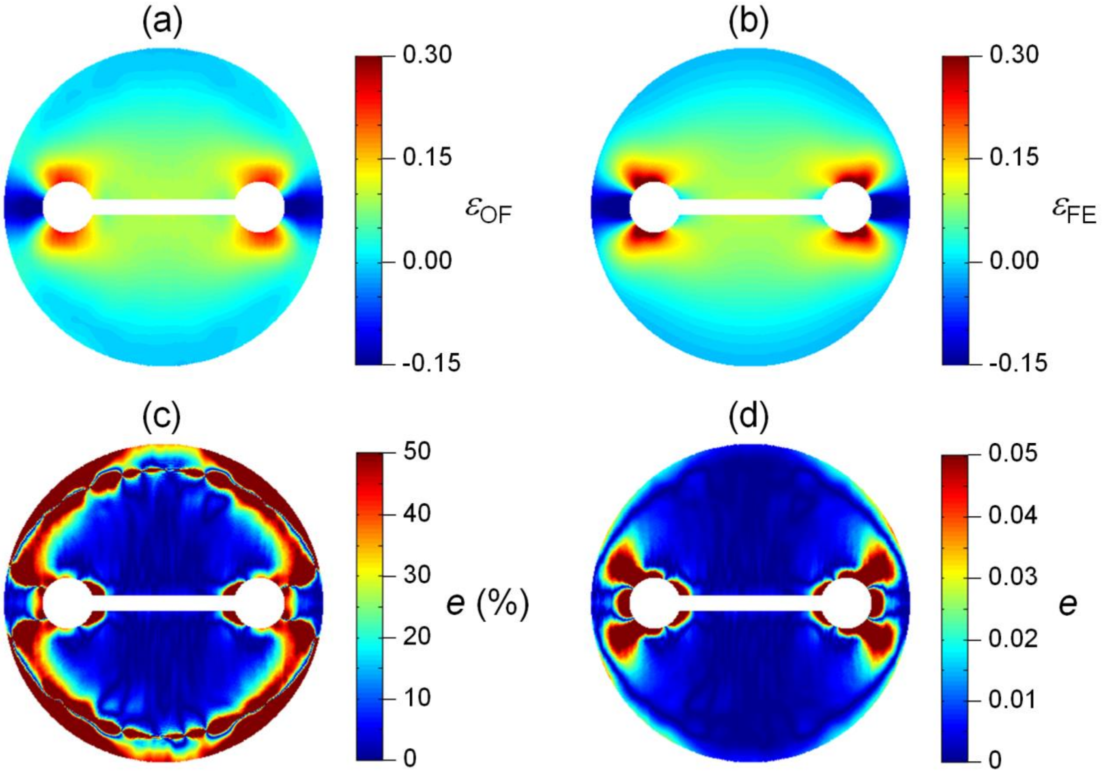

Figure 3.13 The horizontal logarithmic strains of the (a) optical flow and (b) finite element analyses, $\varepsilon_{\mathrm{OF}}$ and $\varepsilon_{\mathrm{FE}}$, of the atherosclerotic artery structure. (c) Normalised and (d) non-normalised errors *e* between the optical flow and finite element strains.

Table 3.3 The effect of the number of analysis steps on the value of the normalised average strain error e_m for $|\varepsilon| > 0.02$ for the atherosclerotic artery structure, using the optimum smoothness parameters.

	Optical flow increment		
	One step	**Two steps**	**Four steps**
e_m (%)	17.9	13.3	13.0

In a real experiment, it is proposed to use only the central region of the atherosclerotic artery ring to extract strains and hence values for material properties, avoiding regions with potentially large errors around the loading points. Therefore, a further analysis was performed to determine the optimum smoothness parameters of this case where only the errors of these central regions were calculated, see Figure 3.14. In this case the set of optimum smoothness parameters is $m_1 = 3$, $\lambda = 3$, $w = 63$, and $m_2 = 37$ pixels, with $e_m = 2.91\%$.

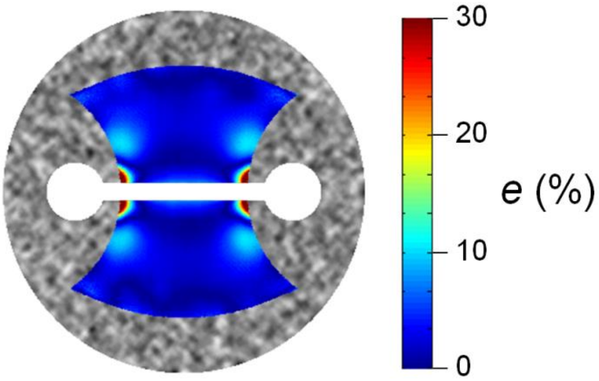

Figure 3.14 Normalised errors e over the central region of the atherosclerotic artery structure. The analysis was performed using the optimum smoothness parameters determined by comparing only the strains of these regions with those of the finite element model.

3.3.3 Normal artery inflation test structure

The circumferential logarithmic strains of the normal artery FE model subject to inflation, calculated using the horizontal, vertical, and shear strains with Equation (3.8), are in the range of 0.065 to 0.09 (Figure 3.15a). The set of smoothness parameters that minimises the average strain error e_m for the optical flow analysis is $m_1 = 3$, $\lambda = 7$, $w = 11$, and $m_2 = 23$ pixels. The circumferential logarithmic strains for this analysis are presented in Figure 3.15b, whereas the normalised and non-normalised error differences between the optical flow and FE strains are shown in Figures 3.15c and 3.15d, respectively. Table 3.4 shows the value of e_m for this analysis which uses five deformation steps, along with the corresponding estimates using one or three steps.

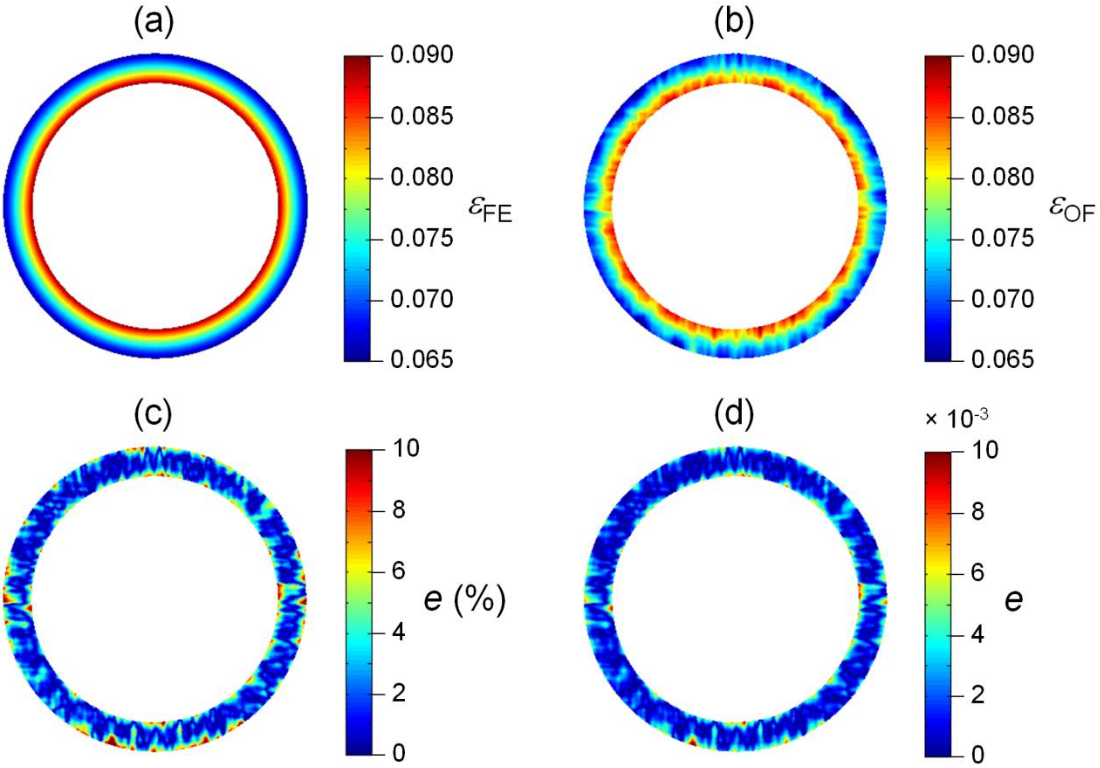

Figure 3.15 The circumferential logarithmic strains of the (a) finite element and (b) optical flow analyses, $\varepsilon_{\mathrm{FE}}$ and $\varepsilon_{\mathrm{OF}}$, of the normal artery structure. (c) Normalised and (d) non-normalised errors *e* between the optical flow and finite element strains.

Table 3.4 The effect of the number of analysis steps on the value of the normalised average strain error e_m for the normal artery structure, using the optimum smoothness parameters.

	Optical flow increment		
	One step	**Three steps**	**Five steps**
$\boldsymbol{e_m}$ **(%)**	1.82	2.16	2.26

3.4 Discussion

The results show good estimates of the strains of the square structure and inflated artery analyses, with $e_m < 2\%$ for the differences between the optical flow and FE results. However, the atherosclerotic artery tensile test analysis provides lower accuracy with $e_m = 13\%$. This may due to the more complex deformation of the atherosclerotic artery structure, which contains both tensile and compressive deformations of the elements. In addition, the low strain regions in the structure (Figures 3.13a and 3.13b) may also contribute to this higher error, where the optical flow estimation failed to track the near zero deformation thus causing high normalised errors. This can be verified by comparing the normalised and non-normalised error plots of the analyses. The colour distributions are not significantly different between the normalised and non-normalised error plots for both the square structure (Figures 3.11c and 3.11d) and inflated artery (Figures 3.15c and 3.15d); whereas those of the atherosclerotic artery error plots (Figures 3.13c and 3.13d) are different due to the existence of low strains at the edges which result in high normalised errors. While considering $e_m = 13\%$ to be acceptable accuracy, these high error regions can be avoided in a real experiment by just taking into account the central regions of the artery ring which have low errors. These regions are the essential part of the analysis of the diseased artery properties, which are mainly composed of atherosclerotic plaque. As shown in Figure 3.14, these central regions have a low value of $e_m = 2.9\%$ which strengthens the confidence with which optical flow analysis can be applied to the uniaxial tensile test of atherosclerotic artery ring.

The comparisons between the results of the optical flow analyses with different loading steps show that separated optical flow estimation is required for large tissue deformation. Having a relatively large deformation, the one step analysis of the square structure provides a high $e_m = 65\%$ which shows failure in tracking the displacements. In contrast, the optical flow analyses with smaller deformation steps in both two and four steps analyses provide significantly better estimates with $e_m = 0.8\%$ for both cases. On the other hand, the one step analysis of the atherosclerotic artery tensile test and normal artery inflation test structures show less significantly different e_m than the multi-step analyses. This may due to the smaller deformations of the artery structures where the displacements were better tracked in the one step analysis. The slightly lower e_m of the one step analysis of the inflation test structure compared to its three and five steps analyses indicates that unnecessary analysis steps may lead to higher errors accumulated from each step. These results show that the optimum number of analysis step depends on the tissue deformation, where a small deformation may requires fewer steps than a large deformation.

The optimum set of smoothness parameters differs between the analyses of three structures, with the best choice dependent on the particular deformation case rather than being a global parameter set suitable for all deformation analyses. When considering only the errors in the central regions of the atherosclerotic artery structure, the optimum values of m_1, λ, and m_2 are similar to those of the square analysis, suggesting that the observed differences in the optimum parameters between these two cases are mainly due to the difference in the geometry. This analysis of the central regions of atherosclerotic artery also did not involve over-smoothing across structure boundaries, leading to a significantly higher optimum w. On the other hand, the lower optimum w and m_2 of the inflated normal artery may be due to its thin-wall structure, where these lower w and m_2 prevent over-smoothing of the strains across boundaries. Despite these differences in the optimum smoothness parameters, the analyses tend to be less sensitive to m_1 and λ but more sensitive to w and m_2. This can be observed from the smaller variations of error values in Table 3.1 than those in Figure 3.10 for the square structure analysis. Overall, the optimum parameters vary with deformation pattern, structural geometry, or image resolution. Therefore, it is recommended that the validation approach for a given optical flow analysis should be carried out by generating an FE structure with a deformation that mimics the condition of the real experiment.

Some studies in the mechanical properties of artery (Wan et al. 2001, Maurice et al. 2005, Danilouchkine et al. 2008) and heart (Xu et al. 2010, Yang et al. 2011) involved determination of tissue deformation strains using optical flow analysis. While these studies provided reasonable estimates of the tissue deformations, a separate validation of the performance of the optical flow technique in these cases has not been carried out. This leads to an uncertain accuracy of the deformation results. In this study the performance of the optical flow technique developed by Sun *et al.* (2010) in various biomechanics applications was examined, which demonstrates the capability of using the technique in these experiments.

3.5 Conclusion

This chapter demonstrates the capability of the optical flow technique to track the deformation of biological tissue in a biomechanical experiment. Using FE models representing tensile tests of square tissue and atherosclerotic artery and an inflation test of normal artery, the optical flow analyses of the constructed deformation images were shown to provide good estimates of the strains for all of these deformation cases. The influences of the smoothness parameters and the number of analysis steps on the accuracy of the technique were also determined. Overall, this validation of the optical flow estimation technique shows that it can be an alternative approach to digital image correlation or other image analysis methods for the following experimental studies. The techniques and smoothing parameters determined in this chapter are used in the studies in Chapters 4 and 7 to find the cross-sectional mechanical properties of atherosclerotic plaques and a healthy artery, respectively, where the optical flow estimation has provided more sensible results than the attempted digital image correlation techniques.

3.6 References

Abaqus Theory Manual, Section 1.4.1. *Abaqus 6.9 Documentation Collection*. Dassault Systèmes Simulia, Providence, USA.

Barron JL, Fleet DJ, Beauchemin SS. Performance of optical-flow techniques. *Int J Comput Vision*. 12(1):43-77, 1994.

Black MJ and Anandan P. The robust estimation of multiple motions: parametric and piecewise-smooth flow fields. *Comput Vision Image Understanding*. 63(1):75-104, 1996.

Danilouchkine MG, Mastik F, van der Steen AFW. Improving IVUS palpography by incorporation of motion compensation based on block matching and optical flow. *IEEE Trans Ultrason Ferroelectr Freq Control*. 55(11):2392-2404, 2008.

D'Errico J. 2010. Surface fitting using gridfit. http://www.mathworks.de/matlabcentral/fileexchange/8998, accessed 14 October 2011.

du Bois d'Aische A, De Craene M, Macq B, Warfield SK. An improved articulated registration method for neck images. *Conf Proc IEEE Eng Med Biol Soc*. 7:7668-7671, 2005.

Horn BKP and Schunck BG. Determining optical-flow. *Artif Intell*. 17(1-3):185-203, 1981.

Maurice RL, Daronat M, Ohayon J, Stoyanova E, Foster FS, Cloutier G. Non-invasive high-frequency vascular ultrasound elastography. *Phys Med Biol*. 50(7):1611-1628, 2005.

Østergaard Noe K, De Senneville BD, Elstrøm UV, Tanderup K, Sørensen TS. Acceleration and validation of optical flow based deformable registration for image-guided radiotherapy. *Acta Oncol*. 47(7):1286-1293, 2008.

Po MJ, Lorsakul A, Laine AF. A momentum-based constraint on optical flow tracking of the endocardial surface. *Conf Proc IEEE Eng Med Biol Soc*. 7191-7194, 2011.

Reeves G. 2009. Smooth2a. http://www.mathworks.co.uk/matlabcentral/fileexchange/23287, accessed 30 March 2012.

Sun D, Roth S, Black MJ. Secrets of optical flow estimation and their principles. *IEEE Conf Comput Vis Pattern Recognit*. 2432-2439, 2010.

Wan M, Li Y, Li J, Cui Y, Zhou X. Strain imaging and elasticity reconstruction of arteries based on intravascular ultrasound video images. *IEEE Trans Biomed Eng*. 48(1):116-120, 2001.

Xu C, Pilla JJ, Isaac G, Gorman JH, Blom AS, Gorman RC, Ling Z, Dougherty L. Deformation analysis of 3D tagged cardiac images using an optical flow method. *J Cardiovasc Magn Reson*. 12:19, 2010.

Yang L, Georgescu B, Zheng Y, Wang Y, Meer P, Comaniciu D. Prediction based collaborative trackers (PCT): a robust and accurate approach toward 3D medical object tracking. *IEEE Trans Med Imaging*. 30(11):1921-1932, 2011.

Zoccolan D, Giachetti A, Torre V. The use of optical flow to characterize muscle contraction. *J Neurosci Methods*. 110(1-2):65-80, 2001.

4. Determination of the Heterogeneous Mechanical Properties of Atherosclerotic Artery

4.1 Introduction

The rupture of atherosclerotic plaque causes morbidity and mortality, where the risk of the rupture is closely related to the plaque material properties and external mechanical factors (Falk et al. 1995, Pasterkamp and Falk 2000). Studies have been carried out to measure the mechanical properties of atherosclerotic arteries using various techniques (Akyildiz et al. 2014). Beattie *et al.* (1998) used an experimental-computational method involving *in vitro* inflation test on artery rings and finite element (FE) modelling to investigate the mechanical behaviour of atherosclerotic human aorta. In recent years, the research group of Baldewsing *et al.* (2004a, 2004b, 2005, 2006, 2008) has performed in-depth investigations using intravascular ultrasound (IVUS) elastography to obtain the strain fields of human atherosclerotic arteries with *in vitro* and *in vivo* conditions, as well as that of an artificial artery; they then applied FE modelling and an inverse method to find the Young's moduli of separated regions in the plaque. In addition, Le Floc'h *et al.* (2009, 2010) suggested another inverse FE reconstruction approach aiming to reduce the geometry parameters and track calcium inclusions in the plaque, adding to the capabilities of Baldewsing's models.

While these studies provided essential contributions to the development of tracing the risk of plaque rupture, they dealt with the heterogeneous material properties of the plaque by separating it into several regions with different Young's modulus. This limits the ability of their models to detect the potential highly variable heterogeneous properties of the plaque. Moreover, the material nonlinearity of the artery was neglected as the range of the tested strains was small.

In this chapter, a novel approach combining experimental testing, FE modelling, and image analysis was developed to obtain the cross-sectional mechanical properties of excised atherosclerotic artery rings. In contrast to the techniques in the above mentioned studies, hyperelastic functions were assigned to obtain a heterogeneous shear modulus field for the tested artery. This whole-section analysis provides a better assessment of the critical regions of the arterial wall. From a clinical perspective, this *in vitro* estimation of the arterial properties can be used to compare with those of *in vivo* studies. This approach can also be applied to other experiments, such as the use of animal models and the investigation of the effects of pharmacological drugs on atherosclerotic artery.

4.2 Methods

As an overview, uniaxial tensile tests were first performed on artery rings harvested from human healthy and atherosclerotic coronary arteries. The images of the ring deformations and arterial reaction forces were recorded. FE models were then developed using Abaqus (version 6.9, Dassault Systèmes Simulia, Providence, USA), mimicking the geometries and loading conditions of the artery rings. The images of the atherosclerotic artery tests were analysed using optical flow estimation which enables determination of the local strains on the rings. The force results of the healthy artery model were matched with those of the experiment to obtain the material properties of the healthy arterial wall. These properties were then assigned to the arterial wall region of the atherosclerotic artery model, and the material properties of each element in the plaque region were obtained using an error minimisation approach. In order to do that, the strain and force results of the experiment and the model were matched using MATLAB (version 7.13/R2011b, MathWorks, Natick, USA), where the material parameters of the model were continuously adjusted until the differences were minimised. Details of these methodologies are described in the following sections.

4.2.1 Mechanical testing

The mechanical tests on human arteries were performed by Dr. Sutcliffe with assistance from Dr. Maguire. Having informed consent and ethical approval, healthy and atherosclerotic coronary arteries (n = 3 for each group) were collected from patients undergoing heart transplantation. An arterial ring of 4 mm thickness along the axis of the artery was harvested from each artery with a razor blade mounted in a 'guillotine-style' jig, with the jig arrangement ensuring that the cross-section was flat and perpendicular to the axial direction. The artery ring was mounted onto stainless-steel wire probes connected to a linear stage motor system (MFA-CC and SMC100CC, Newport Corporation, Irvine, USA) for applying tensile loads (Figure 4.1). The size and geometry of the plaque were different between each sample, and the wire probes were positioned at the wider sides of the lumen to minimise slipping of the ring. The surface of the artery ring was sprinkled with silicon carbide particles in some cases to help improve the image analysis. The ring was then immersed in water in a petri dish. Several uniaxial displacement cycles with amplitudes ranging from 0.4 to 1.0 mm for different samples (see Figures 4.6 and 4.7) were applied at a rate of 0.05 mm/s until there was no change in load response. The first few cycles were used for preconditioning; the last cycle was used for the data analysis. Videos were taken during the displacements using a camera connected to a stereo microscope, at a frame rate of 2 fps. Figures 4.2a and 4.2b show the images of the undeformed state of a healthy and atherosclerotic artery, respectively. The reaction forces were recorded with a sampling rate of 10 Hz using a strain-gauged load cell connected to a data logger (National Instruments, Austin, USA).

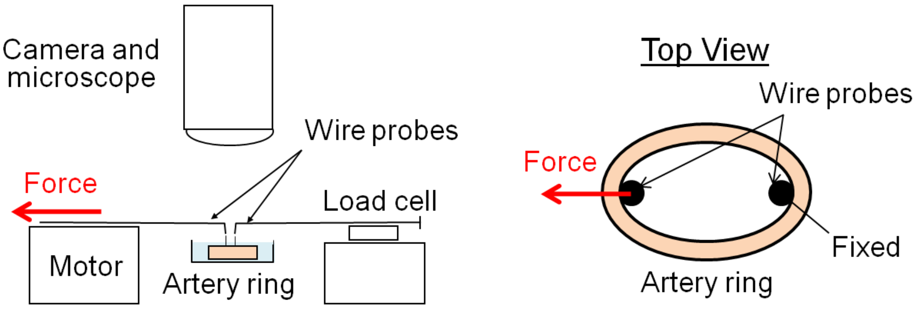

Figure 4.1 The setup of uniaxial tensile artery ring test.

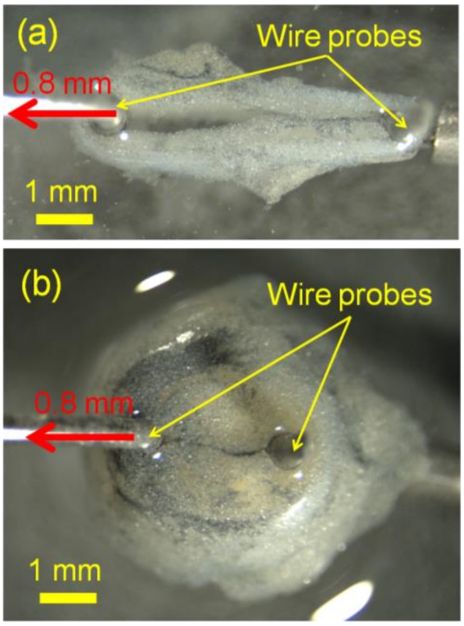

Figure 4.2 Images taken during the mechanical tests before the deformation of (a) a healthy and (b) an atherosclerotic artery ring.

4.2.2 Finite element modelling

Two-dimensional FE models of the healthy and atherosclerotic arteries were created using Abaqus, mimicking the geometries and loading conditions of the artery rings, with the connective tissues surrounding the arterial walls excluded (Figure 4.3). For the healthy artery model (Figure 4.3a), the material was assigned with first-order Ogden hyperelastic properties with the strain-energy function below (Abaqus Theory Manual, Section 4.6.1):

$$U = \frac{2\mu}{\alpha^2}\left({\lambda_1}^{\alpha} + {\lambda_2}^{\alpha} + {\lambda_3}^{\alpha} - 3\right) + \frac{1}{D}(J-1)^2 \tag{4.1}$$

where material parameters μ and α are the shear modulus and hardening exponent, respectively; λ_1, λ_2, and λ_3 are the principal stretches; J is the volume strain; and D is a parameter that determines the material compressibility, which inversely correlated to the bulk modulus K where $K = 2/D$ and $D = 0$ for fully volumetric incompressible material. Assuming nearly incompressible material, D was fixed at 1×10^{-8} $\mathrm{m^2/N}$ which provides an arterial bulk modulus that closed to the value of 4×10^{8} Pa reported by Carew *et al.* (1968) who justified the arterial incompressibility assumption by showing a high ratio of bulk to shear modulus. The Ogden model was chosen rather than a polynomial model in order to capture the potentially rapid strain hardening response with two material parameters in the incompressible case, one representing the arterial modulus and the other representing the hardening effect. The arterial wall was meshed with quadrilateral plane stress elements with an average side width of 0.1 mm. The two wire probes were modelled as rigid bodies with reference points at their centres used to apply loads or record reaction forces. The same tensile displacement as in the experiment was then applied on the left wire probe in the horizontal direction with the right wire probe fixed at the original position (Figure 4.3). The reaction forces of the model on the right wire probe were matched to the experimental recorded forces using MATLAB *fminsearch* function to find the optimum μ and α that minimise the mean error differences e_m between the forces of the experiment f_{exp} and FE model f_{FE}. The error e_m was calculated using Equation (4.2), where $m = 4$ is the number of loading steps.

$$e_m = \frac{\sqrt{\sum_m \left(f_{\text{exp}} - f_{\text{FE}}\right)^2}}{m} \tag{4.2}$$

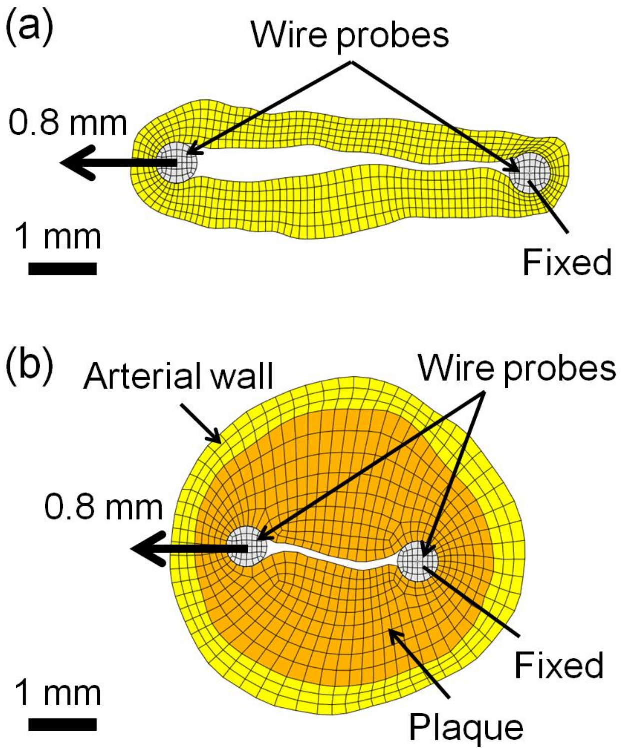

Figure 4.3 Finite element models of the (a) healthy and (b) atherosclerotic artery rings shown in Figure 4.2.

The model of the atherosclerotic artery was separated into the outer healthy wall and inner plaque regions as shown in Figure 4.3b, discriminated visually from the experimental image with referring to the histology section. The model was meshed with quadrilateral plane stress elements with an average side width of 0.2 mm. The rigid body wire probes were used to apply tensile loads or record reaction forces. The healthy wall region of the atherosclerotic artery model was modelled with the Ogden hyperelastic parameters μ, α, and D of the healthy artery model. For the plaque region, each of the elements was fitted with Ogden hyperelastic properties with a different μ parameter. The α and D parameters were assumed to be the same for all of these elements. The optimum μ and α for these elements was found by matching their strains and the reaction forces on the right wire probe with the experiment results. As with the healthy artery model, D was fixed at 1×10^{-8} m^2/N.

4.2.3 Image analysis

In order to determine the strain field of the atherosclerotic arteries, the recorded images from the tests were analysed using the optical flow estimation technique suggested by Sun *et al*. (2010), as described and validated in Chapter 3. Four smoothing parameters have been used to reduce the outliers of the analysis: the median filter size m_1 and regularisation parameter λ of the optical flow functions (Sun et al., 2010), the grid size w for strain calculation, and the mean filter size m_2 for strain smoothing. The optimum smoothness parameters $m_1 = 3$, $\lambda = 3$, $w = 63$, and $m_2 = 37$ pixels for artery ring test analysis, determined in Chapter 3, were applied in this optical flow estimation. The non-vessel regions of the image, i.e. the regions surrounding the vessel, wire probes, and arterial lumen, were masked before running the analysis. This reduced the influence of the movements of non-vessel materials on the arterial deformation analysis. Incremental displacement fields were obtained between four loading steps, and the strains across the entire regions of the artery ring were calculated as in Chapter 3. A mean filter was applied to the strain results to reduce noise in the data.

4.2.4 Optimisation of plaque material parameters

In order to obtain optimum material parameters for the plaque region of the FE model, MATLAB was used to find the parameters that minimised the differences of the strain and force results between the experiment and the model. As shown in Figure 4.4, the analysis was started with a set of reasonable material parameters, modifying the Abaqus input file with these parameters, running the Abaqus analysis, extracting the results from the Abaqus data file, and calculating the error differences between the experiment and FE results. Using the *lsqnonlin* function, the material parameters μ and α of each element in the model were adjusted until the sum of squares of the element strains and reaction forces errors was minimised. This method is believed to give a global rather than a local optimum of the material parameters as the iteration was started with a physiologically-realistic guess.

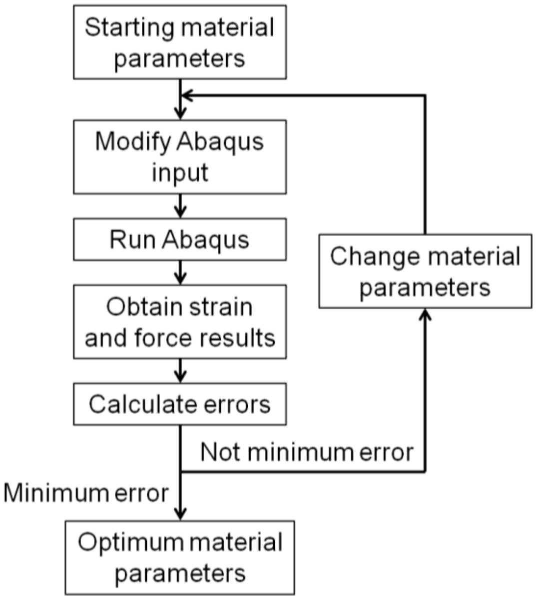

Figure 4.4 Flow diagram showing the steps of material parameter optimisation.

4.2.4.1 Using MATLAB to run material optimisation

In each MATLAB iteration, the Abaqus input file was opened and the material parameters were changed to the desired values. The Abaqus programme was then run with the MATLAB *dos* command. To extract the strain and force results of the model, the Abaqus data file was opened and searched for the results values. Using the *lsqnonlin* function, the material parameters μ and α of each element in the model were adjusted until the sum of squares of the element strains and reaction forces errors, i.e. the differences between the model and experiment results, was minimised.

4.2.4.2 Error calculation

The strain error e_ε for each element at each loading step was calculated as the difference between the horizontal logarithmic strains of the experiment ε_{exp} and FE model ε_{FE}, divided by a specific strain value $\varepsilon_{\text{norm}}$ for normalisation. The $\varepsilon_{\text{norm}}$ is either the absolute value of ε_{exp} or the mean of the absolute ε_{exp} of all elements, whichever is larger. This prevents normalisation by a very small number and over-emphasis on the small strain regions.

$$e_\varepsilon = \frac{\varepsilon_{\text{exp}} - \varepsilon_{\text{FE}}}{\varepsilon_{\text{norm}}} \tag{4.3}$$

$$\varepsilon_{\text{norm}} = \left|\varepsilon_{\text{exp}}\right| \quad \text{or} \quad \frac{\sum_n \left|\varepsilon_{\text{exp}}\right|}{n} \quad \text{whichever is larger} \tag{4.4}$$

n is the number of elements that are involved in the analysis. The force error e_f is the difference between the reaction forces of the experiment f_{exp} and FE model f_{FE}, normalised by f_{exp}.

$$e_f = \frac{f_{\text{exp}} - f_{\text{FE}}}{f_{\text{exp}}} \tag{4.5}$$

The minimisation of errors was performed by comparing the total error e_{total} of each iteration, which was determined as the root mean square of e_ε and e_f, combining the results in all four loading steps $m = 4$. A weighting factor $w_f = 20$ was applied to e_f to emphasise the force matching requirement.

$$e_{\text{total}} = \sqrt{\frac{\sum_n \sum_m {e_\varepsilon}^2 + w_f \sum_m {e_f}^2}{mn + m}} \tag{4.6}$$

4.2.4.3 Assigning material parameters

The optimisation of the choice of material parameters was first run by assigning the parameters to a 7 × 7 grid across the model (blue and magenta asterisks in Figure 4.5a). The blue asterisks mark the active points across the plaque where material parameters were assigned. The material parameters of each plaque element were linearly interpolated from the values at these active grid points. The magenta asterisks around the outside of the plaque are redundant points which were not assigned material parameters. Only the elements labelled with green asterisks were used in strain matching; these elements represent the plaque region excluding the elements surrounding the wire probes. This element selection avoided the large strain errors in the neighbourhood of the probe where the strain distribution is sensitive to the loading. The red asterisks indicate the elements which were not used for the strain matching.

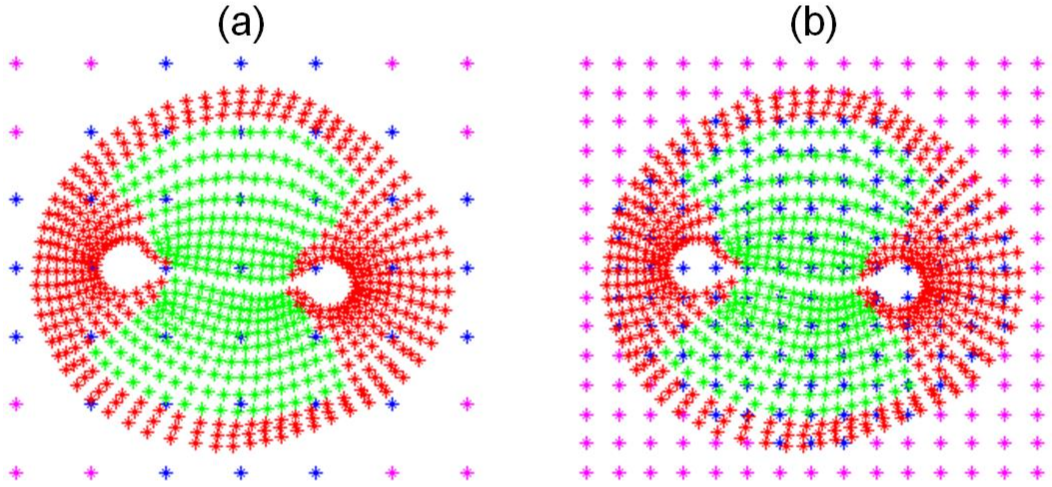

Figure 4.5 Asterisks showing the model of the atherosclerotic artery in Figure 4.2b and the (a) 7 × 7 and (b) 15 × 15 material grids. The green and red asterisks indicate the elements in the finite element model that were and were not used in strain comparisons, respectively. The blue asterisks are the active points of the material grid, which have μ parameters assigned; the magenta asterisks are the redundant material grid points.

Appropriate starting parameters with both μ and α the same for all elements were determined by manually matching the reaction forces until the mean of e_f over the four loading steps was less than 10%. During the optimisation iterations, the value of μ of each material grid point was varied independently, while α was assumed to be uniform across the plaque region. An additional parameter was used to scale all the values of μ to help with convergence. The results of the 7 × 7 grid iterations were used as the starting parameters for a refined 15 × 15 material grid (Figure 4.5b). A similar approach was then applied, and the optimum material properties were obtained from the final results of this refined grid analysis.

4.2.4.4 Checking the optimum material properties

The robustness of the material properties of the plaques found from the optimisation algorithm were checked by comparing the final e_{total} with those found after adjusting the μ of all plaque elements by ±10% or the α of plaque by ±5%. In addition, sections of atherosclerotic arteries adjacent to the tested rings were prepared by Dr. Sutcliffe using a microtome. The images of the section slides were captured under a microscope, and the arterial regions were correlated to the material property results of the corresponding samples.

4.3 Results

The images recorded during the mechanical tests are presented in Figures 4.6 and 4.7, showing the initial and deformed states of the healthy and atherosclerotic artery samples, respectively. In these images, 100 pixels correspond to 0.85 mm. The FE models of these healthy and atherosclerotic arteries are shown in Figures 4.8 and 4.9, respectively.

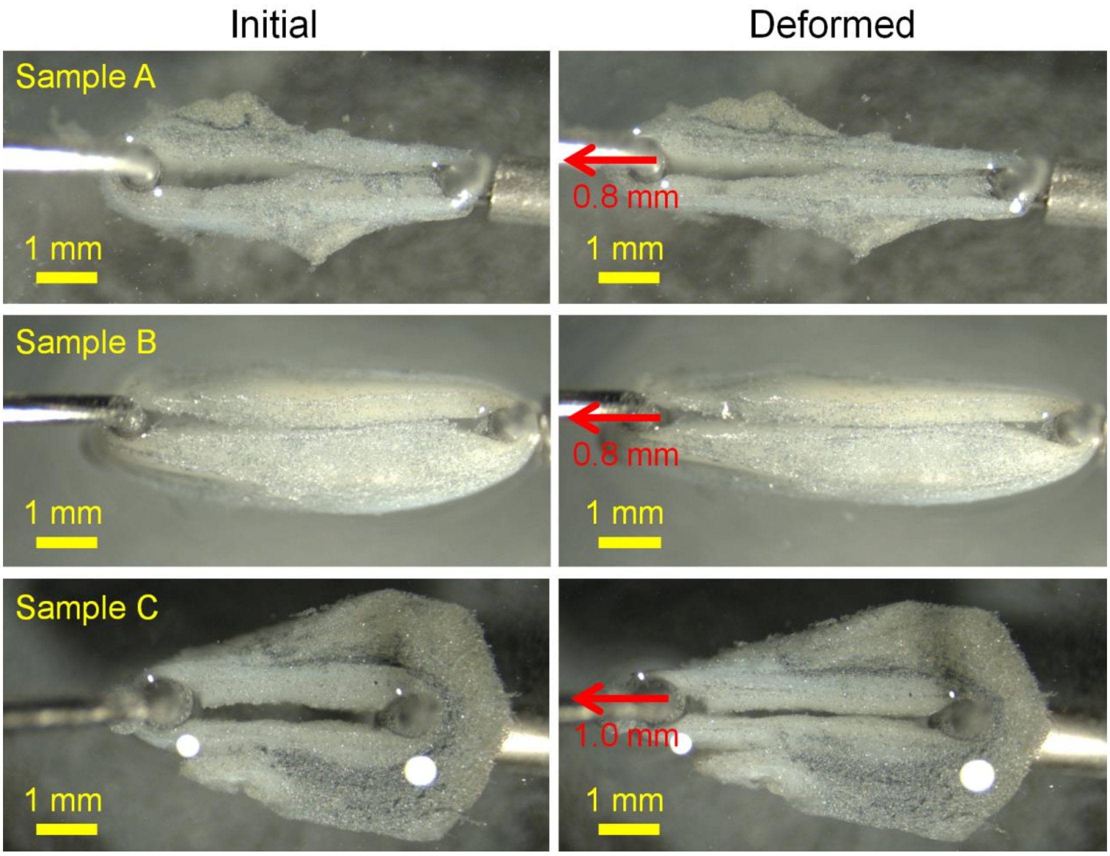

Figure 4.6 Images of the three healthy artery ring tests, showing the initial and deformed geometries. The red arrows show the displacements of the metal probe.

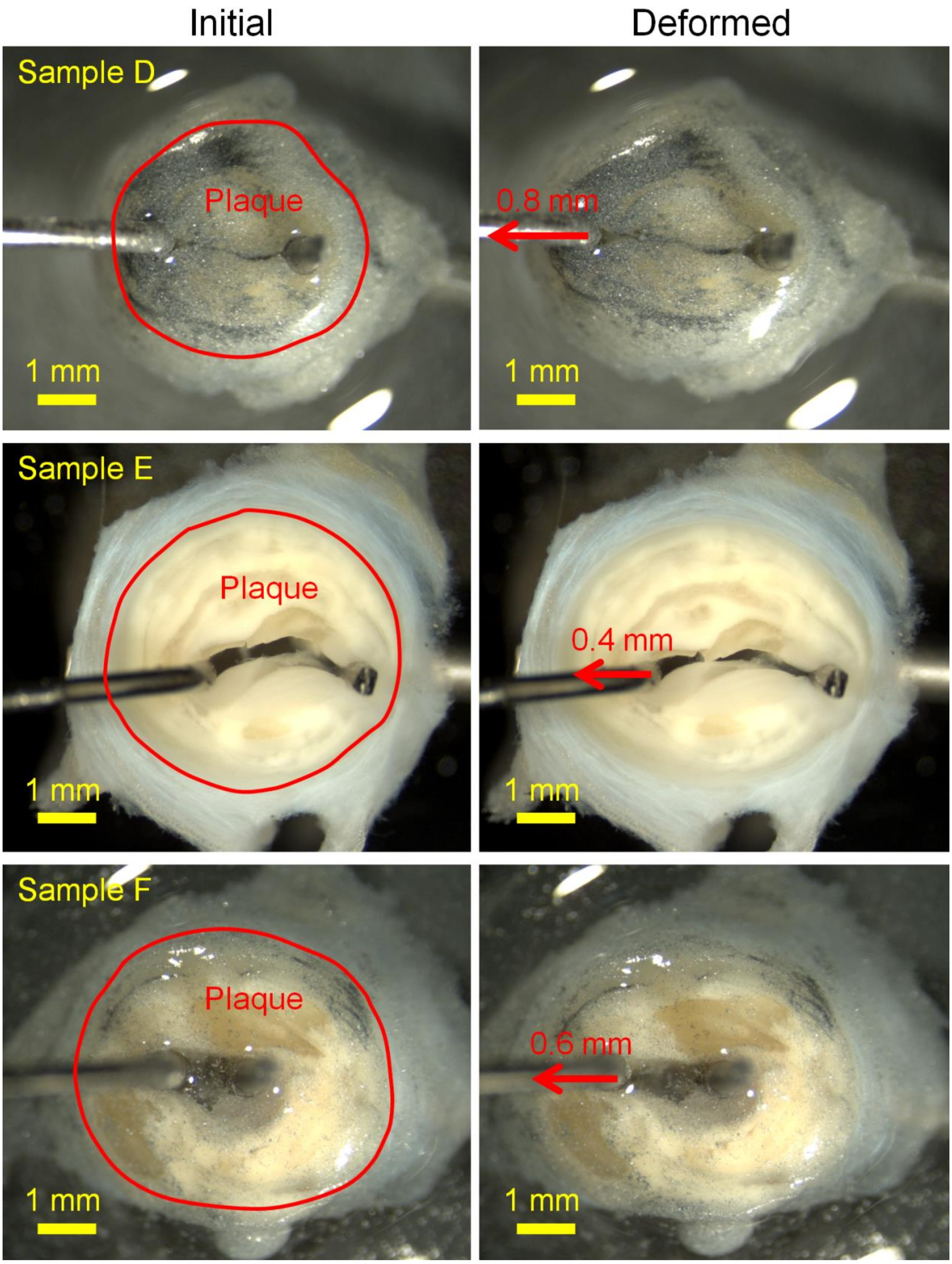

Figure 4.7 Images of the three atherosclerotic artery ring tests, showing the initial and deformed geometries. The plaque regions were highlighted with red, discriminated visually with referring to the histology sections. Silicon carbide particles were placed on Sample D to enhance the deformation analysis.

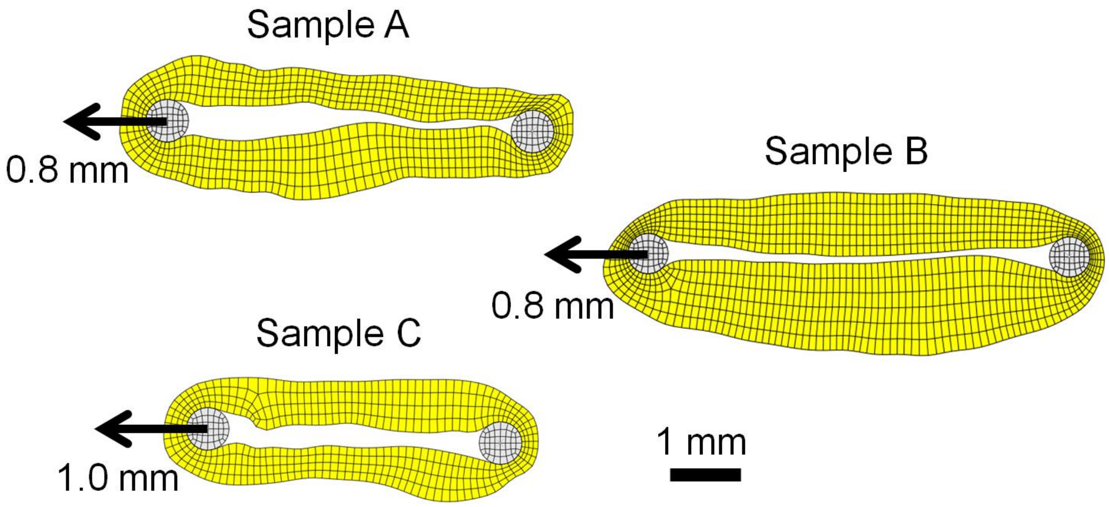

Figure 4.8 Finite element models of the healthy artery samples, mimicking the geometries and loading conditions of the experiments (see Figure 4.6).

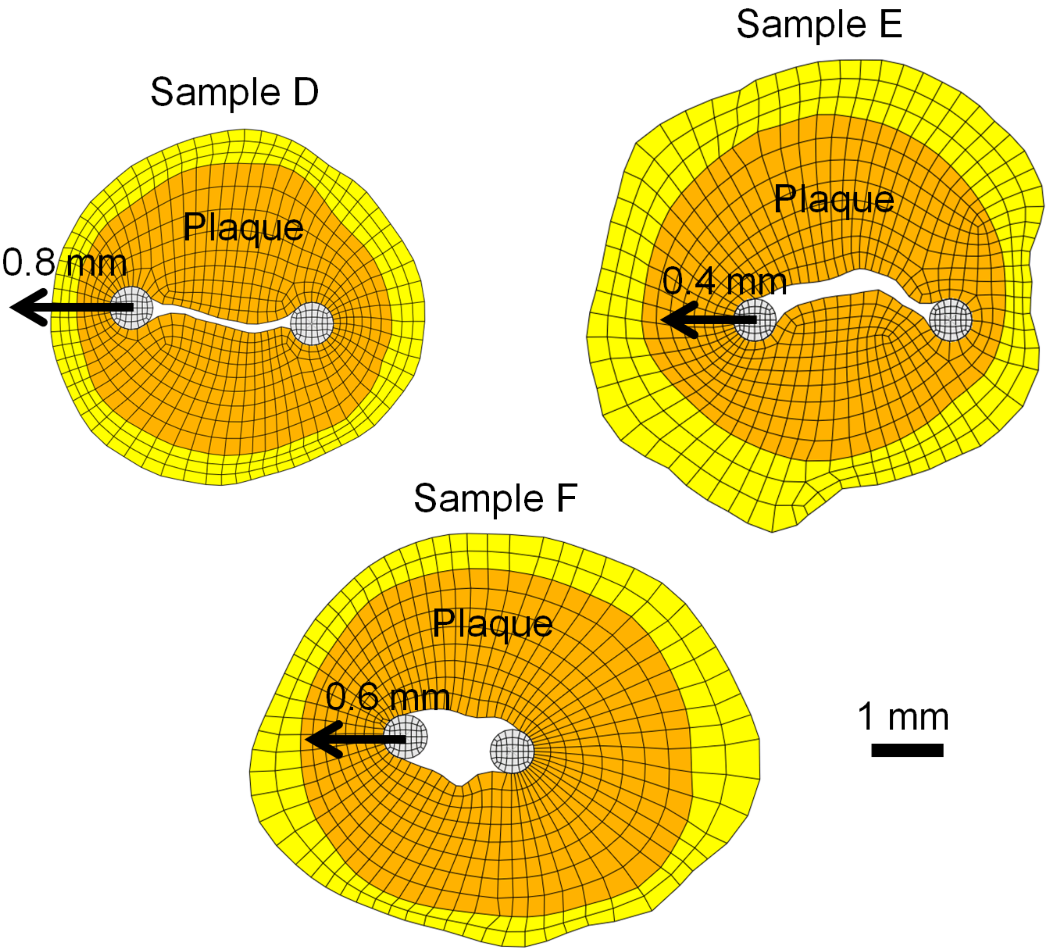

Figure 4.9 Finite element models of the atherosclerotic artery samples, mimicking the geometries and loading conditions of the experiments (see Figure 4.7).

The matching of the reaction forces of the healthy artery models and experiments (Figure 4.10) provides Ogden hyperelastic parameters as shown in Table 4.1, which also gives the error e_m normalised by the final experimental forces. The mean ± standard error of the parameters are $\mu = 95.4 \pm 29.0$ kPa and $\alpha = 25.2 \pm 2.3$, which were used for the arterial walls of the atherosclerotic artery models to proceed with the optimisation of the material parameters of the plaque elements.

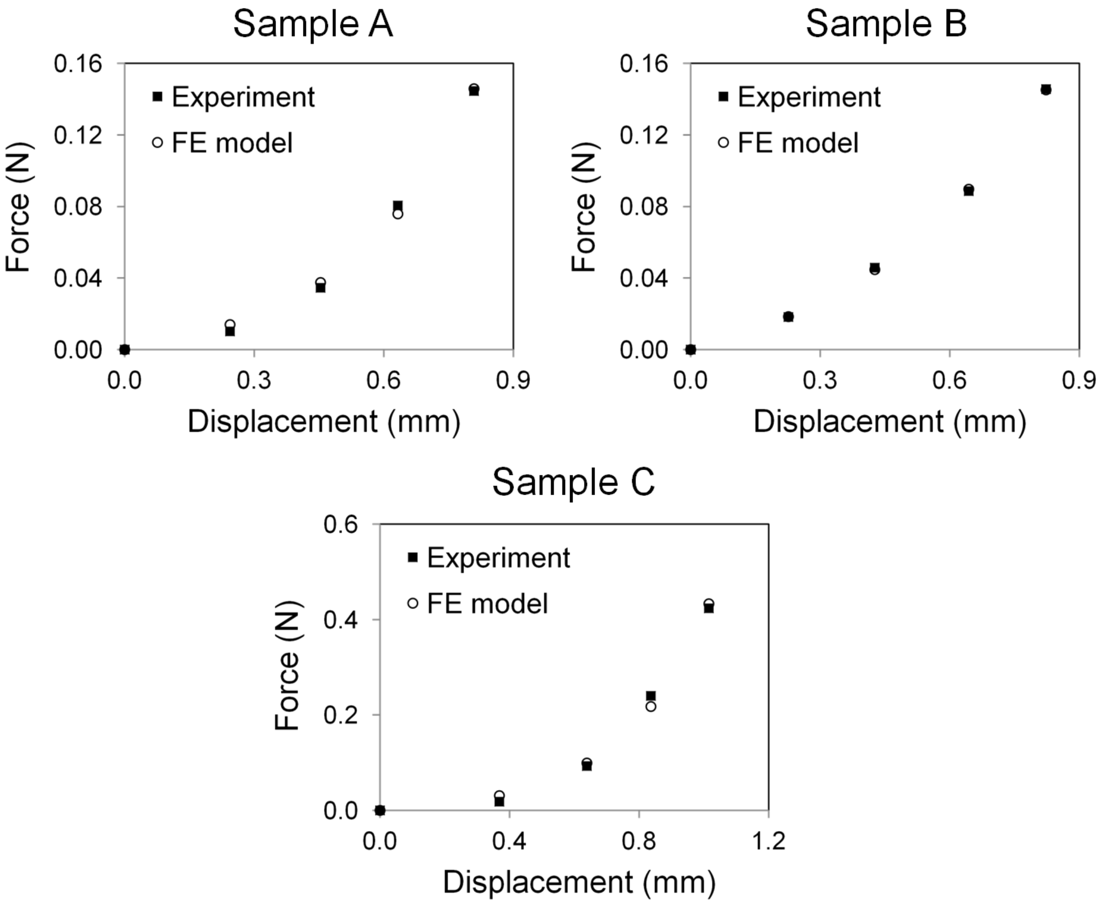

Figure 4.10 Matching of the reaction forces for the experiments and finite element (FE) models of the healthy arteries.

Table 4.1 Ogden hyperelastic shear modulus μ and hardening exponent α, and the mean normalised difference e_m between the experiment and finite element forces of the healthy artery samples.

Sample	**μ (kPa)**	**α**	**e_m (%)**
A	81.9	28.5	1.2
B	151.0	20.8	0.3
C	53.2	26.3	1.7

Table 4.2 shows the final e_{total} for the optimisation of the plaque material parameters of the three atherosclerotic arteries. There is a reduction in errors by moving from 7 × 7 to 15 × 15 material grid analysis. Figures 4.11, 4.12, and 4.13 show the experimental horizontal logarithmic strains calculated using the optical flow displacements, the final strains of the FE analysis, the normalised strain differences e_ε, and the comparison of the experimental and converged FE reaction forces for the three atherosclerotic artery samples.

Table 4.2 The final total difference e_{total} between the experiment and finite element results for the 7 × 7 and 15 × 15 material grid analyses of the atherosclerotic arteries.

Sample	**e_{total} (%)**	
	7 × 7	**15 × 15**
D	21.6	18.6
E	41.0	32.2
F	35.7	26.0

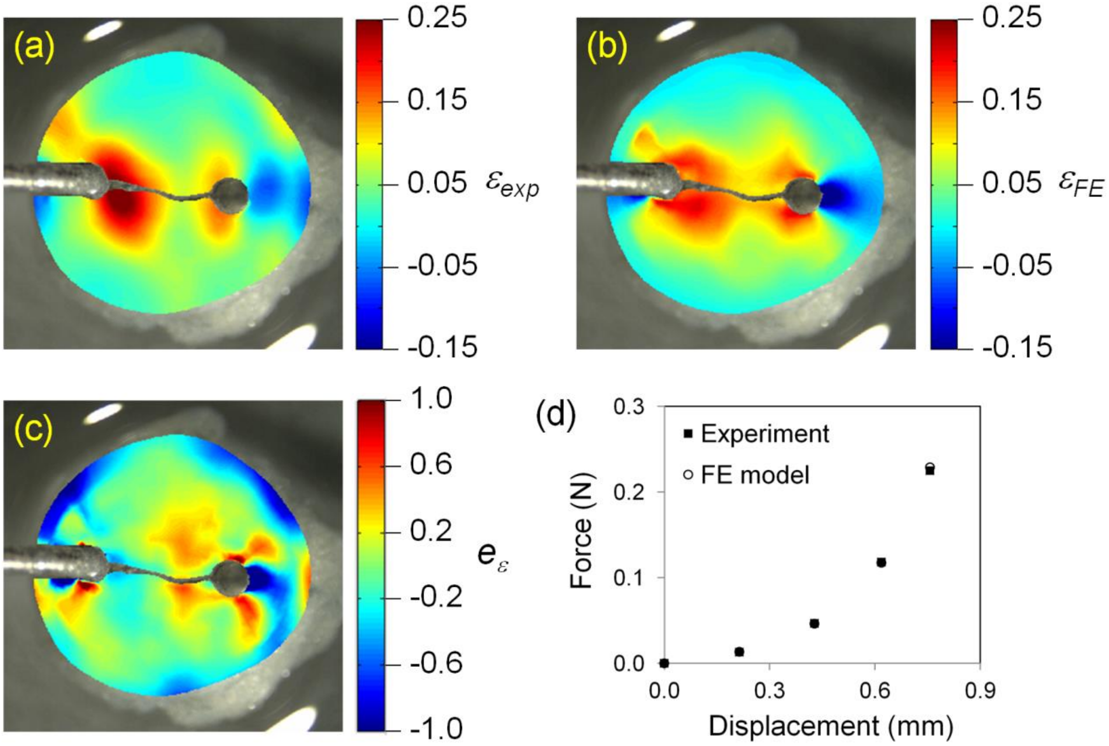

Figure 4.11 Final results of the atherosclerotic artery Sample D. Contours of the horizontal logarithm strain for the (a) experiment $\varepsilon_{\mathrm{exp}}$ and (b) finite element model $\varepsilon_{\mathrm{FE}}$, (c) the normalised strain errors e_ε, and (d) matching of the reaction forces for the experiment and finite element model.

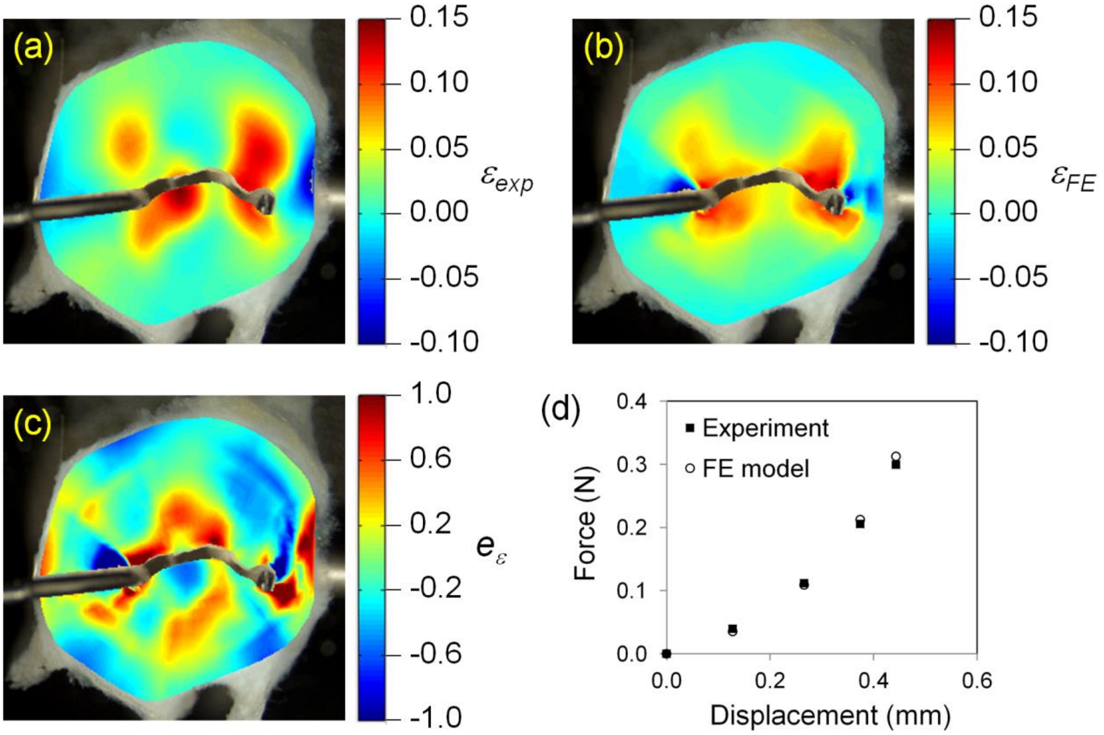

Figure 4.12 Final results of the atherosclerotic artery Sample E. Contours of the horizontal logarithm strain for the (a) experiment ε_{exp} and (b) finite element model ε_{FE}, (c) the normalised strain errors e_{ε}, and (d) matching of the reaction forces for the experiment and finite element model.

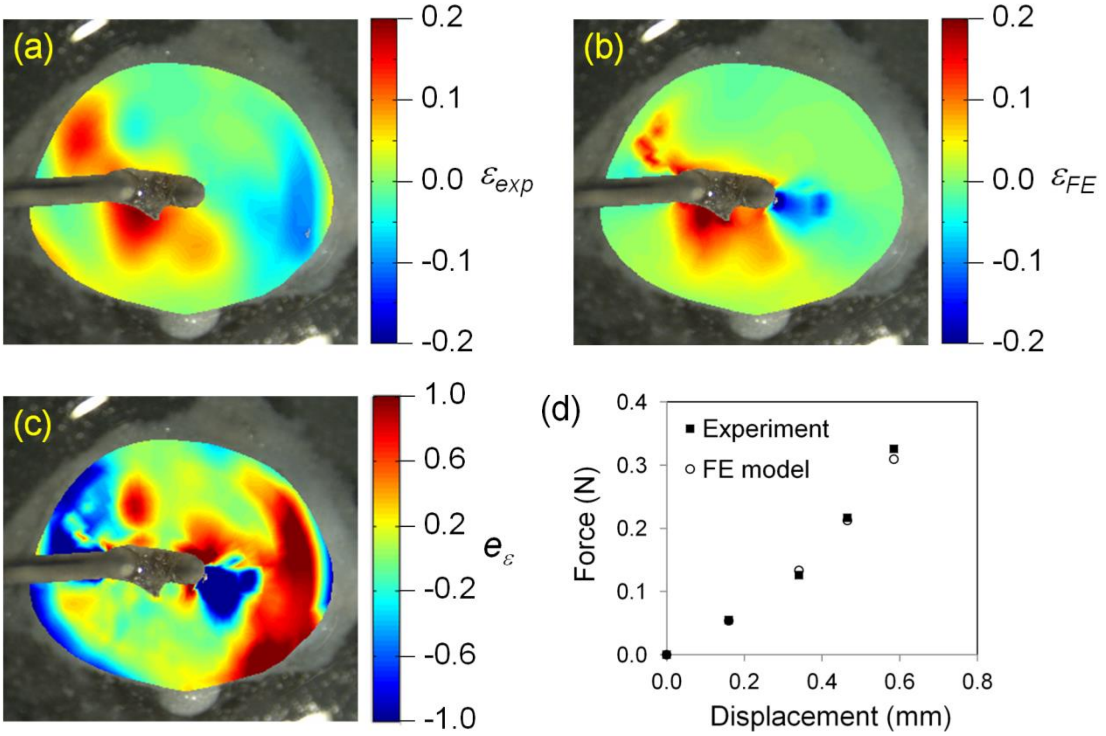

Figure 4.13 Final results of the atherosclerotic artery Sample F. Contours of the horizontal logarithm strain for the (a) experiment $\varepsilon_{\mathrm{exp}}$ and (b) finite element model $\varepsilon_{\mathrm{FE}}$, (c) the normalised strain errors e_ε, and (d) matching of the reaction forces for the experiment and finite element model.

The final values of μ in the plaque region for the atherosclerotic samples are presented in Figure 4.14, along with the sections of corresponding atherosclerotic arteries prepared using a microtome. The calcified regions of the sections were identified as the irregular regions or holes (where the microtone failed to cut through hard calcified regions) in the plaques. The converged values of α are 27.3, 37.0, and 12.0; and 80% of the plaque μ values are in the ranges of 8 – 106, 16 – 385, and 23 – 920 kPa for Samples D, E, and F, respectively.

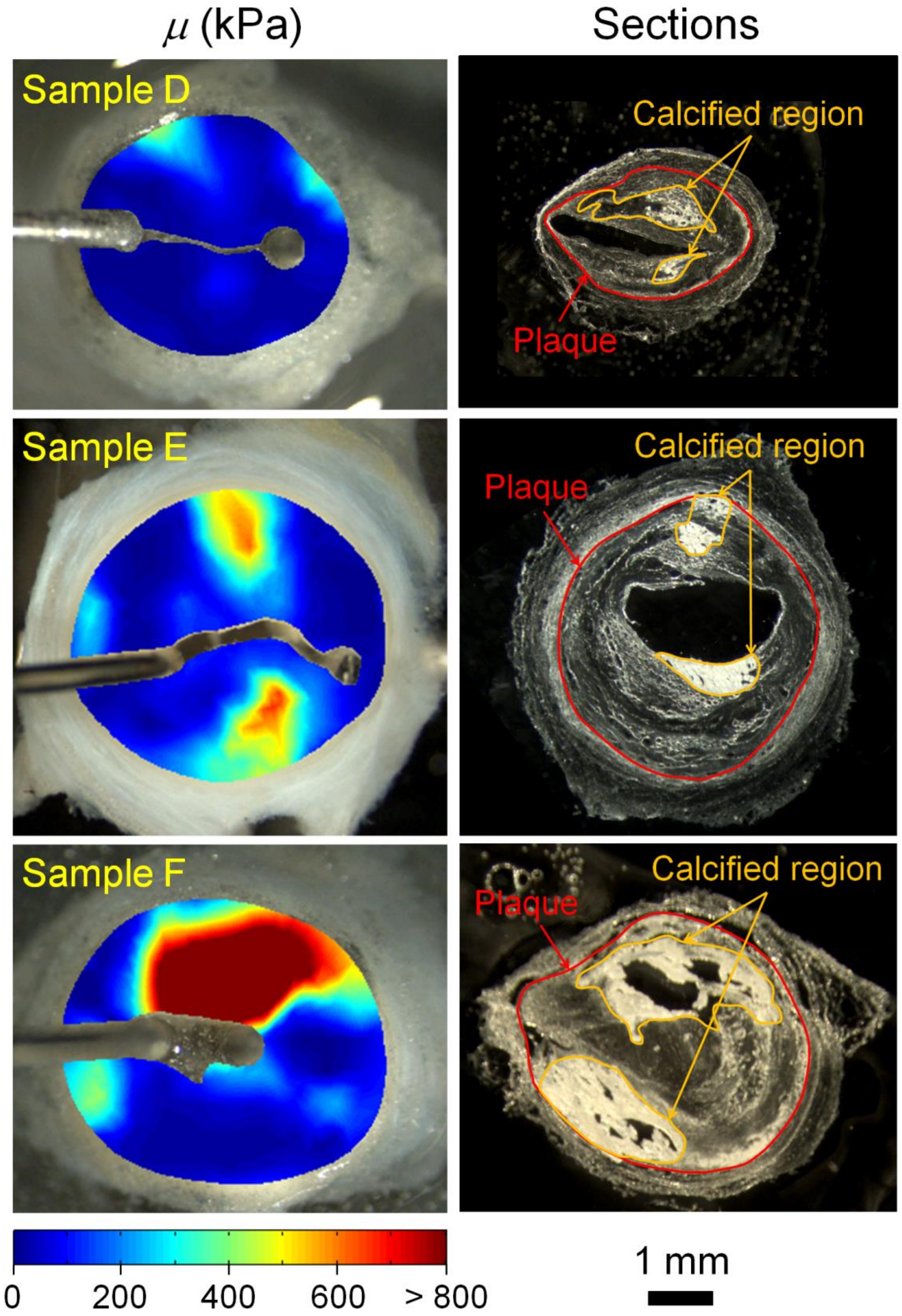

Figure 4.14. The shear modulus μ of plaque regions and the sections of the corresponding atherosclerotic artery samples. The plaques and calcified regions in the sections are highlighted with red and orange, respectively.

Table 4.3 shows the lowest values of e_{total} of the analyses for the three atherosclerotic artery samples compared to those with the μ of all plaque elements changed by ±10% or the α of plaque changed by ±5%. A summary of the μ results is presented as line graphs in Figure 4.15, showing the percentage of element area in each range of μ.

Table 4.3 The total difference e_{total} between the experiment and finite element results of the atherosclerotic arteries (original), compared with the values of e_{total} when changing the μ of plaque elements by ±10% or α by ±5%.

Sample	**e_{total} (%)**				
	Original	**+10% μ**	**-10% μ**	**+5% α**	**-5% α**
D	18.6	22.3	21.1	28.7	24.5
E	32.2	33.7	34.1	38.7	37.5
F	26.0	28.5	29.1	26.1	26.4

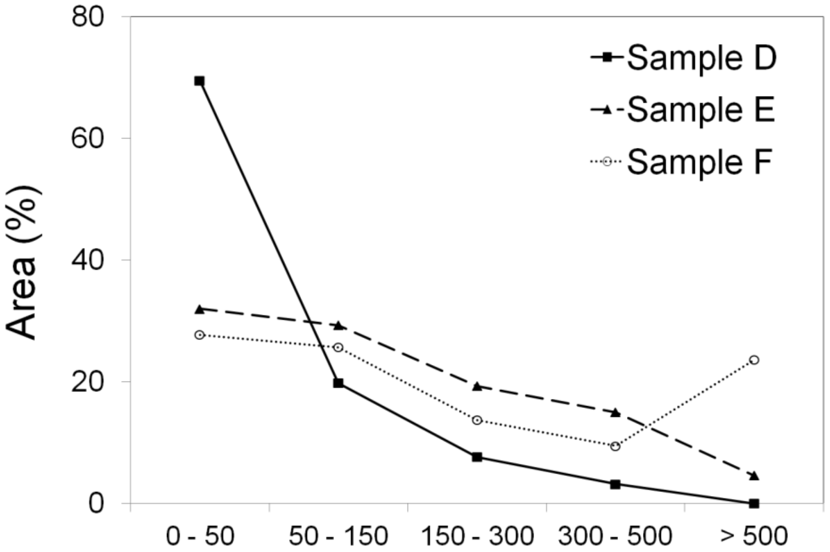

Figure 4.15 Line graphs showing the percentage of element area in each range of modulus μ for the plaques in the atherosclerotic arteries.

4.4 Discussion

Combining mechanical testing, FE analysis, and optical flow estimation, we successfully obtained an estimate of the shear modulus μ and hardening exponent α for the Ogden hyperelastic properties of each atherosclerotic artery sample. The robustness of these results was checked by comparing the final e_{total} with those after varying the μ of all plaque elements or the α of plaque. These comparisons in Table 4.3 show that slight changes of μ and α away from the optimised values lead to higher errors between experiment and FE results. For Sample D and E, the changes of α incur higher errors than the changes of μ due to their highly hyperelastic properties (higher α); whereas the influence of α is less for Sample F which has more linear properties (lower α). Comparing the contours of μ to the section slides in Figure 4.14, the high modulus regions of the atherosclerotic plaques coincide reasonably well with the calcified regions. Some of the mismatches may be due to the inconsistent geometries between the mechanical test and histology sections, or the potential variable composition along the 4 mm length of the tested specimens. Despite these, the reasonable matches at most of the arterial regions further validate the results that were obtained and provide confidence in the approach developed.

One major limitation of the approach is the non-physiological tensile loading on the arterial ring. This results in difficulties in determining the mechanical loads that correspond to the internal physiological pressures. This also causes inaccurate results at both loading ends, which was partially solved by neglecting these regions for the analysis. In contrast, an inflation test applying internal pressure on a section of artery does not have these limitations. However, this method requires mounting of both ends of the artery onto two cannulae in order to apply internal pressure, preventing the imaging of the arterial cross-section. In this case, ultrasound imaging can be used to capture the cross-sectional deformation, but this raises a concern on the accuracy of the measurements due to non-direct imaging on the arterial cross-section. An alternative way of applying internal pressure is using a small inflatable device in the lumen, but challenges arise while dealing with small or diseased arteries with seriously occluded lumen. Therefore, the tensile ring test is considered to be a reasonable compromise solution.

Several other approaches have been suggested by other studies to determine the mechanical properties of atherosclerotic artery. Beattie *et al.* (1998) used an experimental-computational method to correlate the strain results obtained from *in vitro* inflation tests on human atherosclerotic aorta rings with those of FE models. Their inverse FE approach allows determination of the elastic moduli of four separated zones: disease free, lipid, fibrous tissue, and calcified zones.

Using the results of IVUS elastography and FE modelling, Baldewsing *et al.* (2004a, 2004b) suggested an approach to estimate the Young's moduli of the specific regions of atherosclerotic artery. The approach was then improved by incorporating an iterative reconstruction method to find appropriate Young's modulus (Baldewsing et al. 2005), and deformable curves to determine more accurate geometry for the plaque regions (Baldewsing et al. 2006). In a more recent study, they extended the framework to reconstruct the arbitrary plaque with a more heterogeneous structure, using the combination of global and local reconstructions (Baldewsing et al. 2008). While Baldewsing's group has carried out extensive refinement on the approach to better estimate the plaque mechanical properties, the capability of the model to extract the plaque morphology that exhibits several neighbouring lipid cores and calcium inclusions is limited.

In order to solve this, Le Floc'h *et al.* (2009, 2010) suggested another plaque elasticity reconstruction approach, aiming to reduce the geometry parameters and track higher material variation of the plaque. They used iterative inverse FE reconstruction, and sequentially increased the number of separated regions in the plaque based on the difference in estimated Young's moduli. They have validated this approach using *in vivo* IVUS elastograms (Le Floc'h et al. 2009) and the deformation of an artificial artery (Le Floc'h et al. 2010).

While these studies enhanced the development of a clinically applicable technique on tracking the material properties of atherosclerotic plaque thereby predicting its rupture potential, their consideration of the real plaque heterogeneous morphology is limited. The plaque modelling was separated into several regions with specific Young's modulus, as in the recent studies of Hayenga *et al.* (2011), Chai *et al.* (2013), and Heiland *et al.* (2013). Giving the conditions that the tested strains were small, the material nonlinearity of the artery and plaque was also neglected. In contrast, the approach in this chapter allows determination of truly heterogeneous material properties for the plaque, and accounted for the material nonlinearity by assigning hyperelastic functions to both arterial wall and plaque.

The reported material properties of the atherosclerotic plaque vary between different studies. The above mentioned study from Beattie *et al.* (1998) shows Young’s moduli of 4 and 40 kPa for the low and high strains of the plaque lipid region, and 400 and 11000 kPa for those of the calcified region. Baldewsing *et al.* (2004a, 2008) reported a variation of Young’s modulus from 25 to 1500 kPa in the atherosclerotic plaque, showing the low and high moduli of the lipid and fibrosis regions, respectively. In addition, Le Floc'h *et al.* (2009) determined that the Young’s moduli of the plaque range from 10 to 3000 kPa, using starting values derived from other studies (Cheng et al. 1993, Finet et al. 2004, Lee et al. 1991).

While it is expected that the moduli of the atherosclerotic plaque regions vary with disease conditions and testing methodology, our results show modulus ranges that agree with these reported values. Among the three tested atherosclerotic samples, Sample D shows a mild calcification whereas Sample F shows the most severe calcification of plaque (Figure 4.14). To compare the results, the elastic modulus is estimated from the properties μ and α as the slope of the stress-strain curve in uniaxial mode assuming incompressible behaviour (Abaqus Theory Manual, Section 4.6.2). The majority of the elastic moduli of Samples D and F at 1% strain range from 27 to 360 kPa and 72 to 2900 kPa, respectively, which are comparable to the results of Le Floc'h *et al*. (2009) and Baldewsing *et al.* (2008). In addition, the estimated elastic moduli of the healthy human coronary artery samples have a mean value of 2100 kPa at a physiological strain of 10% (Veress et al. 2002), which is close to the reported mean values of 1200 and 4500 kPa by Gow and Hadfield (1979) with *in vivo* and *in vitro* tests respectively, and the value range of 900 to 4100 kPa by Ozolanta *et al*. (1998) under *in vitro* inflation tests with physiological pressures.

Further improvements can be made on the experimental and computational methodologies of this study, where many of them have been addressed in the review of Walsh *et al.* (2014). The numbers of samples are low for both healthy and atherosclerotic arteries in this study; more samples can be tested in future studies and statistical analysis of the results can be included. The artery samples were immersed in water during the experiments where swelling of the tissues may have occurred. Krebs or phosphate buffered saline solution has been used in the experiments in the later chapters.

The artery rings were not subjected to physiological pre-stretch in both the loading and axial directions. The pre-stretch at the loading direction with a physiological baseline pressure load is useful for comparison with *in vivo* data. In this study, the effects of this pre-stretch can be estimated with a rescale in the response curve. *In vivo* axial stresses influence the overall mechanical properties of an artery (Humphrey et al. 2009). Ideally, an axial pre-load that corresponds to the *in vivo* axial stretch should be applied in an *in vitro* mechanical test. This can be achieved by using an inflation test on a section of artery with both ends mounted and connected to a load cell. In this case, ultrasound imaging can be used to obtain the arterial cross-sectional deformation as in the studies of Baldewsing *et al.* (2004a, 2004b). Alternatively, a small improvement on the ring test can be done by recording the thinning of the sample in the longitudinal direction during the test to account for the axial deformation.

The viscoelasticity and anisotropic nature of the artery have not been taken into consideration. The testing equipment limited the frequency of the cyclic loading, thus a dynamic test with a physiological frequency that corresponds to human heart rate was not performed. Future improvements of the equipment can be done to incorporate the dynamic behaviour of the artery in order to study the arterial viscoelastic properties as in the study of Heiland *et al.* (2013). Besides, the mechanical properties of the arteries were analysed in the horizontal direction which corresponds to the arterial circumferential direction, the major loading direction in the physiological condition. However, the anisotropy of atherosclerotic plaque has been shown to play important role on the mechanical properties of plaque (Chai et al. 2014, Holzapfel et al. 2004), thus it should be taken into consideration in future studies.

Furthermore, the cutting of the tissues may have disrupted the integrity of the collagen fibres thus changing the mechanical properties of the arterial cross-section. While this may not change the overall properties of a sample that has a significant length (4 mm in this study), a better approach to prevent this issue is using an inflation test on a long section of mounted artery and recording the cross-sectional deformation with ultrasound imaging.

While a validation of the optical flow technique has been performed in Chapter 3, the image analysis of the experiments can be further validated using a phantom with known mechanical properties. This will also enable determination of smoothness parameters that are more reliable for the real experiments. In addition, the linear interpolation of material parameters cannot account for a sharp transition at the border of the plaque components. Future improvements on the optical flow technique and the captured images will reduce the required smoothing process and improve the resolution of the strain field, thus reducing the error caused by interpolation.

4.5 Conclusion

An approach combining experimental tensile ring tests, FE modelling, and optical flow image analysis has been developed to determine the heterogeneous mechanical properties of atherosclerotic artery. The matching of experiment and FE results and the optimisation of material parameters provide a reasonable and sensible estimate of the shear modulus of the tested human atherosclerotic coronary arteries. Future work can incorporate the effects of pharmacological drugs on vascular smooth muscle response in these techniques, which will allow the investigation of the differences in these effects between healthy and diseased arteries. The *in vitro* experiment results obtained with this approach can also be used to verify the *in vivo* ultrasound imaging measurements obtained from patients. These findings will enable further understanding on the biomechanical properties of atherosclerotic artery, thus promoting the development of new treatment strategies for atherosclerosis.

4.6 References

Abaqus Theory Manual, Section 4.6.1. *Abaqus 6.9 Documentation Collection*. Dassault Systèmes Simulia, Providence, USA.

Abaqus Theory Manual, Section 4.6.2. *Abaqus 6.9 Documentation Collection*. Dassault Systèmes Simulia, Providence, USA.

Akyildiz AC, Speelman L, Gijsen FJ. Mechanical properties of human atherosclerotic intima tissue. *J Biomech*. 47(4):773-783, 2014.

Baldewsing RA, Danilouchkine MG, Mastik F, Schaar JA, Serruys PW, van der Steen AFW. An inverse method for imaging the local elasticity of atherosclerotic coronary plaques. *IEEE Trans Inf Technol Biomed*. 12(3):277-289, 2008.

Baldewsing RA, de Korte CL, Schaar JA, Mastik F, van der Steen AFW. A finite element model for performing intravascular ultrasound elastography of human atherosclerotic coronary arteries. *Ultrasound Med Biol*. 30(6):803-813, 2004a.

Baldewsing RA, de Korte CL, Schaar JA, Mastik F, van der Steen AFW. Finite element modeling and intravascular ultrasound elastography of vulnerable plaques: parameter variation. *Ultrasonics.* 42(1-9):723-729, 2004b.

Baldewsing RA, Mastik F, Schaar JA, Serruys PW, van der Steen AFW. Young's modulus reconstruction of vulnerable atherosclerotic plaque components using deformable curves. *Ultrasound Med Biol*. 32(2):201-210, 2006.

Baldewsing RA, Schaar JA, Mastik F, Oomens CWJ, van der Steen AFW. Assessment of vulnerable plaque composition by matching the deformation of a parametric plaque model to measured plaque deformation. *IEEE Trans Med Imaging* 24(4):514-528, 2005.

Beattie D, Xu G, Vito R, Glagov S, Whang WG. Mechanical analysis of heterogeneous, atherosclerotic human aorta. *J Biomech Eng*. 120(5):602-607, 1998.

Carew TE, Vaishnav RN, Patel DJ. Compressibility of the arterial wall. *Circ Res*. 23(1):61-68, 1968.

Chai CK, Akyildiz AC, Speelman L, Gijsen FJ, Oomens CW, van Sambeek MR, van der Lugt A, Baaijens FP. Local axial compressive mechanical properties of human carotid atherosclerotic plaques-characterisation by indentation test and inverse finite element analysis. *J Biomech*. 46(10):1759-1766, 2013.

Chai CK, Speelman L, Oomens CW, Baaijens FP. Compressive mechanical properties of atherosclerotic plaques-Indentation test to characterise the local anisotropic behaviour. *J Biomech*. 47(4):784-792, 2014.

Cheng GC, Loree HM, Kamm RD, Fishbein MC, Lee RT. Distribution of circumferential stress in ruptured and stable atherosclerotic lesions. A structural analysis with histopathological correlation. *Circulation*. 87(4):1179-1187, 1993.

Falk E, Shah PK, Fuster V. Coronary plaque disruption. *Circulation*. 92(3)657-671, 1995.

Finet G, Ohayon J, Rioufol G. Biomechanical interaction between cap thickness, lipid core composition and blood pressure in vulnerable coronary plaque: impact on stability or instability. *Coron Artery Dis*. 15(1):13-20, 2004.

Gow BS and Hadfield CD. The elasticity of canine and human coronary arteries with reference to postmortem changes. *Circ Res*. 45(5):588-594, 1979.

Hayenga HN, Trache A, Trzeciakowski J, Humphrey JD. Regional atherosclerotic plaque properties in ApoE-/- mice quantified by atomic force, immunofluorescence, and light microscopy. *J Vasc Res*. 48(6):495-504, 2011.

Heiland VM, Forsell C, Roy J, Hedin U, Gasser TC. Identification of carotid plaque tissue properties using an experimental-numerical approach. *J Mech Behav Biomed Mater*. 27:226-238, 2013.

Holzapfel GA, Sommer G, Regitnig P. Anisotropic mechanical properties of tissue components in human atherosclerotic plaques. *J Biomech Eng*. 126(5):657-665, 2004.

Humphrey JD, Eberth JF, Dye WW, Gleason RL. Fundamental role of axial stress in compensatory adaptations by arteries. *J Biomech*. 42(1):1-8, 2009.

Le Floc'h S, Cloutier G, Finet G, Tracqui P, Pettigrew RI, Ohayon J. On the potential of a new IVUS elasticity modulus imaging approach for detecting vulnerable atherosclerotic coronary plaques: *in vitro* vessel phantom study. *Phys Med Biol*. 55(19):5701-5721, 2010.

Le Floc'h S, Ohayon J, Tracqui P, Finet G, Gharib AM, Maurice RL, Cloutier G, Pettigrew RI. Vulnerable atherosclerotic plaque elasticity reconstruction based on a segmentation-driven optimization procedure using strain measurements: theoretical framework. *IEEE Trans Med Imaging*. 28(7):1126-1137, 2009.

Lee RT, Grodzinsky AJ, Frank EH, Kamm RD, Schoen FJ. Structure-dependent dynamic mechanical-behavior of fibrous caps from human atherosclerotic plaques. *Circulation*. 83(5):1764-1770, 1991.

Ozolanta I, Tetere G, Purinya B, Kasyanov V. Changes in the mechanical properties, biochemical contents and wall structure of the human coronary arteries with age and sex. *Med Eng Phys*. 20(7):523-533, 1998.

Pasterkamp G and Falk E. Atherosclerotic plaque rupture: an overview. *J Clin Basic Cardiol*. 3(2):81-86, 2000.

Sun D, Roth S, Black MJ. Secrets of optical flow estimation and their principles. *IEEE Conf Comput Vis Pattern Recognit*. 2432-2439, 2010.

Veress AI, Weiss JA, Gullberg GT, Vince DG, Rabbitt RD. Strain measurement in coronary arteries using intravascular ultrasound and deformable images. *J Biomech Eng*. 124(6):734-741, 2002.

Walsh MT, Cunnane EM, Mulvihill JJ, Akyildiz AC, Gijsen FJ, Holzapfel GA. Uniaxial tensile testing approaches for characterisation of atherosclerotic plaques. *J Biomech*. 47(4):793-804, 2014.

5. Experimental and Finite Element Analyses of the Active Mechanical Properties of Atherosclerotic Artery

5.1 Introduction

Studies have shown that the risk of atherosclerotic plaque rupture can be reduced by treatments with statins (Crisby et al. 2001, Martín-Ventura et al. 2005, Nissen et al. 2005), β-blockers (Hedblad et al. 2001, Wiklund et al. 2002), or calcium antagonists (Zanchetti et al. 2002, Nissen et al. 2004). While statins potentially stabilise the plaque by decreasing inflammation and lipid accumulation in the plaque (Crisby et al. 2001, Martín-Ventura et al. 2005), the detailed mechanisms of how β-blockers and calcium antagonists function on plaque stabilisation remain unclear. It is speculated that these vasodilators stabilise the atherosclerotic plaque by changing the response of vascular smooth muscle cells to external mechanical loading, which changes the overall arterial mechanical property. Therefore, it is crucial to investigate the mechanisms of how atherosclerotic arteries respond to pharmacological drugs and the differences between the active properties of the healthy and diseased arteries.

The mechanical properties of atherosclerotic arteries have been widely studied both *in vitro* (Beattie et al. 1998, Holzapfel et al. 2004, Baldewsing et al. 2008) and *in vivo* (van Popele et al. 2001, Baldewsing et al. 2008, Wykretowicz et al. 2009), where the diseased artery has been shown to be stiffer than the healthy artery in clinical studies (van Popele et al. 2001, Wykretowicz et al. 2009). Holzapfel and Ogden (2010) have provided a review of the studies that worked on the theoretical modelling of arterial smooth muscle function. These include the study of Yang *et al.* (2003) on a model integrating the electro- and mechano-chemical functions of the smooth muscle cell, as well as that of Zulliger *et al*. (2004) on a pseudo-strain energy function describing the arterial mechanical properties with the coupling of collagen, elastin, and smooth muscle active properties.

In vitro vasoconstrictor functional assays have been performed by Dr. Maguire on fresh human healthy and atherosclerotic arteries within 12 hours of retrieval (Ooi et al. 2014). The results show that endothelin-1 (ET-1) mediated constrictor responses are not significantly attenuated in the atherosclerotic arteries (Figure 5.1) despite extensive thinning of the media smooth muscle layer with atherosclerosis, as shown by Burke *et al.* (2002). A similar phenomenon was also observed in the aorta of mice, where 50% ablation of smooth muscle cells did not cause subsequent loss of ET-1 response. These contradict the expectation that the thinning of the muscle layer should lead to reduced muscle response in the diseased artery.

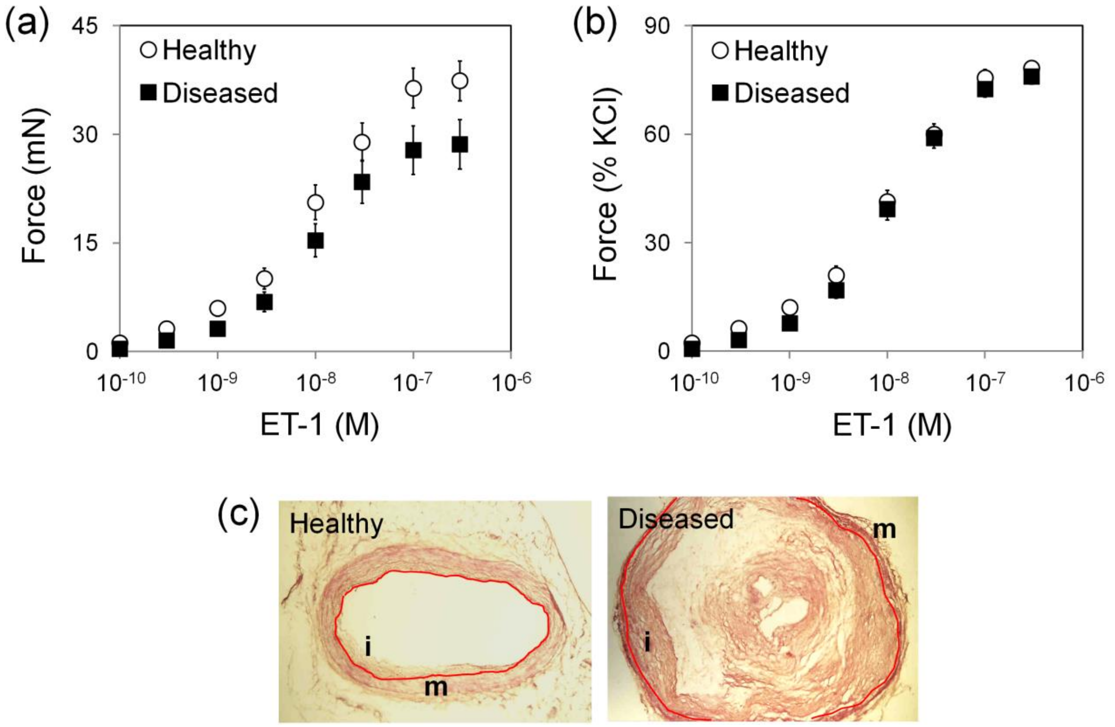

Figure 5.1 Results of the vasoconstrictor functional assays performed by Dr. Maguire (Ooi et al. 2014). (a) Reaction forces (mean ± standard error) of the contractile responses to endothelin-1 (ET-1) of healthy (n = 68) and atherosclerotic diseased (n = 55) human coronary arteries expressed in mN tensile force. (b) The same force data normalised to the response of 100 mM KCl (another vasoconstrictor) in each vessel ring. (c) Histology sections of representative healthy and atherosclerotic diseased coronary arteries, showing thinned media (m), thickened intima (i), and narrowed lumen with the disease. Red lines separate contractile media from non-contractile intima.

Despite the well-modelled arterial smooth muscle functions in the aforementioned studies, the changes of the active properties with atherosclerotic disease which resulted in the unexpected ET-1 response remain unclear. In order to understand these mechanisms, further experiments and computational modelling have been carried out. The results of passive arterial ring tests (without smooth muscle cells activation) performed by Dr. Sutcliffe on healthy and atherosclerotic arteries were first analysed and matched with those of the finite element (FE) models to obtain the passive mechanical properties of the arteries. While comparing these properties between the two groups, the derived passive properties were used with further FE modelling of the experiments of Dr. Maguire on arterial active response to ET-1 (Figure 5.1a). This provides an understanding of how the atherosclerosis-induced changes of arterial structure and mechanical properties affect the arterial active response to ET-1, which plays an important role in discovering new drugs for the treatment of atherosclerotic disease.

5.2 Methods

5.2.1 Tensile ring tests

Tensile ring tests were carried out by Dr. Sutcliffe to determine the passive mechanical properties of healthy and atherosclerotic human coronary arteries. Anonymised human coronary artery samples were collected with patient consent and ethical approval. Histologically healthy arteries ($n = 5$) were from patients transplanted for cardiomyopathies and atherosclerotic arteries ($n = 6$) were from patients transplanted for ischaemic heart disease. The arterial samples were snap-frozen to maintain structural integrity, stored at -70 °C and defrosted before use. The defrosted samples were expected to have negligible smooth muscle cell activation induced by stretching.

An arterial ring with 3 mm length was harvested from each of the artery and set up for tensile testing in a 5 ml organ bath containing oxygenated Krebs solution at 37 ºC (Figure 5.2). All of the 3 mm atherosclerotic artery segments contained visible atherosclerotic plaque although the plaque size varied between samples. Several uniaxial displacement cycles were applied and the reaction forces and deformation images of the side of the artery were recorded; the last cycle was used for the data analysis. The magnitudes of the displacements for the healthy and atherosclerotic artery rings range from 1.3 – 3.9 mm and 0.8 – 3.1 mm, respectively. The mechanical stretch λ of the ring was calculated as:

$$\lambda = \frac{2L}{C_i} \tag{5.1}$$

where L is the distance between the two wire probes that were used to stretch the arterial ring, and C_i is the inner circumference of the ring without loading, measured from the histology of the artery section adjacent to the tested ring (Figure 5.2c).

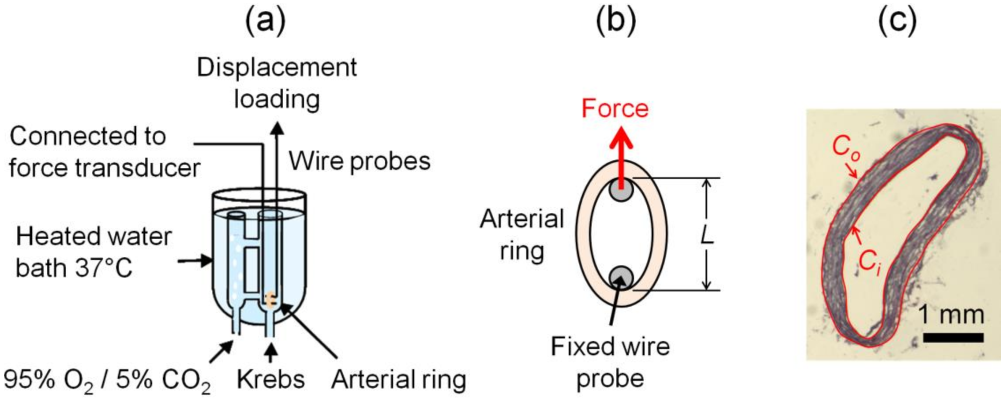

Figure 5.2 (a) The setup of the tensile ring test for obtaining the passive mechanical properties of arteries, with (b) showing the mounting of an artery ring on the wire probes, the direction of applied force, and the lumen length L. (c) The histology of the artery section adjacent to the tested ring, showing the inner and outer circumferences C_i and C_o.

5.2.2 Finite element modelling of arterial passive mechanical properties

For each healthy artery sample a two-dimensional plane stress FE model with plane thickness of 3 mm was created using Abaqus (version 6.11, Dassault Systèmes Simulia, Providence, USA), comprising a single circular ring (Figure 5.3a). A perfect ring model was used since the arterial deformations were recorded only from the side for extracting the overall mechanical properties, and there was no measurement of cross-sectional deformations. The inner and outer radii r_i and r_o of the ring were determined using the measured inner and outer arterial circumferences C_i and C_o from the histology (Figure 5.2c), where $C_i = 2\pi r_i$ and $C_o = 2\pi r_o$. The models were assigned with first order Ogden hyperelastic properties with shear modulus μ and hardening exponent α, assuming incompressible material by using a very small value (1×10^{-8} m^2/N) of the compressibility parameter D (Abaqus Theory Manual, Section 4.6.1). The model reaction forces were matched with those of the corresponding tensile ring tests using an error minimisation approach with MATLAB (version 7.13/R2011b, MathWorks, Natick, USA) to determine the optimum μ and α that provide the best matching. The mean values of μ and α of the healthy artery models were then calculated.

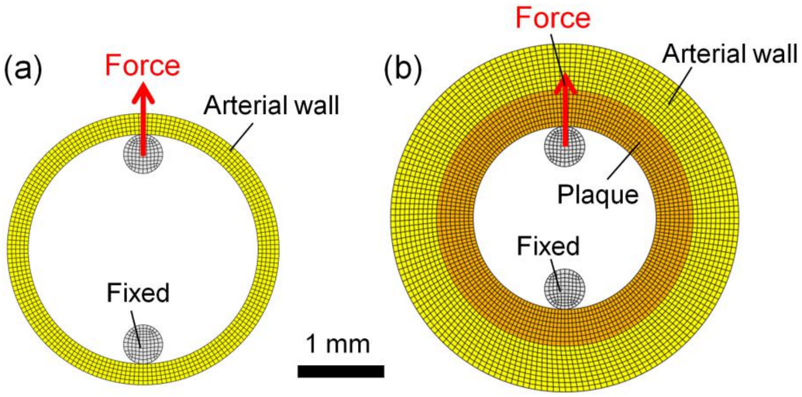

Figure 5.3 One of the (a) healthy and (b) atherosclerotic artery models of the tensile ring tests. A different model was created for each test with an arterial geometry and loading condition that mimic those in the test.

A similar approach was applied to the atherosclerotic artery models, with an additional inner vessel wall layer included to represent plaque tissue (Figure 5.3b). The outer wall layer was assigned with the mean values of μ and α determined from the healthy artery models. The additional inner plaque layer was assumed to be homogeneous to extract the overall hyperelastic properties, and was assigned with different μ and α with the optimum values determined by matching the modelled force-displacement results with those of the corresponding tensile ring test.

In order to compare the overall stiffness of the healthy and atherosclerotic arteries, each of the FE models was loaded with internal physiological pressures of 80 mmHg and 120 mmHg. The arterial distensibility D_a of each sample was determined from the geometry changes of the model using Equation (5.2):

$$D_a = \frac{A_{120} - A_{80}}{A_{80}(P_{120} - P_{80})} \tag{5.2}$$

where A_{80}, A_{120}, P_{80}, and P_{120} are the lumen area A and pressure P at 80 and 120 mmHg, respectively. The stiffness of the arteries was determined by this normalised D_a (i.e. change of lumen area normalised by the initial area) rather than the non-normalised D_a to exclude the influence of the significant geometry differences between the healthy and diseased groups.

5.2.3 Finite element modelling of arterial endothelin-1 response

Without the access to the arterial images, FE models that have the geometries of idealised healthy and atherosclerotic artery rings were created. The healthy artery model contained two separated regions of adventitia and media (Figure 5.4a), with diameter and wall thickness estimated from the arterial rings used in the tensile ring experiments. Both of these regions were assigned with the previously derived mean values of hyperelastic μ and α of the healthy artery models. The media layer was assigned with an additional thermal expansion property to model the muscle force generation in response to the addition of ET-1 under isometric conditions, where applied temperature in the model represents the applied concentration of ET-1 used in the vasoconstriction experiments. The thermal expansion property was modelled with an error function (erf) (Equation 5.3) within an Abaqus user subroutine (Appendix III) to control the generated reaction forces that match the ET-1 experiments:

$$\varepsilon = P_1[\mathrm{erf}(P_2T)]^{P_3} \tag{5.3}$$

where ε and T are the strain and applied temperature, respectively, and P_1, P_2, and P_3 are three parameters that were modified to generate the forces that match the ET-1 vasoconstriction experiments.

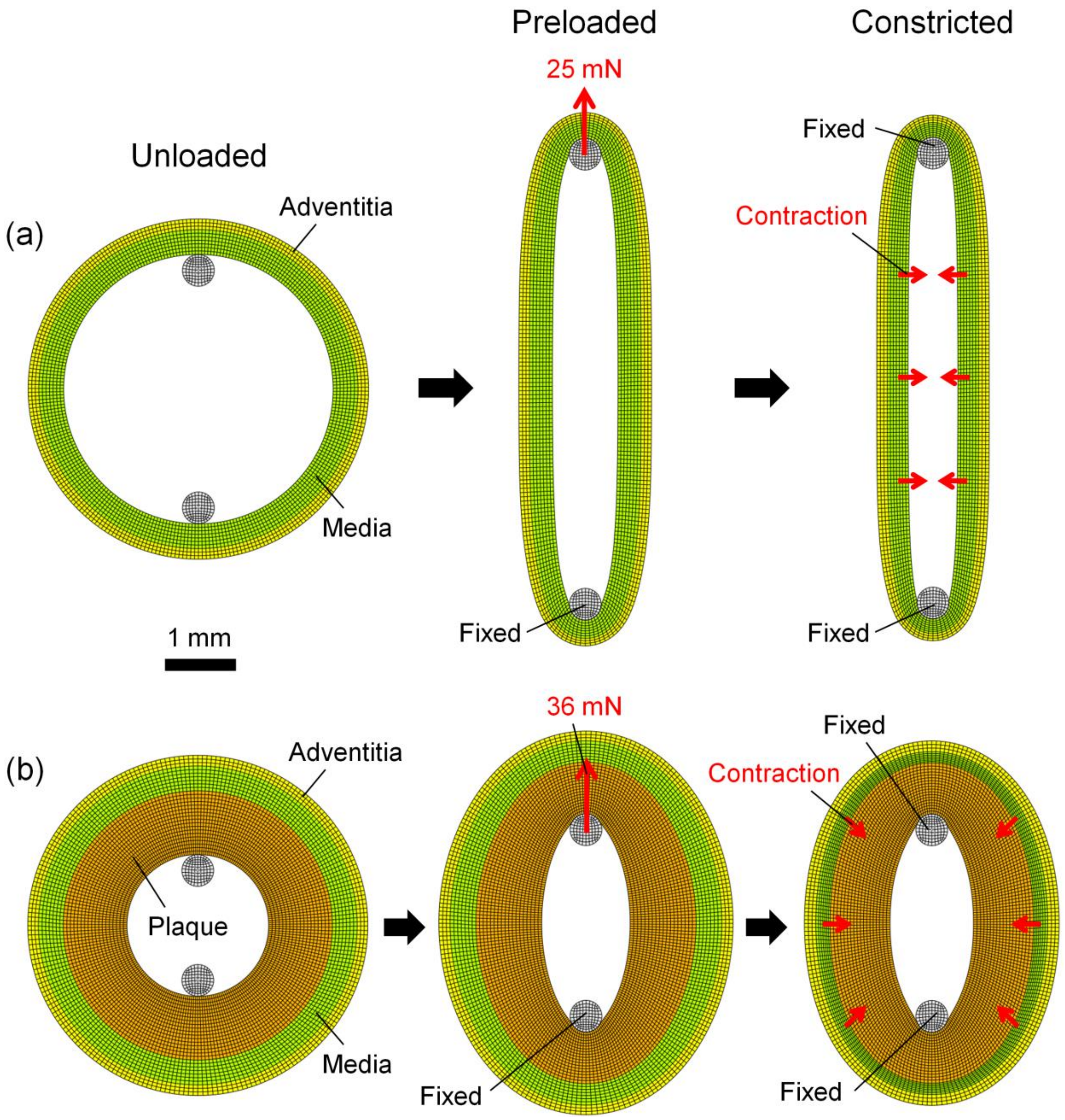

Figure 5.4 (a) Healthy and (b) atherosclerotic artery models for the modelling of the endothelin-1 response of arteries, showing the unloaded, pre-loaded, and constricted states of the arteries. All of the elements in the media layer were assigned with a thermal property to contract in response to the applied temperature.

The idea of this modelling approach is to use the thermal modelling capability within the Abaqus FE software to represent directly the contractile effect of ET-1. The relationship between thermal strain and temperature represented in Equation (5.3) should be interpreted directly as the effect of ET-1 concentration T on the muscle contraction strain ε. The value of P_1 governs the maximum contractile response in the muscle, while P_2 and P_3 control the shape of the curve representing the relationship between contractile strain and ET-1 concentration (P_2 determines the shift of the curve to left or right and P_3 determines the slope of the curve).

The model was first applied with a pre-stretch load of 25 mN which corresponds to the mean basal tensile force determined by the normalisation procedure in the vasoconstriction studies in healthy arteries. Thermal loadings of the same magnitudes as the administered ET-1 concentrations were then applied. The force results of the model were compared to those of the ET-1 vasoconstriction experiment and an error minimisation approach was performed using MATLAB to change the three parameters of Equation (5.3) with multiple iterations until a minimum average difference between measured and predicted forces was achieved.

The model of the atherosclerotic artery ring was then created, which contained an additional layer of plaque (Figure 5.4b). The geometries of the adventitia and media layers remained the same as those of the healthy artery model for direct comparison, whereas the size of the plaque layer was estimated from the atherosclerotic samples used in the tensile ring experiments. The adventitia and media were again modelled with the same hyperelastic properties as those of the healthy model, and the media layer was assigned with thermal characteristics of Equation (5.3) but with different parameters representing diseased muscle tone. The plaque region was assigned with hyperelastic μ and α parameters to be determined from the atherosclerotic artery passive tensile tests. A pre-stretch load of 36 mN was applied, derived from the normalised basal tensile force determined in the vasoconstriction study of atherosclerotic arteries, and the same thermal loadings were applied. The reaction forces were then matched with the contractile responses to ET-1 using a MATLAB error minimisation approach by modifying the P_1, P_2, and P_3 thermal parameters of the atherosclerotic model.

The atherosclerosis-induced changes of arterial contraction under physiological condition were then examined by applying internal pressures of 80 and 120 mmHg to both healthy and atherosclerotic models, along with a thermal loading of 3×10^{-7} K (equivalents to 3×10^{-7} M ET-1). The distensibility D_a of each model was then calculated using Equation (5.2), and comparisons were made between the cases of no muscle contraction (passive), applying the determined healthy muscle tone to both models, and applying diseased muscle tone to the atherosclerotic model.

5.3 Results

5.3.1 Passive mechanical properties of healthy and atherosclerotic arteries

The passive force-stretch relationships of the healthy and atherosclerotic arteries determined from the tensile ring tests are shown in Figure 5.5. One of the healthy artery samples was considered an outlier and not included in the results. Matching the force-displacement results of the healthy artery FE models with those of the tensile ring tests resulted in a mean (± standard error) hyperelastic shear modulus $\mu = 2004 \pm 410$ Pa and hardening exponent $\alpha = 22.8 \pm 2.2$ for the healthy arteries. These values were used in the wall (media plus adventitia) regions of the atherosclerotic models, and the mean values of the material properties for the plaque regions derived as $\mu = 2464 \pm 1075$ Pa and $\alpha = 38.3 \pm 6.7$. The mean arterial distensibility D_a of the healthy and atherosclerotic samples derived from the FE models are $1.12 \pm 0.11 \times 10^{-3}$ mmHg^{-1} and $0.87 \pm 0.18 \times 10^{-3}$ mmHg^{-1} respectively, indicating a trend for the healthy arteries to exhibit greater distensibility than the diseased arteries.

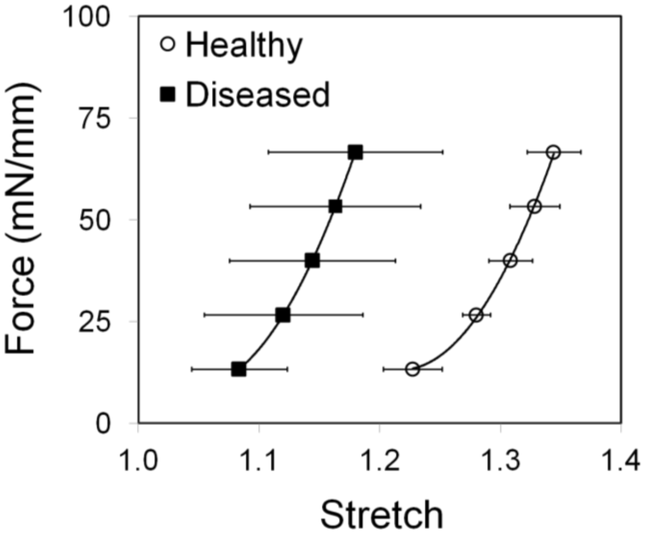

Figure 5.5 Force (per mm vessel length) vs. stretch (mean ± standard error) of the passive tensile ring tests of the healthy (n = 4) and atherosclerotic diseased (n = 6) arteries.

5.3.2 Finite element modelling of arterial endothelin-1 response

The results of the FE models of healthy and atherosclerotic arteries applied with pre-stretch forces and thermal loadings are shown in Figure 5.6. The optimum matching of the reaction forces between the ET-1 experiments and FE models resulted in thermal property parameters of the healthy artery model of $P_1 = -0.086$, $P_2 = 2.6 \times 10^7$ K^{-1}, and $P_3 = 0.34$, whereas those of the atherosclerotic artery model are $P_1 = -0.273$, $P_2 = 3.6 \times 10^7$ K^{-1}, and $P_3 = 0.20$. The negative values of P_1 for both models correspond to the contraction of artery rings in response to ET-1. The higher magnitude of P_1 required for the atherosclerotic artery model indicated that the maximum strain associated with the drug response was greater in the diseased than in the healthy arteries. This suggests that the smooth muscle cells of the atherosclerotic arteries have higher reactivity to ET-1 than those of the healthy arteries.

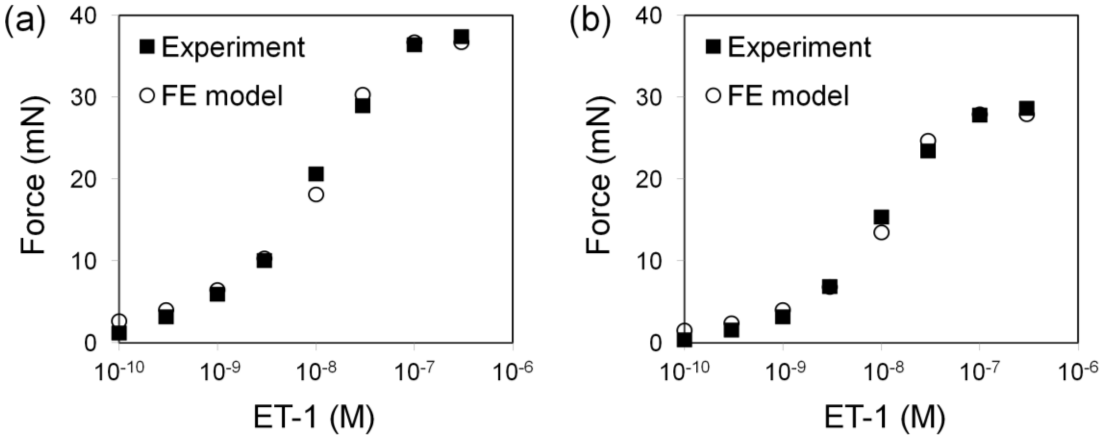

Figure 5.6 The matching of the reaction forces of endothelin-1 (ET-1) experiments and finite element (FE) models for the (a) healthy and (b) atherosclerotic arteries.

The distensibility D_a of these two models under the physiological condition with no contractile muscle tone (passive) and applying healthy or diseased muscle tones were determined from the modelling of the ET-1 response (Table 5.1). The atherosclerotic model has a lower D_a than the healthy model in the passive condition, as previously obtained in the modelling of the tensile ring tests. Applying the diseased muscle tone significantly increased D_a of the diseased model, which achieved a similar level as that of the healthy model with healthy muscle tone. The diseased muscle tone caused a reduction in the lumen area of the atherosclerotic model at 80 mmHg but an increase of the area at 120 mmHg, compared to those in passive and with healthy muscle tone. The larger change in lumen area in response to the pulse pressure and the normalisation to a smaller area resulted in the higher D_a of the model with diseased muscle tone.

Table 5.1 Arterial distensibility D_a of the healthy and atherosclerotic diseased models with no contractile muscle tone (passive) and applying healthy or diseased muscle tones determined from the modelling of the endothelin-1 response.

Artery	**D_a (mmHg^{-1})**		
	Passive	**Healthy tone**	**Diseased tone**
Healthy	1.10×10^{-3}	1.08×10^{-3}	-
Diseased	0.67×10^{-3}	0.67×10^{-3}	1.04×10^{-3}

5.4 Discussion

While hypothesising that the atherosclerosis-induced media smooth muscle atrophy would contribute to a marked loss of contractile response to ET-1, Dr. Maguire found that the atherosclerotic arteries maintained a maximum response of over 70% of that of healthy arteries (Figure 5.1a) and had a similar normalised response as the healthy arteries (Figure 5.1b) (Ooi et al. 2014). Mechanical tests and FE modelling were carried out to investigate the mechanisms of this unexpected finding. The passive mechanical properties of the healthy and atherosclerotic coronary arteries were determined, indicating that the diseased arteries are potentially stiffer (lower distensibility) than the healthy arteries, which agrees with the clinical observations in patients (van Popele et al. 2001, Wykretowicz et al. 2009). The non-significance of the differences may be due to the small sample sizes and high variation of the results. The values of the shear modulus μ of the arterial wall and plaque are very different from those reported in Chapter 4 (Table 4.1 and Figure 4.14). This is mainly due to the differences in the geometry baselines that were used to create the FE models and calculate the deformations. In this chapter, the passive mechanical tests were analysed based on the initial arterial geometries at the zero-load state in the histology. On the other hand, the mechanical tests in Chapter 4 were run with a pre-stretch to hold the artery rings and ensure that forces were clearly recorded at the beginning of the loading cycles, where this starting point was used as the baseline for the deformation analysis. This results in a shift of the stress-strain curves when compared to those in this chapter, leading to the different μ values where the conversion of μ to incremental elastic modulus depends on the strains.

Distensibility was chosen as the indicator of arterial stiffness due to its direct representation of the overall arterial compliance and close correlation with the volume of blood flow through the artery. Elastic modulus, which is commonly used as a representation of stiffness, varies across the plaque and arterial wall of a thick-wall atherosclerotic artery (Beattie et al. 1998, Holzapfel et al. 2004, Baldewsing et al. 2008) and is therefore not an appropriate indicator of the overall arterial compliance. In some *in vitro* studies, the measurements of the overall elastic modulus of atherosclerotic arteries led to a conclusion that the diseased artery is less stiff than the healthy artery (Koniari et al. 2011, Karimi et al. 2013), which is mainly due to the low-modulus lipid-dominated morphology of the plaques. This contradicts the clinical observations where the overall stiffness of the artery was determined from arterial distensibility or pulse wave velocity (van Popele et al. 2001, Wykretowicz et al. 2009). The selection of arterial distensibility as the stiffness indicator in this study is more physiologically relevant, and a similar conclusion as found in the clinical studies was obtained.

The mechanisms of the arterial responses to ET-1 were demonstrated using FE models, where the atherosclerotic arteries have similar or slightly lower reaction forces when compared to the healthy arteries. The maintained contractile ability of atherosclerotic arteries to ET-1 to a similar extent as healthy arteries, despite the loss of smooth muscle, may be a result of an increase of the reactivity of the remaining smooth muscle cells to ET-1, as indicated in the FE modelling where the P_1 parameter (thermal reactivity) was higher in the atherosclerotic than the healthy artery model. There may be an underestimate of the P_1 of the atherosclerotic model, since its media thickness was kept the same as that of the healthy model for ease of comparison, rather than reduced in the diseased model to reflect media atrophy as observed in the histology (Figure 5.1c). The magnitude of the contractile response P_1 for the atherosclerotic artery is predicted to be even higher if the media thickness of the atherosclerotic artery model were reduced while the force response was maintained.

Finally, the physiological distensibility results of the healthy and atherosclerotic models with muscle tones suggest that the diseased artery has an adaptation response which changes muscle reactivity to increase the arterial contraction in response to ET-1, resulting in a distensibility that is closer to that of the healthy artery. The mechanisms underlying this observation require further investigation.

5.5 Conclusion

The work described in this chapter has explored the maintained active response of human atherosclerotic artery to ET-1 *in vitro* despite extensive thinning of the media smooth muscle layer. While providing comparisons of the mechanical properties of the healthy and atherosclerotic arteries, the tensile tests and FE modelling demonstrated the potential elevated contractile strains developed by diseased smooth muscle cells in response to ET-1. These results suggest that adaptation mechanisms occur with the pathogenesis of atherosclerosis to maintain the distensibility of the diseased vessel wall in response to vasoconstrictors such as ET-1. This phenomenon provides an important insight for future development of new drug treatment strategies for atherosclerotic disease.

5.6 References

Abaqus Theory Manual, Section 4.6.1. *Abaqus 6.11 Documentation Collection*. Dassault Systèmes Simulia, Providence, USA.

Baldewsing RA, Danilouchkine MG, Mastik F, Schaar JA, Serruys PW, van der Steen AFW. An inverse method for imaging the local elasticity of atherosclerotic coronary plaques. *IEEE Trans Inf Technol Biomed*. 12(3):277-289, 2008.

Burke AP, Kolodgie FD, Farb A, Weber D, Virmani R. Morphological predictors of arterial remodeling in coronary atherosclerosis. *Circulation*. 105(3):297-303, 2002.

Beattie D, Xu G, Vito R, Glagov S, Whang WG. Mechanical analysis of heterogeneous, atherosclerotic human aorta. *J Biomech Eng*. 120(5):602-607, 1998.

Crisby M, Nordin-Fredriksson G, Shah PK, Yano J, Zhu J, Nilsson J. Pravastatin treatment increases collagen content and decreases lipid content, inflammation, metalloproteinases, and cell death in human carotid plaques: implications for plaque stabilization. *Circulation*. 103(7):926-933, 2001.

Hedblad B, Wikstrand J, Janzon L, Wedel H, Berglund G. Low-dose metoprolol CR/XL and fluvastatin slow progression of carotid intima-media thickness: main results from the Beta-Blocker Cholesterol-Lowering Asymptomatic Plaque Study (BCAPS). *Circulation*. 103(13):1721-1726, 2001.

Holzapfel GA and Ogden RW. Constitutive modelling of arteries. *Proc R Soc A*. 466:1551-1597, 2010.

Holzapfel GA, Sommer G, Regitnig P. Anisotropic mechanical properties of tissue components in human atherosclerotic plaques. *J Biomech Eng*. 126(5):657-665, 2004.

Karimi A, Navidbakhsh M, Shojaei A, Faghihi S. Measurement of the uniaxial mechanical properties of healthy and atherosclerotic human coronary arteries. *Mater Sci Eng C Mater Biol Appl*. 33(5):2550-2554, 2013.

Koniari I, Mavrilas D, Papadaki H, Karanikolas M, Mandellou M, Papalois A, Koletsis E, Dougenis D, Apostolakis E. Structural and biomechanical alterations in rabbit thoracic aortas are associated with the progression of atherosclerosis. *Lipids Health Dis*. 10:125, 2011.

Martín-Ventura JL, Blanco-Colio LM, Gómez-Hernández A, Muñoz-García B, Vega M, Serrano J, Ortega L, Hernández G, Tuñón J, Egido J. Intensive treatment with atorvastatin reduces inflammation in mononuclear cells and human atherosclerotic lesions in one month. *Stroke*. 36(8):1796-1800, 2005.

Nissen SE, Tuzcu EM, Libby P, Thompson PD, Ghali M, Garza D, Berman L, Shi H, Buebendorf E, Topol EJ; CAMELOT investigators. Effect of antihypertensive agents on cardiovascular events in patients with coronary disease and normal blood pressure: the CAMELOT study: a randomized controlled trial. *JAMA*. 292(18):2217-2225, 2004.

Nissen SE, Tuzcu EM, Schoenhagen P, Crowe T, Sasiela WJ, Tsai J, Orazem J, Magorien RD, O'Shaughnessy C, Ganz P; Reversal of Atherosclerosis with Aggressive Lipid Lowering (REVERSAL) investigators. Statin therapy, LDL cholesterol, C-reactive protein, and coronary artery disease. *N Engl J Med*. 352(1):29-38, 2005.

Ooi CY, Sutcliffe MP, Davenport AP, Maguire JJ. Changes in biomechanical properties of the coronary artery wall contribute to maintained contractile responses to endothelin-1 in atherosclerosis. *Life Sci*. In Press, 2014.

van Popele NM, Grobbee DE, Bots ML, Asmar R, Topouchian J, Reneman RS, Hoeks APG, van der Kuip DAM, Hofman A, Witteman JCM. Association between arterial stiffness and atherosclerosis: the Rotterdam Study. *Stroke*. 32(2):454-460, 2001.

Wiklund O, Hulthe J, Wikstrand J, Schmidt C, Olofsson SO, Bondjers G. Effect of controlled release/extended release metoprolol on carotid intima-media thickness in patients with hypercholesterolemia: a 3-year randomized study. *Stroke*. 33(2):572-577, 2001.

Wykretowicz A, Gerstenberger P, Guzik P, Milewska A, Krauze T, Adamska K, Rutkowska A, Wysocki H. Arterial stiffness in relation to subclinical atherosclerosis. *Eur J Clin Invest*. 39(1):11-16, 2009.

Yang J, Clark JW Jr, Bryan RM, Robertson C. The myogenic response in isolated rat cerebrovascular arteries: smooth muscle cell model. *Med Eng Phys.* 25(8):691-709, 2003.

Zulliger MA, Rachev A, Stergiopulos N. A constitutive formulation of arterial mechanics including vascular smooth muscle tone. *Am J Physiol Heart Circ Physiol.* 287(3):H1335-H1343, 2004.

Zanchetti A, Bond MG, Hennig M, Neiss A, Mancia G, Dal Palù C, Hansson L, Magnani B, Rahn KH, Reid JL, Rodicio J, Safar M, Eckes L, Rizzini P; European Lacidipine Study on Atherosclerosis investigators. Calcium antagonist lacidipine slows down progression of asymptomatic carotid atherosclerosis: principal results of the European Lacidipine Study on Atherosclerosis (ELSA), a randomized, double-blind, long-term trial. *Circulation*. 106(19):2422-2427, 2002.

6. The Role of Hyaluronan in Systemic Inflammation-Induced Aortic Stiffening

6.1 Introduction

Patients with systemic inflammatory conditions such as rheumatoid arthritis have increased cardiovascular risk due to aortic stiffening (Van Doornum et al. 2003, Booth et al. 2004, Mäki-Petäjä et al. 2006 and 2012). In the studies of Mäki-Petäjä *et al.* (2006, 2012), rheumatoid arthritis has shown to increase aortic stiffness which can be reversed by anti-inflammatory agents. However, the mechanism of how inflammation leads to this aortic stiffening remains unclear. The capability of reversing the aortic stiffness with anti-inflammatory drugs suggests that the inflammation-induced aortic stiffening is not caused by the loss of elastin fibres, since the aortic elastin fibres are only synthesised during the gestational period and the first year of life (Martyn and Greenwald 1997) thus cannot be repaired or reproduced later on. In addition, some preliminary data of Dr. Mäki-Petäjä show that endothelial dysfunction does not modulate the aortic stiffness, suggesting that the inflammation-induced aortic stiffening is not directly related to the changes of endothelial or smooth muscle functions.

Therefore, a potential mechanism of this aortic stiffening is inflammation changing the properties of arterial extracellular matrix (ECM) such as proteoglycan proteins or glycosaminoglycan (GAG) chains that attach to them. The inflammatory cell infiltration in the media layer may lead to arterial stiffening by changing the amount and nature of proteoglycans, thus altering the state of hydration of the artery. The amount of GAGs such as hyaluronan, aggrecan, and versican in the aorta has also been shown to increase with inflammation (Kaji et al. 1993). More specifically, rheumatoid arthritis and some vascular diseases show altered metabolism, distribution, and function of hyaluronan (Toole et al. 2002). In general, hyaluronan in the artery traps water, which promotes resistance to compressive loads and enhances arterial stiffness (Toole et al. 2002), thus overproduction of this component may lead to arterial stiffening.

It is hypothesised that hyaluronan plays an important role on regulating the stiffness of artery, which is responsible for systemic inflammation-induced aortic stiffening and vascular diseases. This hypothesis is tested by mechanical testing on rat arteries that have hyaluronan degraded by hyaluronidase, and comparing their mechanical properties to those of the arteries without treatment.

6.2 Methods

Aortas of 17 Sprague-Dawley rats aged six to seven weeks were collected by Dr. Mäki-Petäjä in Clinical Pharmacology Unit with ethical approval. Each of the arteries was separated into two sections; one was incubated in hyaluronidase and another in saline solution for an hour. Ten of the aortas were used for mechanical test (n = 10 for each group), which were frozen and tested within a week. The remaining aortas were tested with enzyme-linked immunosorbent assays (ELISA) on hyaluronan content immediately after the hyaluronidase or saline incubation.

For the mechanical test, the rat aortas were defrosted in phosphate buffered saline (PBS) solution. An arterial ring was harvested from the middle section of each artery and mounted onto two tungsten wire probes with the tensile test setup in Section 4.2.1. Five loading cycles of 0.08 N were applied at a frequency of 0.025 Hz and the last cycle was used for the analysis. Videos were taken during loading using a camera (PixeLINK, Ottawa, Canada) connected to a stereo microscope at a frame rate of 4 fps. The arterial ring was immersed in PBS solution throughout the test.

The overall stretch λ of the artery at each deformation step was calculated as the deformed outer circumference C divided by the initial circumference C_{init}

$$\lambda = \frac{C}{C_{\text{init}}} \tag{6.1}$$

The logarithmic strain ε was then calculated as the natural logarithm of the stretch.

$$\varepsilon = \ln \lambda \tag{6.2}$$

In order to obtain the cross-sectional area of the ring wall, the overall wall thickness t was determined as $t = r_o - r_i$, where r_o and r_i are the outer and inner radii of the ring (Figure 6.1). Assuming circular geometry, these radii were estimated from the measured inner and outer areas of the ring, πr_i^2 and πr_o^2. The harvested length h of the ring was determined from images captured from the sides of the ring, taking the average of the lengths measured at six points. From these, the cross-sectional area A of the ring wall was calculated as $A = t \times h$. The Cauchy stress σ that corresponds to the reaction force F of the arterial ring was then determined as:

$$\sigma = \frac{F}{2A} \times \lambda \tag{6.3}$$

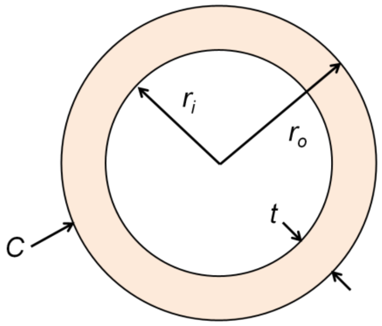

Figure 6.1 Schematic diagram of a circular arterial ring with labelled outer circumference C, outer and inner radii r_o and r_i, and wall thickness t.

The comparison between the arterial stiffness of the hyaluronidase-treated and control groups were made by examining the elastic modulus E between the physiological pressures of 80 to 120 mmHg, which was calculated using Equation (6.4), where σ_{80}, σ_{120}, ε_{80}, and ε_{120} are the stresses and strains at 80 and 120 mmHg, respectively.

$$E = \frac{\sigma_{120} - \sigma_{80}}{\varepsilon_{120} - \varepsilon_{80}} \tag{6.4}$$

The stresses and strains at these pressures were determined using the principle of force equilibrium on the arterial wall. As shown in Figure 6.2a, the reaction force F_p that corresponds to a specific pressure P can be calculated as

$$F_p = P \times 2r_i \times h \tag{6.5}$$

Assuming the inner circumference of the arterial ring equals twice the lumen length L during the tensile deformation ($2\pi r_i = 2L$, Figure 6.2b), Equation (6.5) can be written as

$$F_p = \frac{2PLh}{\pi} \tag{6.6}$$

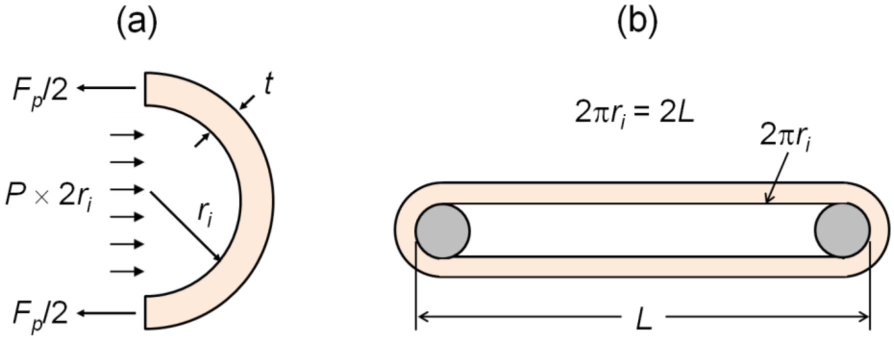

Figure 6.2 (a) Equilibrium of forces F_p that correspond to the pressure P applied on the arterial wall; r_i and t are the inner radius and wall thickness of the artery. (b) The equivalence of the arterial inner circumference ($2\pi r_i$) with twice of the lumen length L in a tensile ring deformation.

The intersection point of the curve of F_p with the arterial reaction forces in the force vs. lumen length plots (Figure 6.3) was determined as the point that corresponds to the specific pressure in the physiological pressurisation condition. Having the value of a specific F_p, the strain that corresponds to this pressure load can be determined from the force-strain curve, and the corresponded stress can then be determined from the stress-strain curve.

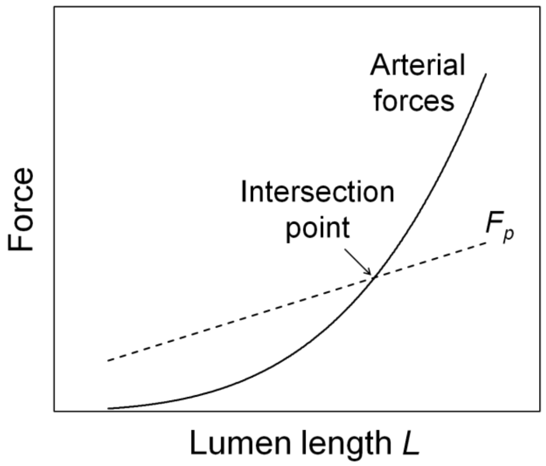

Figure 6.3 Determining the value of the force that corresponds to an internal pressure in the physiological condition as the intersection point of the arterial reaction forces with the curve of the associated pressure force F_p determined using the principle of force equilibrium.

For the separate groups of rat aortas, the hyaluronan content in each artery was quantified using ELISA performed by Dr. Mäki-Petäjä. The results were then correlated with the calculated E.

6.3 Results

The outer diameter and wall thickness of the rat aortic rings are not significantly different between the hyaluronidase-treated and control groups, with a mean (± standard error) diameter of 1.70 ± 0.03 and 1.67 ± 0.03 mm ($p = 0.45$ by ANOVA), and mean wall thickness of 0.15 ± 0.002 and 0.15 ± 0.001 mm ($p = 0.60$), respectively. The images recorded during one of these tests are presented in Figure 6.4, showing the initial and deformed states of an aortic ring. The stress-strain relationship of the artery is shown in Figure 6.5, indicating the points that correspond to the physiological pressures of 80 and 120 mmHg. The elastic modulus E of the hyaluronidase-treated and control arteries are 2057 ± 118 and 1992 ± 79 kPa, respectively, which are not significantly different between two groups ($p = 0.65$). In the ELISA tests, the hyaluronidase successfully digested the hyaluronan of the treated arteries to 0 ± 0 μg per gram of aortic tissue compared to that of the control group of 22 ± 6 μg ($p = 0.02$).

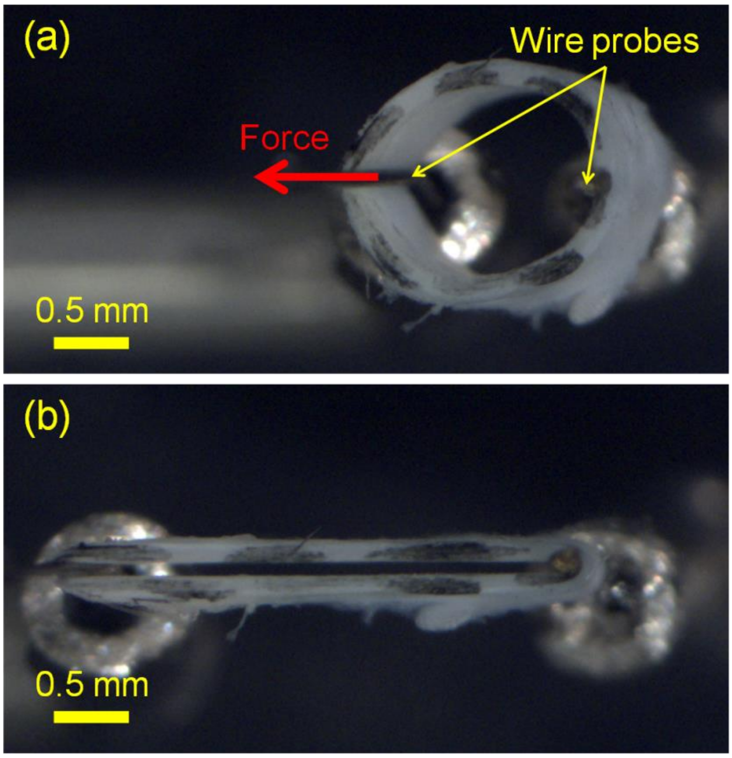

Figure 6.4 (a) The initial and (b) deformed states of a rat aortic ring with a horizontal tensile loading. Black markers were applied on the artery to increase the contrast of the cross-section.

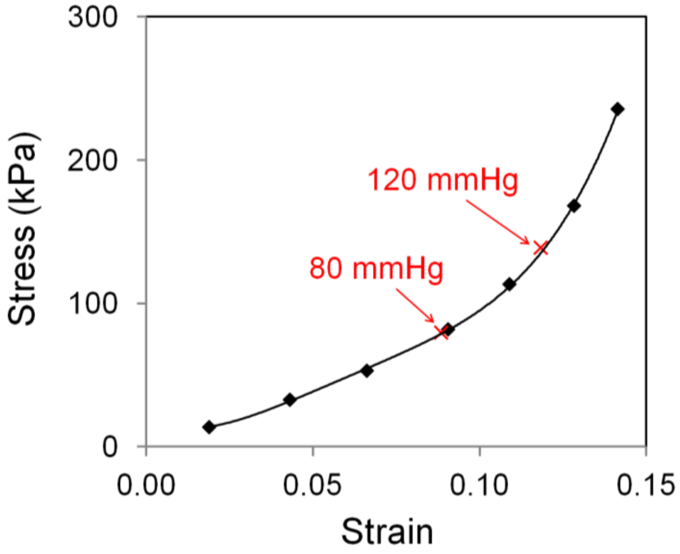

Figure 6.5 The stress-strain relationship of a sample rat aorta, showing the points that correspond to the internal pressures of 80 and 120 mmHg.

6.4 Discussion and Conclusion

The physiological elastic modulus of the hyaluronidase-treated and control arteries are not significantly different despite the successful digestion of the arterial hyaluronan by hyaluronidase, which is in contradiction with the hypothesis. On the other hand, preliminary studies of Dr. Mäki-Petäjä demonstrated that hyaluronan content in blood is higher in patients with rheumatoid arthritis compared to the control subjects, which could be associated with aortic stiffening (increased pulse wave velocity) in these patients.

One potential mechanism explaining this contradiction is that the disease-induced hyaluronan accumulation leads to collagen constriction (Travis et al. 2001) and elastin fragmentation (Chai et al. 2005), resulting in arterial stiffening. Chai *et al.* (2005) suggests that the elastin fragmentation is more likely to contribute to the aortic stiffening by changing the collagen orientation rather than directly influencing the mechanical stiffness. This contradicts the initial speculation of this study that inflammation-induced aortic stiffening is not caused by the loss of elastin fibres due to the capability of reversing the aortic stiffness with anti-inflammatory drugs (Mäki-Petäjä et al. 2006 and 2012) while aortic elastin fibres are not produced after the first year of life (Martyn and Greenwald 1997). Therefore, further investigations are required on the correlation between the changes of elastin and collagen structures during the progression of the inflammatory disease and the recovery of the aortic stiffness with anti-inflammatory drugs. Nevertheless, these long term effects of the change of hyaluronan content are not generated with the methodology of this study, thus a future study can be performed on a transgenic animal model with accumulated or deficit hyaluronan in arteries to confirm this hypothesis.

In conclusion, this study demonstrated the capability of performing tensile ring tests on rat aortas and correlating their elastic modulus with the results of biochemical assays. The results suggest that the hyaluronan content alone does not contribute to the arterial stiffening in diseases involving systemic inflammation such as rheumatoid arthritis. It could be either other ECM proteins or the coupling of the hyaluronan with these proteins that lead to the change of arterial stiffness.

6.5 References

Booth AD, Wallace S, McEniery CM, Yasmin, Brown J, Jayne DR, Wilkinson IB. Inflammation and arterial stiffness in systemic vasculitis: a model of vascular inflammation. *Arthritis Rheum*. 50(2):581-588, 2004.

Chai S, Chai Q, Danielsen CC, Hjorth P, Nyengaard JR, Ledet T, Yamaguchi Y, Rasmussen LM, Wogensen L. Overexpression of hyaluronan in the tunica media promotes the development of atherosclerosis. *Circ Res*. 96(5):583-591, 2005.

Kaji T, Hiraga S, Yamamoto C, Sakamoto M, Nakashima Y, Sueishi K, Koizumi F. Tumor necrosis factor alpha-induced alteration of glycosaminoglycans in cultured vascular smooth-muscle cells. *Biochim Biophys Acta*. 1176(1-2):20-26, 1993.

Mäki-Petäjä KM, Elkhawad M, Cheriyan J, Joshi FR, Ostör AJ, Hall FC, Rudd JH, Wilkinson IB. Anti-tumor necrosis factor-α therapy reduces aortic inflammation and stiffness in patients with rheumatoid arthritis. *Circulation*. 126(21):2473-2480, 2012.

Mäki-Petäjä KM, Hall FC, Booth AD, Wallace SM, Yasmin, Bearcroft PW, Harish S, Furlong A, McEniery CM, Brown J, Wilkinson IB. Rheumatoid arthritis is associated with increased aortic pulse-wave velocity, which is reduced by anti-tumor necrosis factor-alpha therapy. *Circulation*. 114(11):1185-1192, 2006.

Martyn CN and Greenwald SE. Impaired synthesis of elastin in walls of aorta and large conduit arteries during early development as an initiating event in pathogenesis of systemic hypertension. *Lancet*. 350(9082):953-955, 1997.

Toole BP, Wight TN, Tammi MI. Hyaluronan-cell interactions in cancer and vascular disease. *J Biol Chem*. 277(7):4593-4596, 2002.

Travis JA, Hughes MG, Wong JM, Wagner WD, Geary RL. Hyaluronan enhances contraction of collagen by smooth muscle cells and adventitial fibroblasts: role of CD44 and implications for constrictive remodeling. *Circ Res*. 88(1):77-83, 2001.

Van Doornum S, McColl G, Jenkins A, Green DJ, Wicks IP. Screening for atherosclerosis in patients with rheumatoid arthritis: comparison of two in vivo tests of vascular function. *Arthritis Rheum*. 48(1):72-80, 2003.

7. A Novel Inflation Test Technique for *In Vitro* Determination of the Cross-Sectional Deformation of Artery

7.1 Introduction

Arterial stiffness is an important indicator of cardiovascular risks, which leads to ventricular hypertrophy and potential heart failure (Mitchell 1999). As described in Chapter 4, the determination of the cross-sectional mechanical properties of artery is crucial for correlating the regional arterial stiffness with the biological components of the atherosclerotic artery. In addition to this diseased condition, it is also important in the case of ageing-induced arterial stiffening (Mitchell et al. 2004, McEniery et al. 2005) to correlate the changes of arterial biological components, such as increasing activity of matrix metalloproteinases (MMPs) (Yasmin et al. 2005 and 2006), arterial calcification (McEniery et al. 2009, Ng et al. 2011), and elastin fragmentation (Fonck et al. 2009, Tsamis et al. 2013), with the arterial stiffness.

As demonstrated in Chapter 4, the combination of a tensile ring test and optical flow estimation can be used to determine the cross-sectional mechanical properties of the artery. However, this approach has a limitation of non-physiological tensile loading on the arterial ring, which results in difficulties in determining the mechanical loads that correspond to the internal physiological pressures as well as inaccurate results at both loading ends. While applying internal pressures on a section of artery is preferable to mimic the physiological condition, it often requires mounting of both ends of the artery onto two cannulae for the fluid pressurisation, which limits the imaging of the arterial cross-section. In this case, ultrasound imaging can be used to determine the cross-sectional deformation as in the study of Baldewsing *et al.* (2004), but the accuracy of the measurements is limited due to non-direct imaging on the arterial cross-section. Beattie *et al.* (1998) have performed an inflation test on artery rings using a latex tube. While providing a direct imaging of the arterial cross-section, the significantly higher stiffness of the latex tube compared to the artery would raise a concern on the accuracy of the calibrated pressures. The consistency of the measurements of arterial cross-section captured from the top may also be influenced by the changes of the tissue bath level during inflation due to the changes of light refraction.

In this chapter, a novel inflation test technique has been designed and validated, which allows direct imaging of the cross-sectional deformation of an artery ring in an *in vitro* pressurisation test, as in the study of Beattie *et al.* (1998) but solves the limitations discussed above. Combining with optical flow analysis, this design enables the determination of both the overall and regional mechanical properties of an artery, and thus can be used in future studies on diseased or ageing-induced changes of regional arterial stiffness.

7.2 Methods

7.2.1 Design of inflation test system

An inflation test system has been designed as shown in Figure 7.1a. A syringe pump is used to inject water through silicon tubes to a balloon tube, where the inflation of the balloon loads an artery ring with an internal pressure. A common latex rocket balloon (Creative Party Ltd, Bournemouth, UK) with 11 mm diameter has been chosen for the testing of the design, where it is aimed to use multiple custom-build latex tubes with a variety of diameters and stiffness for different arteries in future studies. The cyclic pressure loading is controlled by Labview programme (National Instruments, Austin, USA), with the pressures recorded by a pressure transducer (Honeywell S&C, Morristown, USA) connected to a data logger (National Instruments, Austin, USA). The cross-sectional deformation of the artery is captured using a camera (PixeLINK, Ottawa, Canada).

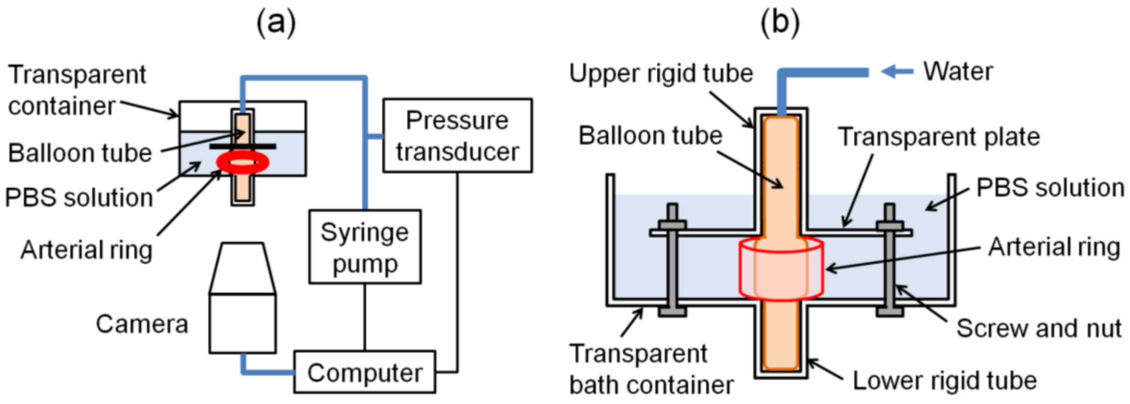

Figure 7.1 (a) The setup of the inflation artery ring test and (b) the enlarged view of the inflation system.

A transparent plastic container is used to immerse the artery in phosphate buffered saline *(*PBS) solution, which allows the capture of the arterial deformation through the bottom of the container (Figure 7.1b). A rigid plastic tube was separated into two sections, one connected to the bath container and another to a transparent plastic plate. These rigid tube sections are used to cover the balloon and allow it to be inflated only at the opening between the upper and lower sections of the tube. The size of this opening is adjustable using the screws and nuts that connect the plastic plate with the bath container, so that the inflatable section of the balloon has a length that is the same as that of the arterial ring. An inverted imaging system is designed since the level of the PBS solution changes with the inflation of balloon, which influences the accuracy of the images taken from the top.

7.2.2 Testing with pig aorta

In order to assess the capability of the inflation test system for obtaining arterial mechanical properties in a physiological pressure range, an experiment was carried out on a pig aorta collected from an abattoir (Leech & Sons, Melbourn, UK). An artery ring was harvested from the aorta and placed on the balloon tube. Some dot markers were applied on the ring using water resistant ink to increase the accuracy of deformation analysis. Five pressure cycles of 0 to 400 mmHg were applied at a frequency of 0.02 Hz and the artery deformation was recorded at a frame rate of 4 fps.

The first four cycles were used to precondition the ring and the last cycle was used for data analysis.

After that, the arterial ring was removed and another pressurisation was performed on only the balloon. The same fluid volume as the arterial inflation test was injected into the balloon by applying the same syringe pump displacement at the same frequency. The pressures that were applied on the arterial ring were then calibrated by subtracting the pressure on only the balloon (second test) from that on both balloon and artery (first test) at the same time point.

7.2.3 Analysing arterial deformation

The deformation of the arterial ring in the inflation test was then analysed. Assuming circular geometry, the inner and outer radii, r_i and r_o, of the ring were estimated from the measured inner and outer areas of the ring, $\pi {r_i}^2$ and $\pi {r_o}^2$. These radii were then used to calculate the mid-wall circumferential stretch λ_m and logarithmic strain ε_m using the equations below, where r_m and $r_{m,\mathrm{init}}$ are the deformed and initial mid-wall radii, respectively.

$$r_m = \frac{r_i + r_o}{2} \tag{7.1}$$

$$\lambda_m = \frac{r_m}{r_{m,\mathrm{init}}} \tag{7.2}$$

$$\varepsilon_m = \ln \lambda_m \tag{7.3}$$

The circumferential stresses σ applied on the artery were then calculated from the calibrated pressures P using the thin-wall tube equation.

$$\sigma = \frac{P \times r_m}{r_o - r_i} \tag{7.4}$$

The calculated stresses and strains were then used to determine the elastic modulus *E* at the physiological pressure range of 80 – 120 mmHg, where σ_{80}, σ_{120}, ε_{80}, and ε_{120} are the mid-wall stresses and strains at 80 and 120 mmHg, respectively.

$$E = \frac{\sigma_{120} - \sigma_{80}}{\varepsilon_{120} - \varepsilon_{80}} \tag{7.5}$$

In order to determine the variation of strains at the cross-section of the arterial ring, optical flow estimation was performed on the deformation images as described in Chapter 3. The optimum smoothing parameters for the inflation test determined in Chapter 3 were used in this analysis.

7.2.4 Validating the inflation test with tensile test

A tensile test was carried out to compare the results with those of the inflation test. An arterial ring was harvested from the aortic section adjacent to the ring used for the inflation test, and tested with uniaxial tensile loading as described in Chapters 4 and 6. Five displacement cycles of 13 mm were applied at a frequency of 0.02 Hz and the last cycle was used for the analysis. The arterial deformation and reaction forces were recorded as in the inflation test. The deformation was then analysed as in Chapter 6 to obtain the stress-strain relationship and *E* at 80 – 120 mmHg.

7.3 Results

7.3.1 Inflation test

The initial and deformed geometries of the pig aortic ring in the inflation test are shown in Figure 7.2. The pressures that were applied on the arterial ring with the balloon and those on the balloon alone are presented in Figure 7.3, along with the calibrated pressures applied on the arterial ring. The calculated stress-strain curve is shown in Figure 7.4, with the points that correspond to the physiological pressures of 80 and 120 mmHg labelled. The elastic modulus *E* determined using the stresses and strains at these pressures is 469 kPa. The cross-sectional strains determined using optical flow analysis range from 0.1 to 0.7 (Figure 7.5a) at the final calibrated pressure of 260 mmHg, with the majority of them falling in the range of 0.3 to 0.4 (Figure 7.5b).

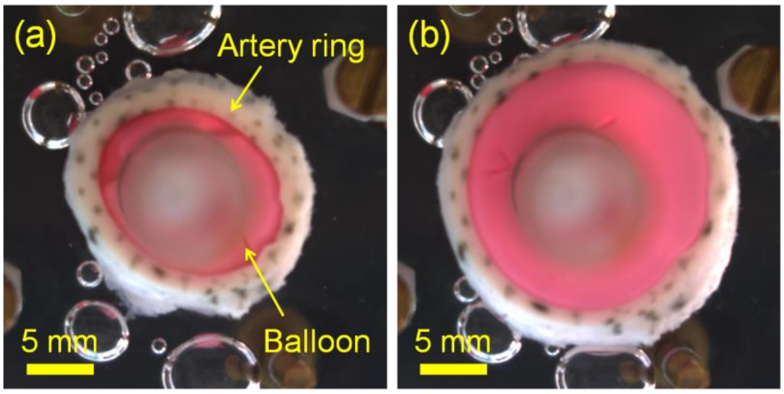

Figure 7.2 (a) Initial and (b) deformed geometries of the pig aortic ring with an internal pressure loading of 400 mmHg.

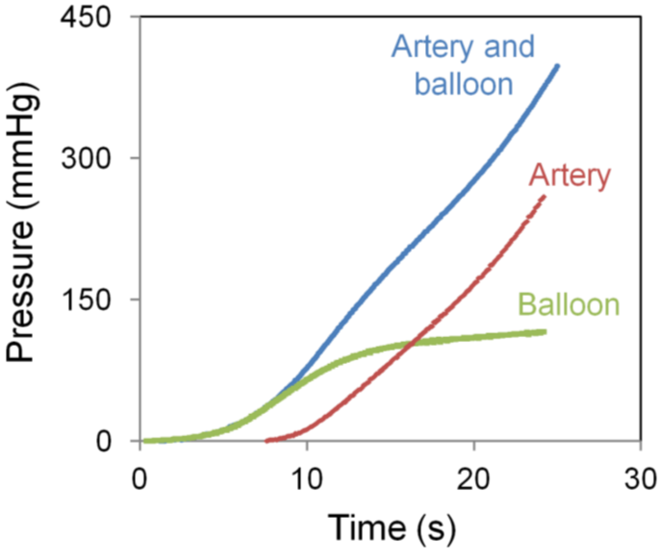

Figure 7.3 The applied pressure as a function of loading time for artery with balloon, only the balloon, and only the artery. The loading time is proportional to the volume of water injected into the balloon.

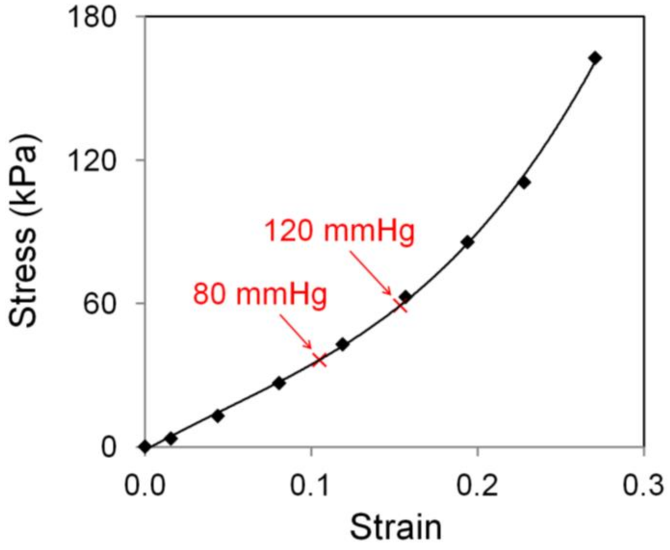

Figure 7.4 The stress-strain curve of the artery inflation test with labelled points at the physiological pressures of 80 and 120 mmHg.

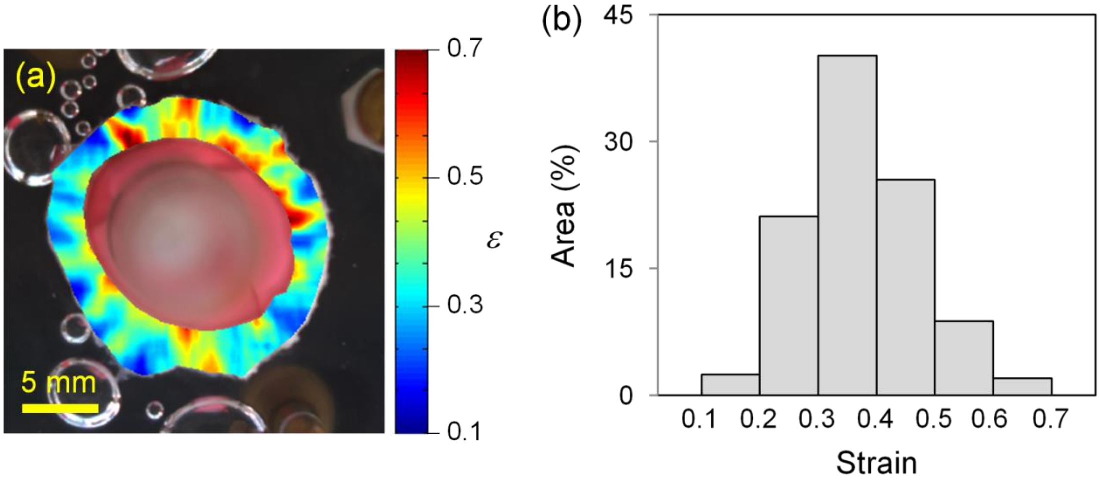

Figure 7.5 (a) Circumferential strains ε determined using optical flow analysis. (b) Percent of the area of arterial cross-section in each range of strains.

7.3.2 Tensile test

The initial and deformed geometries of the pig aorta with tensile loading are shown in Figure 7.6. The stress-strain curve of this test is shown in Figure 7.7, along with that of the inflation test. The calculated *E* at the pressure range of 80 – 120 mmHg is 494 kPa for this tensile test.

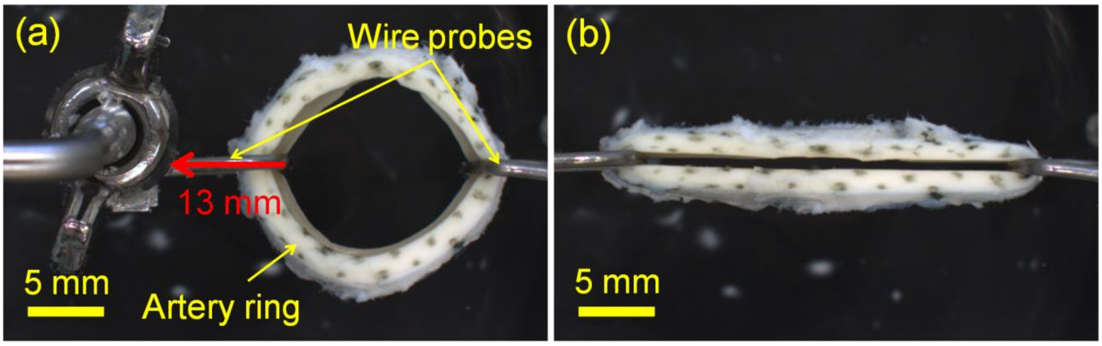

Figure 7.6 (a) Initial and (b) deformed geometries of the pig aortic ring with a horizontal tensile loading.

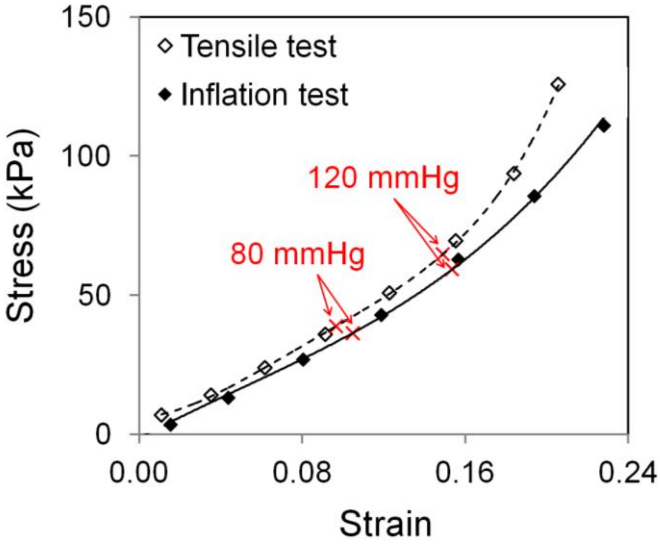

Figure 7.7 The stress-strain curves of the artery tensile and inflation tests with labelled points of the physiological pressures 80 and 120 mmHg.

7.4 Discussion and Conclusion

The design of an inflation test system for *in vitro* mechanical test of an artery ring has been demonstrated. From the preliminary experiments on pig aortic rings, the incremental elastic modulus of 469 and 494 kPa have been obtained for the inflation and tensile tests, respectively, for the pressure range that corresponds to a physiological environment. The difference between these two values is 5% which is considered acceptable consistency. This validates the capability of the inflation test design to determine the overall stiffness of an artery loaded with physiological pressures. During the inflation, the axial shortening of the arterial ring caused reducing resistance of the balloon expansion at both ends of the ring, leading to a tendency of larger deformation at the recorded arterial site than the actual overall deformation. This resulted in the discrepancy between the stress-strain curves of the inflation and tensile tests at high strains (Figure 7.7) and suggests that the result of the inflation test at high strains may not be as reliable as that in the physiological pressure range. This effect could be reduced by using a stiffer balloon, but this raises a concern on the accuracy of the extracted arterial properties if the balloon is much stiffer than the artery.

While optical flow estimation has been used to determine the regional deformation of the artery ring, the strain fields of the artery do not seem physiologically realistic (Figure 7.5a). It is speculated that friction between the balloon and artery caused non-uniform deformations around the arterial circumference. Future improvements on the technique are needed to obtain more accurate regional deformation, such as using a non-frictional balloon or other expandable materials or applying grease to reduce the friction. Another limitation of this design is that the sizes of the balloon and plastic tube are only suitable for limited types of artery such as human and pig aortas. While balloon and tube of other sizes can be fitted to the system, challenges would arise when dealing with very small artery or diseased artery with seriously occluded lumen where an appropriate small size balloon is difficult to be obtained. In these cases, tensile ring test or ultrasound imaging would be better compromise approaches to determine the arterial cross-sectional mechanical properties.

In future studies, a finite element model can be used to correlate the deformations between each experiment sample and the model using the methodology described in Chapter 4 to determine the regional stiffness of the artery. Combined with histological observation of arterial cross-section, this allows a study of the associations of ageing-induced arterial stiffening with regional structural changes such as calcium deposition and elastin fragmentation.

7.5 References

Baldewsing RA, de Korte CL, Schaar JA, Mastik F, van der Steen AFW. A finite element model for performing intravascular ultrasound elastography of human atherosclerotic coronary arteries. *Ultrasound Med Biol*. 30(6):803-813, 2004.

Beattie D, Xu G, Vito R, Glagov S, Whang WG. Mechanical analysis of heterogeneous, atherosclerotic human aorta. *J Biomech Eng*. 120(5):602-607, 1998.

Fonck E, Feigl GG, Fasel J, Sage D, Unser M, Rüfenacht DA, Stergiopulos N. Effect of aging on elastin functionality in human cerebral arteries. *Stroke*. 40(7):2552-2556, 2009.

McEniery CM, McDonnell BJ, So A, Aitken S, Bolton CE, Munnery M, Hickson SS, Yasmin, Maki-Petaja KM, Cockcroft JR, Dixon AK, Wilkinson IB, Anglo-Cardiff Collaboration Trial Investigators. Aortic calcification is associated with aortic stiffness and isolated systolic hypertension in healthy individuals. *Hypertension*. 53(3):524-531, 2009.

McEniery CM, Yasmin, Hall IR, Qasem A, Wilkinson IB, Cockcroft JR, ACCT Investigators. Normal vascular aging: differential effects on wave reflection and aortic pulse wave velocity: the Anglo-Cardiff Collaborative Trial (ACCT). *J Am Coll Cardiol*. 46(9):1753-1760, 2005.

Mitchell GF. Pulse pressure, arterial compliance and cardiovascular morbidity and mortality. *Curr Opin Nephrol Hypertens*. 8(3):335-342, 1999.

Mitchell GF, Parise H, Benjamin EJ, Larson MG, Keyes MJ, Vita JA, Vasan RS, Levy D. Changes in arterial stiffness and wave reflection with advancing age in healthy men and women: the Framingham Heart Study. *Hypertension*. 43(6):1239-1245, 2004.

Ng K, Hildreth CM, Phillips JK, Avolio AP. Aortic stiffness is associated with vascular calcification and remodeling in a chronic kidney disease rat model. *Am J Physiol Renal Physiol*. 300(6):F1431-F1436, 2011.

Tsamis A, Krawiec JT, Vorp DA. Elastin and collagen fibre microstructure of the human aorta in ageing and disease: a review. *J R Soc Interface*. 10(83):20121004, 2013.

Yasmin, McEniery CM, O'Shaughnessy KM, Harnett P, Arshad A, Wallace S, Maki-Petaja K, McDonnell B, Ashby MJ, Brown J, Cockcroft JR, Wilkinson IB. Variation in the human matrix metalloproteinase-9 gene is associated with arterial stiffness in healthy individuals. *Arterioscler Thromb Vasc Biol*. 26(8):1799-1805, 2006.

Yasmin, McEniery CM, Wallace S, Dakham Z, Pulsalkar P, Maki-Petaja K, Ashby MJ, Cockcroft JR, Wilkinson IB. Matrix metalloproteinase-9 (MMP-9), MMP-2, and serum elastase activity are associated with systolic hypertension and arterial stiffness. *Arterioscler Thromb Vasc Biol*. 25(2):372, 2005.

8. Conclusion and Future Work

8.1 Conclusion

In-depth knowledge of the mechanical properties of artery is essential to develop efficient treatment strategies for cardiovascular diseases. This thesis developed improved techniques for investigating the passive and active mechanical properties of atherosclerotic artery. The correlation between hyaluronan content with arterial stiffness was also studied with mechanical tests. The conclusions of these studies are outlined below.

1. The application of the optical flow estimation technique in biomechanics experiments was first assessed. Finite element (FE) models representing tensile tests of square tissue and atherosclerotic artery and an inflation test of normal artery were developed. The images showing the deformation of the structure in each of these cases were constructed and analysed with the optical flow technique, with influences of the smoothness parameters and the number of analysis steps taken into consideration. These optical flow analyses provide good estimates of the strains for all of these deformation cases, suggesting that it can be an alternative approach to digital image correlation or other image analysis methods for experimental studies on arterial biomechanics.

2. Having developed the confidence to use the optical flow technique in the experiments, it was then combined with tensile ring tests and FE modelling to determine the heterogeneous mechanical properties of human atherosclerotic coronary arteries. The experimental images were first analysed using the optical flow technique to obtain local deformation strains; FE models with loading conditions mimicking the tests were then developed. The matching of the experimental and FE results were performed with optimisation of the FE material parameters by minimising the differences between the results. This provides a sensible estimate of the hyperelastic properties of both the arterial wall and plaque.

3. The active function of the atherosclerotic arteries was investigated with tensile ring tests and FE approaches. This study explored the maintained active response of human atherosclerotic artery to endothelin-1 (ET-1) *in vitro* despite extensive thinning of the media smooth muscle layer. The matching of the experiments and FE results demonstrated the potential elevated contractile strains developed by diseased smooth muscle cells in response to ET-1. The modelling of the arterial active function in the physiological condition further suggests that adaptation mechanisms occur in the atherosclerotic arteries to maintain the distensibility while being exposed to *in vivo* vasoactive agents.

4. A study on the role of hyaluronan in systemic inflammation-induced aortic stiffening has been performed with tensile tests on rat aortic rings and biochemical assays. The results show no significant difference between the elastic modulus of the hyaluronidase-treated and control arteries despite successful digestion of hyaluronan in the hyaluronidase-treated group. This contradicts the hypothesis that hyaluronan plays an important role on regulating the stiffness of artery, and suggests that the aortic stiffening may not be the contribution of the hyaluronan content alone but a result of changes of the coupling of hyaluronan with other extracellular matrix (ECM) proteins, which is a long term effect in patients.

5. The determination of arterial mechanical properties with a tensile ring test has limitations of non-physiological tensile loading and inaccurate results at the loading ends. In order to avoid these limitations, an inflation test system has been designed and shown to successfully obtain the overall elastic modulus of a pig aorta, which is consistent with that obtained from a tensile ring test. However, improvements are needed for determining the local mechanical properties of the artery and for the testing of small artery or diseased artery with occluded lumen.

Overall, this thesis provides information for further understanding the atherosclerosis-induced changes of arterial biomechanics and the association of hyaluronan content with aortic stiffening, which is useful for future development of treatment strategies for these diseases.

8.2 Future Work

The experimental and computational approaches demonstrated in this thesis can be used in future studies on arterial biomechanics. For the study on the mechanical properties of atherosclerotic artery, future work can be done for experiments involving pharmacological drugs to stimulate vascular smooth muscle response. The approach described in Chapter 4 can be used to determine the changes of the local mechanical properties of atherosclerotic arteries with these drugs and the differences between the responses of the healthy and diseased arteries. The results obtained *in vitro* can also be compared to any *in vivo* data obtained from patients.

As discussed above, the study on the active function of atherosclerotic artery suggests that the diseased artery has an adaptation response to change its muscle function to maintain the *in vivo* distensibility. Further investigation on the mechanisms underlying this observation can be performed, such as quantification of endothelin receptors in both healthy and diseased arteries to correlate the results with the change of contractile response. In addition, other pharmacological drugs can be used to investigate whether the finding of using ET-1 is a general phenomenon of altering contractility of atherosclerotic tissue.

The finding in Chapter 6 suggests that the immediate digestion of hyaluronan in rat aortas does not significantly change the arterial stiffness. Therefore, a further study on the long-term effects of hyaluronan accumulation or deficiency in artery should be carried out with transgenic or drug-treated animal models. This long-term change of arterial hyaluronan content can then be associated with the changes of aortic stiffness and the nature of arterial ECM proteins such as collagen constriction and elastin fragmentation.

The designed inflation test system in Chapter 7 requires further improvements for future studies on the local mechanical properties of artery. A non-frictional expandable device is required to replace the current balloon to obtain more accurate regional deformation. The device is also needed to have different sizes in order to be used for both human and animal arteries as well as for diseased artery with seriously occluded lumen. Having these improvements, the FE modelling and error minimisation approach in Chapter 4 can then be used to determine the regional stiffness of the artery. In addition to obtaining the mechanical properties of atherosclerotic artery with physiological loading, this approach can be used to study the associations of ageing-induced arterial stiffening with regional structural changes such as calcium deposition and elastin fragmentation.

In conclusion, the methodologies and finding in this thesis can be used in future research studies with improvements in techniques and protocols, thus providing more in-depth knowledge on the biomechanics of both healthy and diseased arteries.

.

9. Appendix

Appendix I: MATLAB Function for the Calculation of Stretches

```
function [lambdaX1, lambdaX2, lambdax, lambday, lambda1, lambda2,
thetaxy, theta12, phi]=stretchcalc(X1,X2,x1,x2);
% written by Michael Sutcliffe mpfs 12/8/08
% theory taken from Abaqus theory manual 6.8.1, section 1.4.1
% see also
http://www.engin.umich.edu/class/bme506/bme5062000/bme506formlec/larg
edeflec/largedef.htm
% test for rotation
% initial position X and X+dX
% deformed position x and x+dx
% x1 in x dirn
% x2 in y dirn
% assume grids are square and aligned in x1 and x2 directions
% take deformation across grid as mean of deformations at corners
% F is deformation gradient matrix
% dx= partial (dx/dX).dX
% F = partial (dx/dX)
% R is rotation matrix
% V is stretch matrix
% F = V.R
% lambda is stretch lambda=dl/dL where dl are lengths between
elements
% lambdax along orientation nearest to X1
% lambday along X2 direction
% lambdaX1 stretch along 1 direction
% lambdaX2 stretch along 2 direction

% lambda1 minimum lambda
% lambda2 max lambda
% theta12 is orientation of largest stretch direction
% thetaxy is orientation of lambdax relative to X1 direction
% phi is rigid body rotation

% X1=[0 1 ; 0 1]
% X2=[0 0; 1 1]
% x1=[0 1; -.1 0.9]
% x2=[0 0.1; 1 1.1]
% lambdacheck=1/sqrt(2)*sqrt(0.9^2+1.1^2)
% test for stretch in x1 and x2 directions

% X1=[0 1 ; 0 1]%initial
% X2=[0 0; 1 1]
% x1=[0 1.1; 0 1.1]%final
% x2=[0 0; 1.5 1.5]

dX1=X1(1,2)-X1(1,1);
dX2=X2(2,1)-X2(1,1);

dx1dX1=mean(x1(:,2)-x1(:,1))/dX1;
dx1dX2=mean(x1(2,:)-x1(1,:))/dX2;
dx2dX1=mean(x2(:,2)-x2(:,1))/dX1;
dx2dX2=mean(x2(2,:)-x2(1,:))/dX2;
F=[dx1dX1 dx1dX2 ;dx2dX1 dx2dX2;];
```

```
lambdaX1=dx1dX1;
lambdaX2=dx2dX2;
% dx=[dx1 dx2]
% dX=[dX1 dX2]
% dxcheck=F*dX'
Ft=F';
FF=F*Ft;
[vector lambda]=eig(FF);
lambda1=sqrt(lambda(1,1));
lambda2=sqrt(lambda(2,2));

n1=vector(:,1);
n2=vector(:,2);
V=lambda1*n1*n1'+lambda2*n2*n2';
Vinv=1/lambda1*n1*n1'+1/lambda2*n2*n2';
R=Vinv*F;
Fcheck=V*R;
phi1=R(:,1);

if (n1(1)~=0)
    theta1=atan(n1(2)./n1(1));
else
    theta1=pi/2;
end
if (n2(1)~=0)
    theta2=atan(n2(2)./n2(1));
else
    theta2=pi/2;
end
theta12=theta2;

% eigenvalues are sorted in ascending order, with theta2 angle to
maximum stretch
% choose lambdax in x direction by swapping where angle exceeds 45
degrees
if theta2 > pi/4 | theta2 < -pi/4  % max stretch is in y direction
    thetaxy=theta1;
    lambdax=lambda1;
    lambday=lambda2;
else  % max stretch is in x direction
    thetaxy=theta2;
    lambdax=lambda2;
    lambday=lambda1;
end
if (phi1(1)~=0)
    phi=atan(phi1(2)./phi1(1));
else
    phi=pi/2;
end
```

Appendix II: MATLAB Function for the Calculation of Strains

```
function [strain11,strain22,strain12]=straincalc(X1,X2,x1,x2)
% Function to calculate green strains of an element
% Written by Chen Yen Ooi 27/04/2012, modified from stretchcalc
function of mpfs
% Theory taken from Abaqus Theory Manual 6.9.1, Section 1.4.1 and the
website
http://www.engin.umich.edu/class/bme506/bme5062000/bme506formlec/larg
edeflec/largedef.htm
% Initial position X and X+dX
% Deformed position x and x+dx
% x1 in x direction
% x2 in y direction
% Assume grids are square and aligned in x1 and x2 directions
% Take deformation across grid as mean of deformations at corners
% F is deformation gradient matrix
% dx = partial (dx/dX).dX
% F = partial (dx/dX)

dX1=X1(1,2)-X1(1,1);
dX2=X2(2,1)-X2(1,1);

dx1dX1=mean(x1(:,2)-x1(:,1))/dX1;
dx1dX2=mean(x1(2,:)-x1(1,:))/dX2;
dx2dX1=mean(x2(:,2)-x2(:,1))/dX1;
dx2dX2=mean(x2(2,:)-x2(1,:))/dX2;
F=[dx1dX1 dx1dX2; dx2dX1 dx2dX2];

% right Cauchy deformation tensor
C=F'*F;

% calculate Green-Lagrange strains
E=(C-[1 0; 0 1])/2;

strain11=E(1,1);
strain22=E(2,2);
strain12=E(1,2);
```

Appendix III: Abaqus User Subroutine for Controlling Thermal Expansion

```
c Abaqus user subroutine to define incremental thermal strains with
an erf function, see descriptions in Abaqus User Subroutines
Reference Manual, Section 1.1.29, Abaqus 6.11 Documentation
Collection

c Written by Chen Yen Ooi on 15/07/2013

c Referred mainly to the uexpan1x.f example in the Abaqus
Verification Manual, Section 4.1.16, Abaqus 6.11 Documentation
Collection

c param1, param2, and param3 are changed iteratively to provide an
optimum match of the finite element and experiment results

c user subroutine uexpan

      subroutine uexpan(expan,dexpandt,temp,time,dtime,predef,dpred,
     $     statev,cmname,nstatv,noel)
c
      include 'aba_param.inc'
c
      character*80 cmname
c
      dimension expan(*),dexpandt(*),temp(2),time(2),predef(*),
     $     dpred(*),statev(nstatv)
c
      param1 = -0.085
      param2 = 25000000
      param3 = 0.4
c
      func1 = erf(param2*temp(1))
      func2 = erf(param2*(temp(1)-temp(2)))
      expan(1) = param1*(func1**param3-func2**param3)
c
      return
      end
```